REDUCIBLE OXIDE BASED OXYGEN CARRIERS FOR CHEMICAL LOOPING COMBUSTION AND PARTIAL OXIDATION OF METHANE

by

Saurabh Kiran Bhavsar

Bachelor in Chemical Engineering,

Institute of Chemical Technology (formerly UDCT), Mumbai, India, 2009

Submitted to the Graduate Faculty of

Swanson School of Engineering in partial fulfillment

of the requirements for the degree of

Doctor of Philosophy

University of Pittsburgh

2014

UNIVERSITY OF PITTSBURGH

SWANSON SCHOOL OF ENGINEERING

This dissertation was presented

by

Saurabh Kiran Bhavsar

It was defended on

March 26, 2014

and approved by

Robert Enick, PhD, Professor, Department of Chemical and Petroleum Engineering

Sachin Velankar, PhD, Professor, Department of Chemical and Petroleum Engineering

Rongchao Jin, PhD, Professor, Department of Chemistry, Carnegie Mellon University

Dissertation Director: Götz Veser, PhD, Professor, Department of Chemical and Petroleum Engineering

REDUCIBLE OXIDE BASED OXYGEN CARRIERS FOR CHEMICAL LOOPING COMBUSTION AND PARTIAL OXIDATION OF METHANE

Saurabh Kiran Bhavsar, PhD

University of Pittsburgh, 2014

Chemical looping combustion (CLC) is a novel combustion technology that offers a highly efficient route towards clean combustion of fuel with inherent CO_2 capture. In CLC, a fuel is combusted in reducer reactor in contact with an oxygen carrier (typically a metal oxide) and subsequently re-oxidized by air in oxidizer. Condensation of steam from reducer effluent results in high purity sequestration ready CO_2 streams. Thus CLC results in a NO_x-lean, flame-less oxyfuel combustion process eliminating the need for air separation. Splitting the combustion into two half processes provides a high degree of flexibility in CLC for process intensification, e.g. a wide range of oxygen carriers, fuels and oxidant gases can be used, albeit use of various fuels/oxidants have their own challenges.

Typically in CLC, a metal is supported on a high temperature stable matrix to provide the required thermal stability in harsh redox conditions. However these non-reducible supports do not contribute any oxygen in the combustion process or facilitate the reduction of supported metal. Therefore in the present work, we test the applicability of reducible oxides like ceria as supports in CLC. It was found that, compared to non-reducible supports, the redox properties of ceria strongly facilitate efficient utilization of metal oxides in the process, thus resulting in improved redox kinetics and higher carrier conversion. The broad applicability of the concept was tested with various transition metals typically used in CLC. Furthermore, the reactivity of

carriers was enhanced by employing systematically engineered mixed-oxides of iron, nickel and/or manganese.

Beyond combustion, tailoring the metal phase and reactor operation was used for partial oxidation of methane to produce syngas – a valuable feedstock in chemical industry. Utilization of the looping concept for partial oxidation results in a safe oxidation process eliminating the need for expensive air separation or noble metal catalysts. Steam, CO_2 or mixtures of both can be used as oxidants for ultra-pure H_2 or syngas generation and CO_2 activation. Current work underscores the fact that reactor operation in chemical looping allows targeting clean combustion, partial oxidation or various reforming processes, but rational design of oxygen carriers makes these processes viable.

TABLE OF CONTENTS

LIST OF TABLES

LIST OF FIGURES

NOMENCLATURE

C_P = heat capacity (J/kg.K)

ΔH_R = heat of reaction (J/ mol)

M_{act} = molecular weight of reactive component in solid carrier (kg/mol)

M_{H_2O} = molecular weight of steam (kg/mol)

T_0 = initial temperature (K)

$T_{\max}$ = maximum temperature (K)

$\Delta T_{\max}$ = maximum temperature rise (K)

v_g = gas velocity (m/s)

v_h = heat front velocity (m/s)

v_r = reaction front velocity (m/s)

w_{act} = weight fraction of reactive component in solid carrier

w_{g,H_2O}^{in} = weight fraction of steam in the feed

ρ = density (kg/m^3)

ε_s = porosity

ξ = stoichiometric factor (ratio of moles of gas to moles of solid in the oxidation reaction)

ACKNOWLEDGEMENTS

First and foremost, I would like to thank my adviser Dr. Götz Veser for his invaluable advice, countless number of discussions, constant support and encouragement. Expressing my gratitude in words is as good as trivializing your relentless efforts in transforming me from a timid student into a confident and knowledgeable researcher. The solid foundation you have laid will definitely help me in my future endeavors. I really admire your way of leading the research group, and especially our group seminars which focus on honing students' inquisitiveness and communication skills. I have been fortunate to learn and grow in your research group. I am also grateful to my committee members Dr. Enick, Dr. Velankar and Dr. Jin for providing me with many helpful insights on my work.

I would like to thank my senior lab-members Anmin Cao, Rahul Solunke, Lu Whaley, Shuang Liang, Sen Liu, Karen Uffalussy and Michelle Najera for their guidance and training. Chris Ewing, Yungchieh Lai, Amey More and Sharlee Mahoney thanks for your help and cooperation in the lab. It was fun moving lab-space with you guys. I really appreciate Charles Spyres, Ken Nadeau, Louis Miller, Brian Tackett and Natalie Isenberg for their willingness to learn and help in the experimental work. I am grateful for DOE-NETL's financial support.

In addition, I would like to extend my thanks to the staff of Chemical Engineering and Material Science departments at Pitt, especially Patricia Park, Rita Leccia, Bob Maniet, Al Stewart, Cole Van Ormer and Sushen Tang for their support.

I want to thank Prashanth, Balaji, Amey, Prasad, Anant and Mugdha for their altruistic friendship; our outings, photo-walks, table tennis and carrom sessions helped me enjoy my time outside laboratory. Shailesh *dada*, I am most fortunate to have an elder brother like you who guided me through my toughest times during PhD! Thanks for always being there for me and listening to my problems.

Last but not the least; I cannot adequately express my gratitude to my family. My parents, who sacrificed their dreams and always supported me, are the two most important people in my life. I salute my parents for giving me the belief and strength to achieve this dream. This would not have been possible without you!

1.0 INTRODUCTION

Sustainable supply of clean energy is a key challenge of our time. Anthropogenic CO_2 emissions have by now been unambiguously identified as main drivers for climate change, and emissions from energy production are the main contributions to those emissions[1]. While a transition away from fossil energy sources is the most promising solution to this problem, our dependence on those resources for roughly 80% of world-wide energy supply makes this a formidable task that will require unprecedented investment of effort and money and hence significant time. It is hence of paramount importance to develop near and mid-term reactor and process engineering solutions that allow us to address this challenge by combining fossil fuel based energy production with cost and energy-efficient carbon capture. At the same time, any such solution should ideally be flexible enough to accommodate a future switch to renewable sources, such as biomass and waste streams.

CO_2 can be captured by a wide range of technologies, which can be broadly classified in three categories: (i) *Pre-combustion*: Wherein fuel is de-carbonized by reforming it into syngas (H_2 and CO) and then converting it into H_2 and CO_2 via water gas shift reaction (WGS). CO_2 can be separated by physical or chemical absorption. (ii) *Oxy-combustion*: Instead of using air, pure oxygen obtained from cryogenic separation of air is used, resulting in N_2-free combustion with a high concentration of CO_2 in flue gas stream. (iii) *Post-combustion*: In which CO_2 is separated from flue gases using various capture techniques.

There are currently a wide range of technologies available for CO_2 capture, although the majority of them were not specifically developed for CO_2 sequestration. These processes have been practiced for a long time in chemical and petrochemical industries[2]. Existing technologies are based on physical or chemical separation of CO_2, which includes absorption, adsorption, cryogenics and membranes. Absorption techniques use a suitable solvent to absorb CO_2 from flue gas stream. Alkanolamines e.g. monoethanolamine (MEA) and diethanolamine (DMEA) are used in chemical absorption while methanol, dimethylether, polyethylene glocol and sulfolanes are used in physical absorption[2]. Issues like energy intensive solvent regeneration and equipment corrosion in presence of O_2 exist as challenges in absorption technique. Additionally, flue gas contaminants like SO_x and NO_x can have negative impact on the process performance.

Adsorption techniques utilizing solid sorbents e.g. zeolites, alumina and activated carbon also suffer from energy intensive regeneration. Porous membranes, which work on principle of size exclusion, have a major drawback of low throughput, requiring multistage operation or stream recycling. Future techniques for CO_2 separation, like advanced physical[3] and chemical[4] solvents, ammonia[5], PBI membranes[6], ionic liquids[7], metal-organic framework[8] and enzymatic membranes[9], are in the primitive stages of development.

Retrofitting natural gas fired combined cycle (NGCC) with energy intensive near commercial CO_2 capture processes could result in 8-10% reduction in power plant efficiency[10-11]. This translates to increased cost of produced electricity. By considering these factors, the development of a bridging technology for clean fuel combustion in energy production with inherent CO_2 capture is essential. Such process engineering solutions should not only stand out as cost-effective and efficient alternatives, but also be able to process wide range of renewable fuels in the future.

1.1 CHEMICAL LOOPING COMBUSTION

Chemical looping has emerged over the past two decades as one of the most promising and cost efficient approaches to address the previously outlined issues. In chemical looping combustion (CLC), the combustion of a fuel is broken down into two, spatially separated half-steps: The oxidation of an “oxygen carrier” (typically a metal) with air and the subsequent reduction of this carrier via reaction with a combustible fuel (see Figure 1). The oxygen carrier serves to selectively transport oxygen from the air reactor to the fuel reactor, while at the same time helping to thermally couple the two reaction half steps. It is important to note that the overall net reaction yields unchanged conventional fuel combustion, as shown below where ‘Me’ denotes a generic metallic oxygen carrier material and methane is used as a typical fuel:

Carrier oxidation (Oxidizer): $4\ Me + 2\ O_2 = 4\ MeO$ …(R1)

Fuel combustion (Reducer): $CH_4 + 4\ MeO = CO_2 + 2\ H_2O + 4\ Me$ …(R2)

Net reaction: $CH_4 + 2\ O_2 = CO_2 + 2\ H_2O$ …(R3)

The two reaction steps are typically conducted in two separate reactors which are coupled via the carrier transport between the reactors, most commonly in a circulating fluidized bed (CFB) configuration. However, due to the issues associated with the transport of large amounts of solids (in particular the attrition of the carrier material), fixed-bed reactors (FBR) with periodic switching of the reactor feed from oxidizing (air) to reducing conditions (fuel) - i.e. a temporal rather than a spatial separation of the two reactions steps - are also being actively investigated. While this configuration minimizes the issues associated with the mechanical strength of the carrier, control of temperatures in the reactor becomes a challenge in the fixed-bed process.

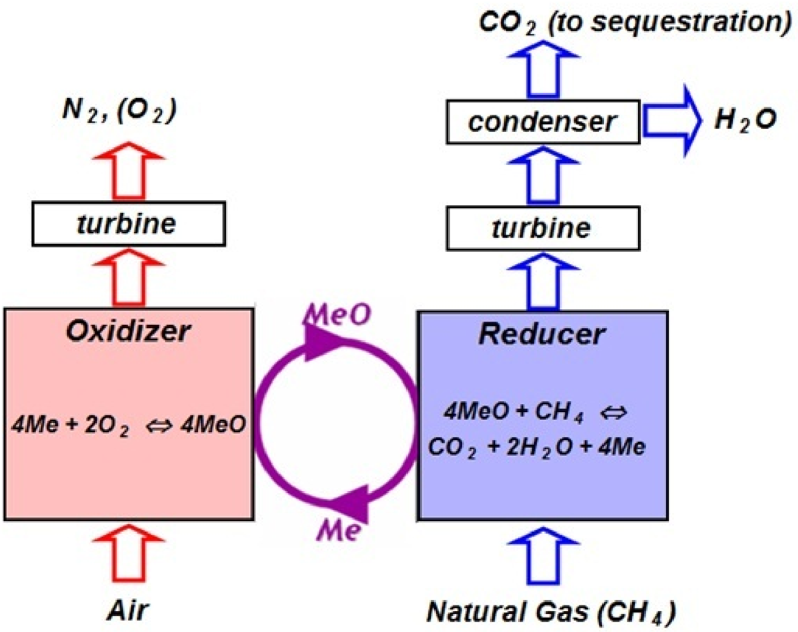

Figure 1. Schematic for Chemical Looping Combustion (CLC) using CH_4 as fuel. The oxygen carrier ("Me") is oxidized to form "MeO" in the "oxidizer"(air reactor) and transferred into the "reducer" (fuel reactor) where it supplies the oxygen for fuel combustion and is thus reduced back to "Me". Reduced metal is then transferred back to the oxidizer to close the material "loop".

The key advantage of CLC over conventional (mixed) combustion—beyond a flame-less combustion, and the suppression of NO_x—is the fact that CLC ideally produces a pure mixture of CO_2 and H_2O as combustion effluent, from which highly concentrated high-pressure (i.e. sequestration-ready) CO_2-streams can be produced after removal of steam via simple condensation. By avoiding the mixing of fuel and air at any point in the process, CLC entirely avoids nitrogen dilution of the combustion effluent and hence any of the CO_2 separation steps that cause significant cost and energy penalties in other "clean combustion" technologies. CLC can thus be seen as an oxyfuel combustion process which avoids the fundamental issues of conventional oxyfuel combustion (such as excessive combustion temperatures and expensive pre-combustion air separation), or as an air-blown combustion process without the cost and energy penalty of post-combustion CO_2 capture.

Despite the recent surge in interest of applying the chemical looping principle to clean combustion[12-14], chemical looping is in fact one of the oldest, large-scale industrial processes: Around the turn of the century (19th to 20th century!), Howard Lane built a hydrogen production plant in Great Britain which was based on the "looping principle"[15]. In this plant, iron was oxidized with steam to produce pure hydrogen and the produced iron oxide was then reduced in contact with coal gas to close the loop. A German patent by Messerschmidt in 1911 describes the same technology[16]. However, the development of cheaper steam reforming technology made the process eventually obsolete.

It was half a century later that Gilliland and coworkers at Standard Oil rediscovered the looping principle and applied it for the production of synthesis gas[17] and the production of pure CO_2 using Cu as the preferred carrier material[18]. It is noteworthy that the inventors already pointed out the fuel flexibility of the process (claiming broadly the use of "oxidizable carbonaceous material" and mentioning specifically hydrocarbons, methane, and coke). However, the process was not further pursued at the time, presumably due to lack of market demand.

Finally, Richter and Knoche in the US[19] and Ishida and Yin in Japan[20] (who coined the term "chemical looping combustion" in this publication) revisited this technology in the 1980s in the context of combustion based on the improved exergetic efficiency of this unmixed combustion technology in comparison to conventional combustion. However, the technology did not catch on, likely due to the increased process complexity. It was only the proposition by the same Japanese group in the 1990 to utilize this technology for CO_2 capture that resulted in a dramatic surge of interest in this technology[21-22]. Today, a vast number of academic and industrial laboratories around the world have developed research programs for this technology.

1.1.1 Oxygen carrier development

Large scale applicability of CLC is contingent upon availability of suitable oxygen carriers. Facile supply and uptake of oxygen by these materials is critical for the viability of the process. Periodic switching of chemical and thermal environments in looping processes subjects the oxygen carriers to harsh redox conditions, therefore imposing stringent demands on developing robust oxygen carriers, e.g. excellent thermal and mechanical stability is paramount for long-term operation of looping processes. In fact, the solid inventory in each reactor and solid circulation rates are primarily governed by the oxygen carrier capacity of carrier particles. Therefore, one of the most important characteristics of an oxygen carrier is its reactivity in both reduction and oxidation half cycles. In addition, the ability to completely combust the fuel to form carbon dioxide and steam—determined by the choice of metal and thermodynamics—is another important factor in achieving maximum fuel combustion efficiency. Resistance against attrition and crushing becomes important with use of these particles in fluidized bed reactors. Finally, the oxygen carrier material (metal and support oxides) should be low-cost, environmentally benign and abundantly available.

In order to meet these criteria, significant fraction of research efforts in chemical looping community are focused on development and testing of i) synthetic/engineered oxygen carriers (where metals are supported on a high temperature stable oxides to improve their thermal and mechanical stability) and ii) naturally occurring ores as a low-cost alternative. While the principle of CLC has been demonstrated widely[23-28], significant challenges remain for the technical realization of the concept. In particular, insufficient carrier stability and poor redox kinetics due to low reactivity of the oxygen carrier constitute key issues. Many efforts have been made to develop suitable oxygen carriers which can satisfy the stringent requirements placed on carriers under the harsh environment of CLC. Most of the oxygen carriers reported in literature are engineered materials: Cu-, Ni-, Fe-, Mn-, and Co-based carriers have been tested with regard to their thermal stability and redox kinetics[29-32], with the (active) metals typically rendered thermally stable by supporting them on inert oxides like Al_2O_3, SiO_2, ZrO_2, and $MgAl_2O_4$[33-37].

Among the various metals investigated for CLC, Fe has emerged as an attractive option due to its abundance, low cost, and low toxicity. However, its weak redox characteristics, low fuel conversion, and poor oxygen transport capacity ($Fe_2O_3 \Leftrightarrow Fe_3O_4$) due to the inaccessibility of some of its oxidation states in practical CLC operation constitute significant draw-backs[29, 38-39]. Ni-based oxygen carriers, on the other hand, are among the most thoroughly analyzed carriers for CLC[24, 33, 40-42] due to their high reactivity and near complete fuel conversion when using methane as feed[29]. However thermodynamic limitations forbids 100% selectivity towards CO_2 and steam formation, hence traces of CO and H_2 are observed in the products[35]. Moreover, Ni-based carriers are hampered by high cost and the well-known toxicity of nickel. Cu-based carriers have demonstrated high oxygen release capacity[43] and are more effective in the combustion of methane. Unlike Ni, they are not thermodynamically restricted and can yield complete combustion to CO_2 and H_2O. 100% combustion efficiency has been obtained in the operation of copper as a carrier metal[44], but this metal is not suitable for CLC due to its low melting point, which results in agglomeration problems[29, 45]. Increasing calcination temperature and decreasing copper loading are found to be critical in alleviating agglomeration related issues[46]. Cobalt has high oxygen transport capacity but is limited by high cost, environmental concerns and poor redox performance[45, 47]. Finally, similar to Fe-based materials, Mn-based carriers show promise due to their low toxicity, low cost and relatively high oxygen carrying capacity. In spite of that, there are only few studies investigating use of Mn-based oxygen carriers due to their poor reactivity and tendency to react with support oxides to form stable spinels[33, 37, 45].

Besides using mono-metallic carriers, where each metal has its own limitations, reactivity of oxygen carriers can be tailored by combining metals with different properties with aim to get the best of both the worlds: e.g. Cu-Ni carriers, herein, nickel helps abate agglomeration issues of copper, while the copper assists the thermodynamically hindered nickel to fully convert methane to CO_2 and steam[48]. Although conventionally used non-reducible oxides as supports assist in thermally stabilizing the supported metals, these support oxides are not active in oxygen release or uptake, and are inert ballast in the reactor. On the other hand, use of reducible oxides which are "active" in oxygen transport, e.g. ceria and titania, provide an excellent avenue for improving the oxygen carrying capacity and redox kinetics[39, 42], but there are very few reports investigating both the above-mentioned aspects. As a result, major part of the present work deals with investigating the impact of reducible supports and mixed-metal oxides for chemical looping processes. We aim to systematically tailor the metal phase and support phase for improving carrier reactivity and oxygen mobility/transport. The results will be discussed in chapters 3.0, 4.0, 5.0 and 7.0.

1.1.2 CLC for power generation

The use of chemical looping for power generation exists as one of the primary motivation for the development of CLC technology. CLC replaces the combustor in the process of energy generation. Therefore, the integration of CLC with infrastructure for power production is critical for effectively converting chemical energy into work or electricity. The added complexity of the process vs the advantage of inherent CO_2 capture can have significant impact on the efficiency of power generation. Simulation studies have shown that CLC is a promising technology with relatively high energetic efficiency in power or heat generation with inherent CO_2 capture[49-51].

Exergy analysis has been used as a tool for identification of important parameters in integration of CLC in power plants[19-20, 22, 52]. Exergy is a measure of maximum theoretical work that can be extracted from combined system of i) a system/process and ii) the environment, as the system passes from a given state to a state of equilibrium with the environment. Exergy in contrast to energy is destroyed in all real processes. Destruction of exergy in a flame-less combustion—where fuel and oxidizing gas are not directly mixed—is limited compared to conventional combustion of fuel with direct mixing of fuel and air. A comparative exergy analysis of natural gas fired CLC (Ni as oxygen carrier) and conventional power plant by Anheden and Svedberg[52] revealed that CLC results in less exergy destruction than conventional process. Moreover, same analysis showed that CLC shows higher exergetic power efficiency compared to conventional combustion (42.7% vs 37.9%). Thus the CLC process proves superior to conventional combustion even without considerations of CO_2 capture – a major advantage of CLC which can make the process more effective.

Since CLC is essentially envisioned to retrofit the current power production infrastructure e.g. natural gas combined cycles (NGCC), Naqvi and Bolland[53-54] studied the idea of using CLC coupled with combined cycles. The chemical looping combustion combined cycles (CLC-CC) concept essentially modifies the NGCC process, where off-gases from oxidizer (air) and reducer (CO_2) are used to run air and CO_2 turbines respectively. At oxidizer temperature of 1200^oC with

100% CO_2 capture with compressed to 110 bar, net plant efficiency greater than 52% can be obtained. Although slightly less than reference case of NGCC (56% at combustor exit temperature of 1425^oC), more importantly CLC-CC configuration eliminates post-combustion CO_2 capture requirements. Temperature of air reactor—which is a function of flowrate of air and solid circulation rate—has significant impact on efficiency of combined cycles, as it defines the turbine inlet temperature[54-55]. Thus the energetic efficiency increases with increasing oxidizer temperature[53-56]. When temperature is constrained by limitation of oxygen carrier particles, such as the low melting point of copper, a multi-staged CLC approach can be employed to increase the efficiency at lower temperature, albeit at the cost of increased process complexity[53].

Efficiency of power generation of pressurized CLC using natural gas as fuel (including CO_2 capture) is predicted within the range of 52 – 53%[53, 55], which is about 3 – 5% more than NGCC with state-of-the-art technology for CO_2 capture[51, 53, 57]. Kvamsdal et al[57] compared various options of CO_2 capture techniques against the conventional natural gas based power plant, and a comparison was made based on net plant efficiency and emission of CO_2. Post-combustion, oxy-fuel and pre-combustion capture concept-based cycles were considered with a 400 MW combined cycle plant as a reference case. Novel technologies like H_2 membrane separation reformer (50%), advanced zero emission power plant (50%), solid oxide fuel cell combined with a gas turbine (67%) and CLC (51%) showed better performance with respect to both efficiency and in most cases also CO_2 capture (capture rates ~100%). Post-combustion capture (Amine, 48%) and pre-combustion capture with auto-thermal reforming (47%), which are based on more mature technologies, show a lower efficiency along with an average capture rate of 90%. For a more realistic comparison, factors like technology maturity and cost should be accounted in analysis. Nevertheless, the study shows potential of CLC to be one of the most competitive technologies for power production and CO_2 capture.

1.1.3 Brief insight into economic analysis

Whether or not CLC will be adopted by the energy generation industry will ultimately depend on the cost of electricity produced and CO_2 delivered for long term storage. A case study[58] comparing natural gas fired combined cycle (NGCC), semi-closed cycle with amine absorption (to capture 90% CO_2) (SC-CA) and CLC power plant has been summarized in Table 1. In the study, the CLC plant was sized to 400 MW to avoid discrepancies coming from different scales. It can be observed that CLC gives higher net power output compared to the NGCC case due to less exergy destruction as discussed in previous section. The reduction in power output for SC-CA relative to NGCC is due to energy lost in separating CO_2 from flue gas streams (which is inherent in case of CLC).

Table 1. NGCC, SC-CA, CLC plant comparison (400 MW capacity)[57]

Parameters	NGCC	SC-CA	CLC
Net Power Output (MW)	373	332	403
CO_2 emissions (g/kW$_{th}$)	356	35.6	0
Net capital cost (M€)	151	185	257
Cost of electricity (€/MW$_{th}$)	40	51	59

Although CLC has merits of in-situ CO_2 capture, process complexities results in higher capital and electricity cost than NGCC or SC-CA. However, cost of electricity is calculated with assumption of no restrictions on CO_2 emissions. If carbon tax is implemented in future, the NGCC plant must account for its CO_2 emissions, which will significantly increase the electricity cost. At these early stages of CLC development, with sub-pilot scale units in operation, there is a high degree of uncertainty in the estimation of investment cost. With future developments cost involved can be accurately determined and potentially be lowered.

1.2 CHEMICAL LOOPING RELATED PROCESSES

While the initial interest in chemical looping was almost exclusively focused on combustion, the reaction engineering principle behind chemical looping – i.e. the splitting of a reaction into two spatially separated reaction half-steps which are coupled through the periodic oxidation and reduction of an "oxygen carrier" – has recently been applied to further fuel conversion reactions beyond combustion[12, 59]. In particular partial oxidation processes, in which the oxidation of the fuel is controlled to yield synthesis gas rather than the deep oxidation products CO_2 and H_2O, and reforming reactions, where the air feed to the oxidizer reactor is replaced by either steam or CO_2 in order to produce high purity hydrogen or CO streams, respectively, are finding increasing interest. In all of these cases the inherent product separation due to the lack of mixing between the fuel and the oxidant constitute again the main advantage of the "looping configuration" over the respective conventional process.

1.2.1 Syngas Generation by Chemical Looping Partial Oxidation of Methane

CLC offers a unique and efficient route for clean, NO_x-lean, and flameless combustion of fuel with no significant efficiency penalty for CO_2 capture, making it rather unique among current emerging technologies[52, 54-55, 57]. Concurrently, advances in drilling technology have made the tight formations like shale more accessible. As a consequence, domestic natural gas reserves are expected to almost double the in near future[60]. This has revived the interest in using the abundant supply of locally available natural gas to produce vast arrays of chemicals and intermediates, but conversion of methane into syngas (a mixture of CO and H_2) is a pre-requisite for such conversion processes. Although industrial production of synthesis gas from methane is almost exclusively based on steam reforming of methane (SRM) ($CH_4 + H_2O = CO + 3\ H_2$), SRM is an energy intensive process due to the endothermic nature of the reaction as well as the necessary down-stream processing required to achieve a H_2:CO ratio of 2 (desired in various syngas conversion processes).

In the last two decades, catalytic partial oxidation of methane (CPOM) has received much attention as a promising alternative technology. In CPOM, methane is converted with oxygen over a noble metal catalyst to syngas in a simple, one step reaction: $CH_4 + \frac{1}{2}\ O_2 = CO + 2\ H_2$ ($\Delta H_R = -37$ kJ/mol)[61]. The system is characterized by a high autothermal temperature exceeding 1000°C, which results in high reaction rates and short contact times[62]. CPOM has several advantages over SRM: Exothermicity of reaction allows for autothermal operation rendering external heating unnecessary. Moreover, high reaction rates allow for compact reactors and high throughput. In principle, CPOM is a good alternative for SRM, however issues like i) safety concerns of contacting fuel with oxidizing gas at high temperatures close to their upper flammability limit, ii) a need for an air separation unit to produce undiluted streams of syngas and iii) the use of expensive noble metal catalysts cast a shadow of concern over the applicability of CPOM on large-scale.

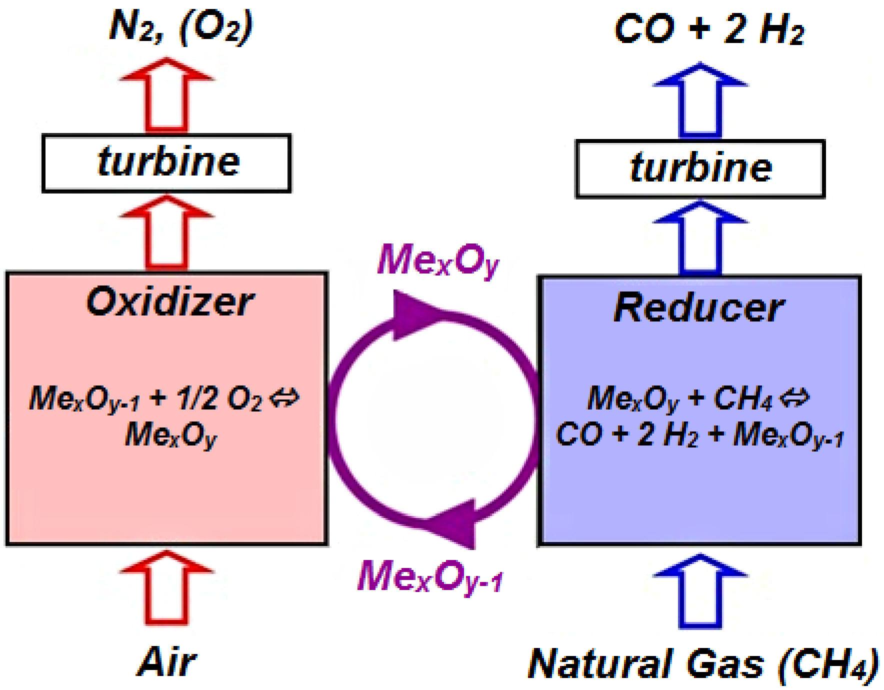

Figure 2. Schematic for chemical looping partial oxidation of methane (CLPOM). Limiting methane oxidation to syngas is achieved by controlling the amount of oxygen carrier in the fuel reactor or by controlling the oxidation states of the oxygen carrier in redox operation.

On the other hand, the application of chemical looping for partial oxidation of methane (CLPOM) can directly address some of the above-mentioned issues. In CLPOM, fuel oxidation to syngas can be achieved by controlling the relative amount of carbon and oxygen in the fuel reactor (see Figure 2) or by selection of appropriate carrier metal that can be operated in certain oxidation states selective for syngas generation as per following reactions with carrier Me_xO_y:

Oxidizer: $Me_xO_{y-1} + ½\ O_2 = Me_xO_y$ …(R4)

Reducer: $CH_4 + Me_xO_y = CO + 2\ H_2 + Me_xO_{y-1}$ …(R5)

Net reaction: $CH_4 + ½\ O_2 = CO + 2\ H_2$ …(R6)

In CLPOM, combustion of fuel is broken down into two spatially or temporally separated steps. As a result, unlike CPOM, fuel and oxidizing gases are never in direct contact, thereby eliminating flammability concerns in CLPOM. Furthermore, metal oxides act as oxygen carriers and result in N_2-free oxidation of fuel, therefore avoiding the need for expensive air separation to obtain pure oxygen and the net reaction still results in the partial oxidation of methane.

Thus, chemical looping can be used for partial oxidation of methane by controlling the fuel oxidation via use of an appropriate carrier material and/or adjustment of the carbon to oxygen ratio in the fuel reactor. Alternatively, steam can be co-fed with methane in the fuel reactor for concurrent steam reforming of methane to generate syngas using supplementary oxygen from metal oxides. For example, Ryden et al., used a continuously operated fluidized bed with a Ni-based carrier for syngas generation, both with and without steam co-feed. They report near complete methane conversion with H_2:CO ratio ~2, albeit at higher C/O ratios than the stoichiometric ratio for partial oxidation[63]. Furthermore, carbon formation was observed for sustained periods of operation. This issue was alleviated by feeding steam into the fuel reactor, which also resulted in a higher H_2:CO ratio. This indicates the onset of significant steam reforming and/or water gas shift activity.

The issue of carbon formation is a recurring theme with use of Ni-based carriers for chemical looping syngas generation. Although preventive measures like steam co-feeding abates/eliminates carbon deposition[64-65], a large amount of steam[66] ($H_2O:CH_4 = 1$, stoichiometrically sufficient to perform steam reforming) counters the objective of using chemical looping for partial oxidation. Moreover, depending on the $H_2O:CH_4$ ratio and propensity for SRM, steam feed could also significantly impact the energetics of the process and lower the overall exothermicity of the process. Pröll et al., investigated the effect of air to methane ratio on thermal balancing in the system to achieve autothermal operation (i.e. balance between exothermic and endothermic reactions occurring in two reactors)[67]. It was found that combustion dominates at near stoichiometric conditions and requires large amount of cooling when compared to partial oxidation which occurs at oxygen lean conditions and thus strongly reduces the cooling requirements. Although high reactivity of nickel has been the impetus behind its extensive use as a carrier material for partial oxidation, it suffers from coke formation. On the other hand Fe-based materials are selective but lack sufficient reactivity[66]. Apart from C/O ratio, activity for partial oxidation can be increased by using alternate carrier materials. Some reports on Fe-Ce mixed oxide carriers and $LaFeO_3$ perovskites are promising, although such carriers show low reactivity[68-71].

Therefore, in the present project, we aim to maximize selectivity and reactivity for syngas generation by optimizing both the factors: i) selection of appropriate oxygen carrier and ii) operation of redox process to tune C/O ratio in the fuel reactor. Detailed results and approach will be discussed in chapter 5.0.

1.2.2 Chemical looping reforming

Typically in CLC, hot oxidizer effluent gases (vitiated air) are considered to be useful for power generation. However, using air for the regeneration of a reduced carrier does not result in any useful off-gases from oxidizer but forms vitiated air. In principle, instead of air, CLC can work with wide range of oxidizing gases as long as the oxygen carrier shows sufficient reactivity towards it. This presents an opportunity to further intensify chemical looping processes by employing different oxidizing gas: By using steam, CO_2 or mix of both the process can result in formation of ultra-pure H_2, syngas generation or CO_2 activation.

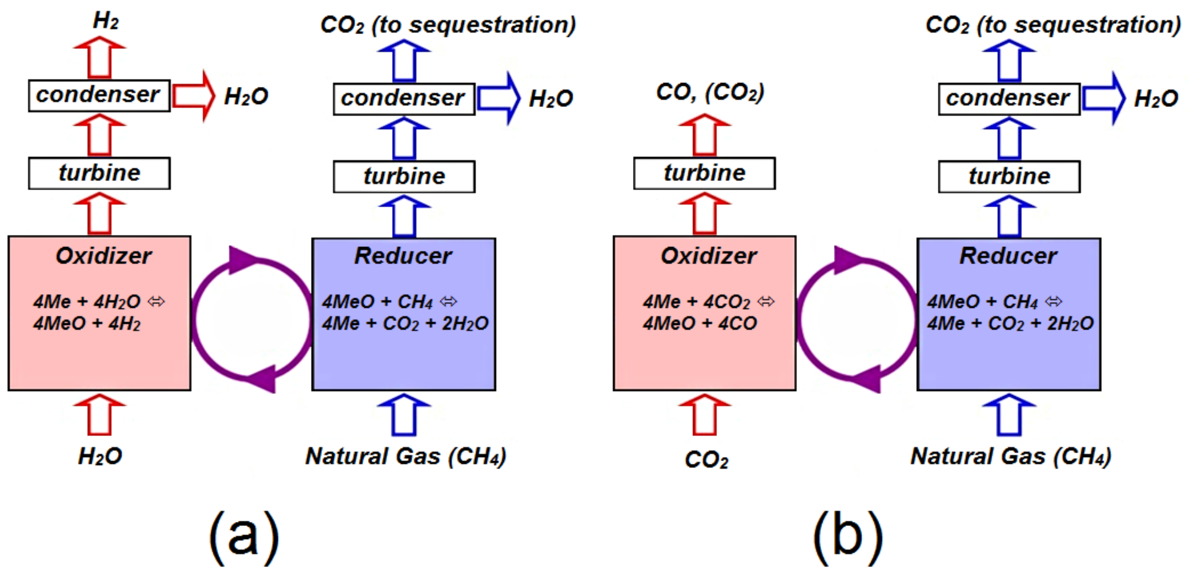

Figure 3. a**)** Schematic for Chemical Looping Steam Reforming (CLSR) process in which air is replaced with steam as oxidant, resulting in the production of pure H_2 stream in oxidizer effluent; b**)** Schematic for Chemical Looping Dry Reforming (CLDR) process in which air is replaced with CO_2 as oxidant resulting in CO_2 activation via production of CO in oxidizer exhaust.

1.2.2.1 Chemical looping steam reforming (CLSR):

The replacement of air with steam as an oxidant is of particular interest since in this case, ultra-pure H_2 is produced as an effluent of the oxidizer reactor after condensation of steam (Figure 3a)[72-75]. The process has a long history, dating back to 20th century, i.e. preceding the recent development in chemical looping by many decades, and is historically often referred to as "steam-iron process"[15-16]. Utilizing steam as an oxidant results in "Chemical Looping Steam Reforming" (CLSR) of the fuel used (in this case methane) as net reaction:

Oxidizer: $4\ MeO + 4\ H_2O = 4\ MeO + 4\ H_2$ …(R7)

Reducer: $CH_4 + 4\ MeO = CO_2 + 2\ H_2O + 4\ MeO$ …(R8)

Net reaction: $CH_4 + 2\ H_2O = CO_2 + 4\ H_2$ …(R9) where, Me represents the reduced oxygen carrier metal and MeO is the corresponding metal oxide. CLSR is a particularly attractive technology as it does not require separation of H_2 from CO, in contrast to conventional SRM which produces hydrogen in the form of syngas, requiring down-stream clean-up. CLSR thus has the potential to be a relatively efficient technology for the production of high purity H_2 streams with inherent separation and capture of CO_2 emissions.

Various metals have been scanned thermodynamically and iron emerged as the most promising candidate with a redox cycle limited to $Fe_3O_4 \Leftrightarrow Fe/FeO$[75]. Iron-based carriers have been used to demonstrate the feasibility of the process in batch[76] and continuous[77] fluidized bed reactors. Our research group has proposed CLSR in a fixed-bed reactor instead of a fluidized bed configuration in order to optimize energetic efficiency via heat integration between the two half steps of the reaction (which are now conducted in a temporal rather than spatial separation mode, i.e. the reactor is operated via periodic switching of the reactor feed between fuel and steam)[75]. Chiesa et al. proposed the idea of employing a second oxidizer using air to completely oxidize the carrier to Fe_2O_3 for efficient energy recovery from gaseous streams exiting the reactors. The study discussed various plant configurations for CLSR and predicted efficiencies similar to conventional SRM with reduced environmental impact[78].

1.2.2.2 Chemical looping dry reforming (CLDR):

While CLC is highly efficient for CO_2 capture, it does not offer a solution for CO_2 sequestration. Concerns about the lack of a secure and proven sequestration technology have motivated widespread efforts to utilize CO_2 via activation and re-introduction into chemical processes through a wide variety of approaches[79-81]. This makes a conceptually simple CO_2 activation step, the reduction to CO, an attractive route, since CO is a highly versatile and widely used chemical and can feed into a wide range of processes with a large cumulative capacity[79, 82-83].

This is done by using CO_2 as an oxidant instead of the air used in conventional CLC or in place of steam in the CSLR process, resulting in a process called “Chemical Looping Dry Reforming” (CLDR) (see Figure 3b). When using methane as the fuel, CLDR produces a net reaction similar to the dry reforming of methane, as shown below based on a metallic 'Me' oxygen carrier:

Oxidizer: $4\ Me + 4\ CO_2 = 4\ MeO + 4\ CO$ …(R10)

Reducer: $4\ MeO + CH_4 = 4\ Me + CO_2 + 2\ H_2O$ …(R11)

Net reaction: $CH_4 + 3\ CO_2 = 4\ CO + 2\ H_2O$ …(R12)

However, this process differs from conventional catalytic dry reforming processes: While the target of conventional dry reforming ($CH_4 + CO_2 = 2\ CO + 2\ H_2$) is high syngas yield, CLDR ideally targets to maximize the CO yield with no selectivity for H_2. CLDR is thus a process optimized for CO_2 activation and utilizes the full chemical potential of the fuel towards this target.

Our laboratory has in recent years pioneered this process and demonstrated its feasibility[84]. Fe-based carriers emerged again from a thermodynamic screening study as the most attractive candidates for this process due to a combination of low cost, low toxicity, thermodynamically favorable equilibrium for the reaction with CO_2. However, since CO_2 is both a highly stable molecule and a weak oxidant, activity of the carrier is a critical aspect for this process, motivating the development of nanostructured oxygen carriers with the aim to minimize kinetic limitations. Utilizing nanostructured core-shell Fe@SiO_2 and nanocomposite Fe-BHA (Barium Hexa-aluminate) were used to show that efficient CO_2 activation is indeed possible via a CLDR process[84-85] the details of which will be discussed in chapter 6.0.

1.2.2.3 Chemical looping mixed reforming (CLMR):

Based on the above discussion of CLSR and CLDR processes, it appears to be the logical next step to combine these looping process by feeding a combination of steam and CO_2 as oxidizing agents to the oxidizer, thus directly producing syngas[59]. This process is analogous to thermochemical splitting of water and CO_2[86-87]. However, instead of using concentrated solar energy for the thermal decomposition of the oxygen carrier, a fossil or renewable fuel is used for the chemical reduction.

As Fe has been shown to be suitable for both CLSR and CLDR, it is a natural candidate of choice for chemical looping mixed reforming (CLMR) process. The relevant reactions are shown below for CH_4 as fuel and the oxygen carrier transitioning between Fe and Fe_3O_4, indicating a flexible CO_2:H_2O ratio in the oxidizer feed. It can be seen that this process would potentially result in a highly flexible scheme for syngas production with adjustable CO:H_2 ratio:

Oxidizer: $3\ Fe + (2-x)\ CO_2 + x\ H_2O \Leftrightarrow Fe_3O_4 + (2-x)\ CO + x\ H_2$ …(R13)

Reducer: $CH_4 + Fe_3O_4 \Leftrightarrow CO_2 + 2\ H_2O + 3\ Fe$ …(R14)

Net reaction: $CH_4 + (1-x)\ CO_2 + (x-2)\ H_2O \Leftrightarrow (2-x)\ CO + x\ H_2$ …(R15)

Since steam and CO_2 have different reactivities, here we would be focusing on investigating the thermodynamic feasibility of syngas production with flexible CO:H_2 ratio. CLMR and its fuel-free solar process are very attractive, as they essentially run combustion in reverse, i.e. they use solar/chemical energy to reduce CO_2 and H_2O mixtures to synthesis gas (which could then be used again directly as a fuel, or further converted to methane, methanol, or synthetic fuels for easier transport and storage).

2.0 REDUCIBLE SUPPORTS FOR NICKEL-BASED OXYGEN CARRIERS

Although the concept of CLC has been demonstrated[88-92], there is still room for improvement in design of efficient oxygen carriers where insufficient carrier stability and poor redox kinetics are still key issues. Typically, metals like Cu, Ni, Fe, Mn, and Co[29-32] are rendered thermally stable by supporting them on high temperature supports such as Al_2O_3, SiO_2 or similar oxides[35-37]. While these conventional supports serve their purpose of endowing the carriers with thermal stability, they pose an energy penalty on the process (due to the transport of this additional mass between the two reactors as well as the temperature cycling of the inert phase) and do not contribute towards the oxygen carrying capacity of the carrier or facilitate redox reactions.

However, the use of "active" supports is well established in heterogeneous catalysis, where reducible oxides—such as CeO_2—are in widespread use as a support for metal nanoparticles in oxidation and redox catalysis[93], such as automotive exhaust abatement[94], water gas shift[95-96], and catalytic methane oxidation[97-99]. In all these examples, the promoting effect of CeO_2 on the active metal phase of the catalyst is due to its oxygen storage capacity, i.e. the facile and reversible release of lattice oxygen via reduction of Ce^{4+} to Ce^{3+}. Specifically Ni-CeO_2 catalysts have been studies in various oxidation reactions, taking advantage of an O-buffering effect[100] and a synergistic effect between NiO and CeO_2 is thought to be crucial for enhanced methane combustion[101].

Despite this widespread use in catalysis, however, ceria (or other reducible oxides) have found little attention as support matrix in oxygen carrier materials for CLC[12, 14, 102]. Yan and coworkers[103] recently studied syngas production via chemical looping reforming (CLR) of methane using Ce-Fe mixed oxides with different Ce/Fe ratios at 850^{o}C and found that chemical interactions between surface iron sites and the Ce-Fe solid solutions enhanced the reducibility of the carriers. Wang and coworkers[104] investigated similar composite oxygen carriers composed of cerium oxide doped with Fe, Cu and Mn oxides for producing syngas by CLR and found again that doping the ceria with transition metal oxides can enhance the oxygen release capacity of ceria. Ceria and ZrO_2 have furthermore been investigated as supports for bimetallic $CuFe_2O_4$ in two-step methane reforming consisting syngas generation in the fuel reactor and water splitting in the oxidizer reactor[105]. Although ZrO_2-based carriers showed higher methane conversion due to better thermal and phase stability of ZrO_2, CeO_2 was found to be a better support than ZrO_2 in terms of reactivity and selectivity. Finally, ceria has also been successfully used as an oxygen carrier in solar-driven thermochemical dissociation of CO_2 and H_2O, a closely related process to CLC in which concentrated solar power is used to thermally decompose the oxide rather than reduce it in contact with a fuel[87].

The above reasoning and the few, but encouraging, existing reports motivates this study in which we investigate the performance of nanostructured CeO_2 and La_2O_3 as oxygen carriers for CLC. Using Ni-based oxygen carriers supported on two reducible (CeO_2, La_2O_3) and two non-reducible (Al_2O_3, SiO_2) supports we compare the impact of these support materials on activity and stability in periodic redox operation with air and H_2 as model fuel. Nickel was chosen as a choice of metal because of its well-known high reactivity in CLC[12, 14, 29]. From these results, ceria and alumina based carriers were down-selected for further studies with CH_4 as fuel in thermogravimetric (TGA) and fixed-bed reactor studies. Overall, we find that the use of a reducible support can have a pronounced effect on carrier utilization and redox kinetics.

2.1 EXPERIMENTAL

2.1.1 Carrier synthesis and characterization

CeO_2 nanorods were prepared by a hydrothermal synthesis procedure previously adapted in our research group[96]. Briefly, 0.752 g of $Ce(NO_3)_3{\cdot}6H_2O$ (99+%, Sigma-Aldrich) were dissolved in 8 ml DI water. 30 ml of NaOH (98+%, Sigma-Aldrich) solution (7 M) was rapidly added under vigorous stirring. After 30 min of stirring, the slurry was transferred into a 50 ml autoclave, heated to 100^oC under autogenous pressure for 72 h, and then allowed to cool to room temperature. The product was washed by DI water and collected via centrifugation to remove any ionic remnants until the pH of the solution was 7. After drying at 100^oC overnight and calcination at 450^oC for 2 h, the final product was obtained. It should be noted that the CeO_2 nanorods are not high-temperature stable, and were used in the present study due to the ease and efficiency of the synthesis procedure (in comparison to microemulsion-based syntheses[106], for example), not due to the nanorod structure. Other high surface area supports were obtained commercially in powder form (La_2O_3, REacton® 99+%, Alfa Aesar; γ-Al_2O_3, 99+%, and SiO_2 nanopowder, 99+%, Sigma-Aldrich) and used as obtained.

Ni-based carriers with 40 wt.% Ni weight loadings were synthesized from these supports by simple incipient wetness technique. Briefly, 0.33g of $Ni(NO_3)_2.6H_2O$ (99+%, Sigma-Aldrich) was dissolved in 1 ml DI water to obtain a clear solution. 100 mg of support material was added and stirred for 2 h. The obtained slurry was dried in a vacuum oven at 80-100°C overnight, and calcined at 450°C for 2 h to get the final form of the oxygen carrier.

The materials were characterized at various stages (after synthesis, reactive tests in TGA and fixed-bed) via transmission electron microscopy (TEM, JOEL 200), X-ray diffraction (XRD, Phillips PW1830 with typical 2θ scans between 15° and 90°), nitrogen porosimetry (BET, Micromeritics ASAP 2020) and SEM equipped with EDAX (Phillips XL30).

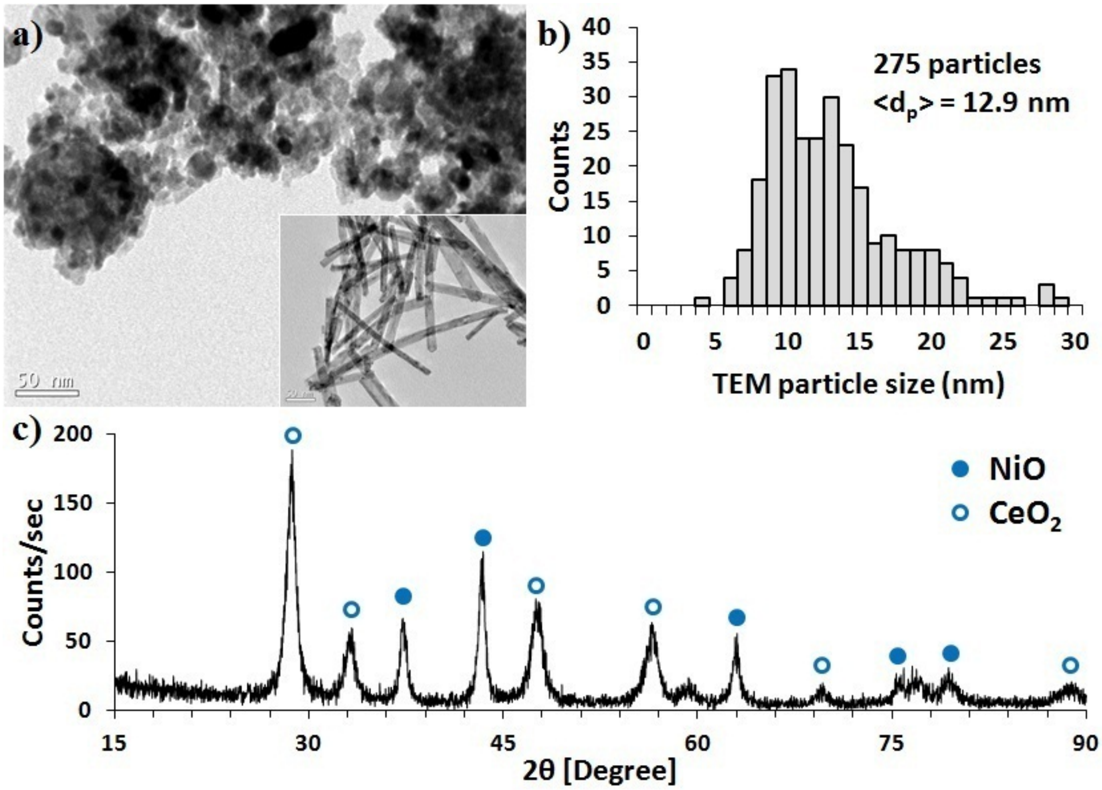

Figure 4. a) TEM micrograph of a typical Ni-CeO_2 carrier after calcination at 450°C in air for 2 h (the inset shows the initial CeO_2 nanorods; both scale bars = 50 nm); b) Ni particle size distribution of freshly calcined Ni-CeO_2; and c) XRD pattern of freshly synthesized NiO-CeO_2 (in oxidized state) after calcination in air.

Figure 4a shows a typical TEM image of freshly calcined Ni-CeO_2, where nickel is displayed as black and CeO_2 as gray matrix with inset of image showing CeO_2 nanorods after calcination. Typical BET surface area of the CeO_2 nanorods was ~98 m^2/g. Figure 4b shows the particle size distribution determined from TEM images, indicating a rather broad distribution of nickel particle sizes from 5-30 nm with an average particle size of ~13 nm. The XRD in Figure 4c confirms the presence of separate NiO and CeO_2 phases in freshly synthesized NiO-CeO_2, i.e. the absence of a mixed oxide phase. The surface area of the oxidized NiO-CeO_2 sample is ~56 m^2/g with 40.9 wt.% Ni loading (determined by compositional analysis with EDAX). All other carriers were similarly characterized and the respective information is summarized in Table 2. Note that the CeO_2 nanorods initially maintain their structure post-calcination at 450^oC, but this rod structure is not sustained after deposition of nickel.

Table 2. Detailed characterization of Ni-based carriers, synthesized by simple wet impregnation technique, after calcination in air at 450^oC and after reaction in TGA at 800^oC with H_2, Air. (*No La_2O_3 detected, **La_2O_3 present as La_2NiO_4 and $La(OH)_3$, ***SiO_2 used is amorphous)

Carrier	Ni wt.% (EDAX)	Calcined in air at 450^oC			Post CLC in TGA at 800^oC H_2/Air		
		Surface area (m^2/g)	Ni particle size (nm)	Support particle size (nm)	Surface area (m^2/g)	Ni particle size (nm)	Support particle size (nm)
Ni-CeO_2	40.9	55.8	12.7	9.6	16.7	23.6	20.3
Ni-La_2O_3	39.1	27.3	6.1	-*	7.13	21.4	-**
Ni-Al_2O_3	40.6	51.1	9.7	6.9	49.1	21.6	9.2
Ni-SiO_2	40.9	126.6	11.2	-***	54.9	20.7	-***

2.1.2 Reactive Tests

Kinetics and thermal stability of the carriers were initially evaluated in a thermogravimetric analyzer (Perkin Elmer TGA-7). In a typical run, between 5 – 20 mg of oxygen carrier were heated inside the TGA cradle in an inert gas stream (N_2, Grade 5.0) to the desired reaction temperature. Then H_2 (Grade 5.0; 20 sccm) and air (Grade 0.1; 20 sccm) were flown alternating to simulate the periodic reduction – oxidation cycles of CLC. Between reduction and oxidation phases, the TGA was purged with N_2 (Grade 5.0; 20 sccm) to avoid formation of potentially flammable gas mixtures inside the instrument. H_2 is used here as a model fuel to differentiate the carrier performance in cyclic redox operation and to elucidate the effect of reducible supports for Ni-based carriers without the added complexity of carbon formation and selectivity considerations when using methane as fuel.

Carriers were down-selected based on the results from TGA tests with H_2 and further evaluated with CH_4 at 800^oC using cycling times such that carbon formation—and hence possible carbon carryover and burn-off in the oxidation half-cycle—were avoided in order to enable efficient CO_2 capture. The suitable time for reduction (2.5 min at 5 sccm CH_4) was determined by varying the CH_4 reduction time and flowrate while monitoring any carbon burn-off in oxidation half cycle. All other experimental conditions were identical as above. All experiments were conducted at ambient pressure conditions.

Fixed bed experiments were conducted to investigate the effectiveness of carriers for CH_4 conversion to H_2O and CO_2 – crucial for efficient CO_2 capture in CLC. 100 mg of Ni-CeO_2 or Ni-Al_2O_3 was placed inside the quartz-glass tubular reactor (¼” ID) which was inserted into an electric oven (Thermo Electron Corporation – Lindberg/Blue M). The oven was heated to 800^oC and CH_4 (1 sccm, Grade 2.0, y_{CH4} = 16.7% in Ar) and air (20 sccm, Grade 0.1) were flown alternating to simulate the periodic reduction and oxidation in CLC. In between reduction and oxidation of the carrier the reactor was again purged with argon (Grade 5.0) to avoid formation of explosive mixtures of air and CH_4 inside the reactor. The effluent gases were recorded after condensation of moisture using a mass spectrometer (Pfeiffer Omnistar QMS 200), and translated into molar flowrates (n_i) for all species observed during the reaction. The carbon balance was performed to assure the accuracy of the analysis and closed within 5 – 10% error for all reported experiments.

Carbon Balance:

$$n_{CH_4,in} = n_{CH_4,out} + n_{CO_2,out} + n_{CO_{out}} + 0.5 \times (n_{H_2,out} - 2n_{CO_{out}}) \qquad \text{…Eq. (1)}$$

On-stream methane conversion (X_{CH4}) and cumulative carrier ($X_{carrier}$) conversion were evaluated using:

$$X_{CH_4} = \frac{n_{CH_4,in} - n_{CH_4,out}}{n_{CH_4,in}}, \qquad X_{Carrier} = \frac{4\sum n_{CO_2,out} + \sum n_{CO,out}}{Total\ mol\ of\ O\ in\ carrier} \qquad \text{…Eq. (2), (3)}$$

Selectivity of various species (S_i) viz. CO_2, H_2, CO and carbon (C) formation by methane pyrolysis was calculated by the following equations.

$$S_{CO_2} = \frac{n_{CO_2,out}}{(n_{CH_4,in} - n_{CH_4,out})}, \qquad S_{CO} = \frac{n_{CO_{out}}}{(n_{CH_4,in} - n_{CH_4,out})} \qquad \text{…Eq. (4), (5)}$$

$$S_{H_2} = \frac{0.5 n_{H_2,out}}{(n_{CH_4,in} - n_{CH_4,out})}, \qquad S_{Carbon} = \frac{0.5(n_{H_2,out} - 2n_{CO_{out}})}{(n_{CH_4,in} - n_{CH_4,out})} \qquad \text{…Eq. (6), (7)}$$

As expected, we find that complete combustion, partial oxidation and catalytic pyrolysis of methane are the dominant reactions occurring in the system shown using generic metal oxide “MeO” and reduced metal “Me":

Complete Combustion: $CH_4 + 4\ MeO = CO_2 + 2\ H_2O + 4\ Me$ …(R16)

Partial Oxidation: $CH_4 + MeO = 2\ H_2 + CO + Me$ …(R17)

Methane Pyrolysis: $CH_4\ (+\ Me) = C + 2\ H_2\ (+\ Me)$ …(R18)

2.2 RESULTS AND DISCUSSION

2.2.1 CeO_2 and La_2O_3 Reducibility

Since ceria and lanthana are known to be able to act as oxygen storage and oxygen transfer materials, these pure oxides show potential to be used as oxygen carrying for CLC. Thus, to assess the viability of these oxides in CLC, pure CeO_2 nanorods and La_2O_3 were used in TGA at above mentioned conditions. The degree of oxygen loss during the reduction (30 min) is quantified for CeO_2 by the degree of reduction (δ), defined by the reaction:

$CeO_2 + \delta\ H_2 = CeO_{2-\delta} + \delta\ H_2O$.

Figure 5a shows δ as a function of operating temperature. Reducibility increases from 300^oC to 400^oC due to the expected improvement in kinetics at higher temperature. With further increase in temperature from 400^oC to 700^oC, reducibility is observed to decrease which can be explained by the sintering of the ceria particles, as confirmed in TEM images of the CeO_2 carriers after 3 cycles of CLC at various temperatures (Figure 5b-e). At the experimental conditions, reduction of the ceria particles is strongly limited by the slow oxygen diffusion in the oxygen sub-lattice of ceria. The strong increase in particle size and the concomitant reduction in specific surface area hence result in a significant reduction of accessible oxygen over the 30 min of the reduction phase, and hence in an effective loss of reducibility of the sample.

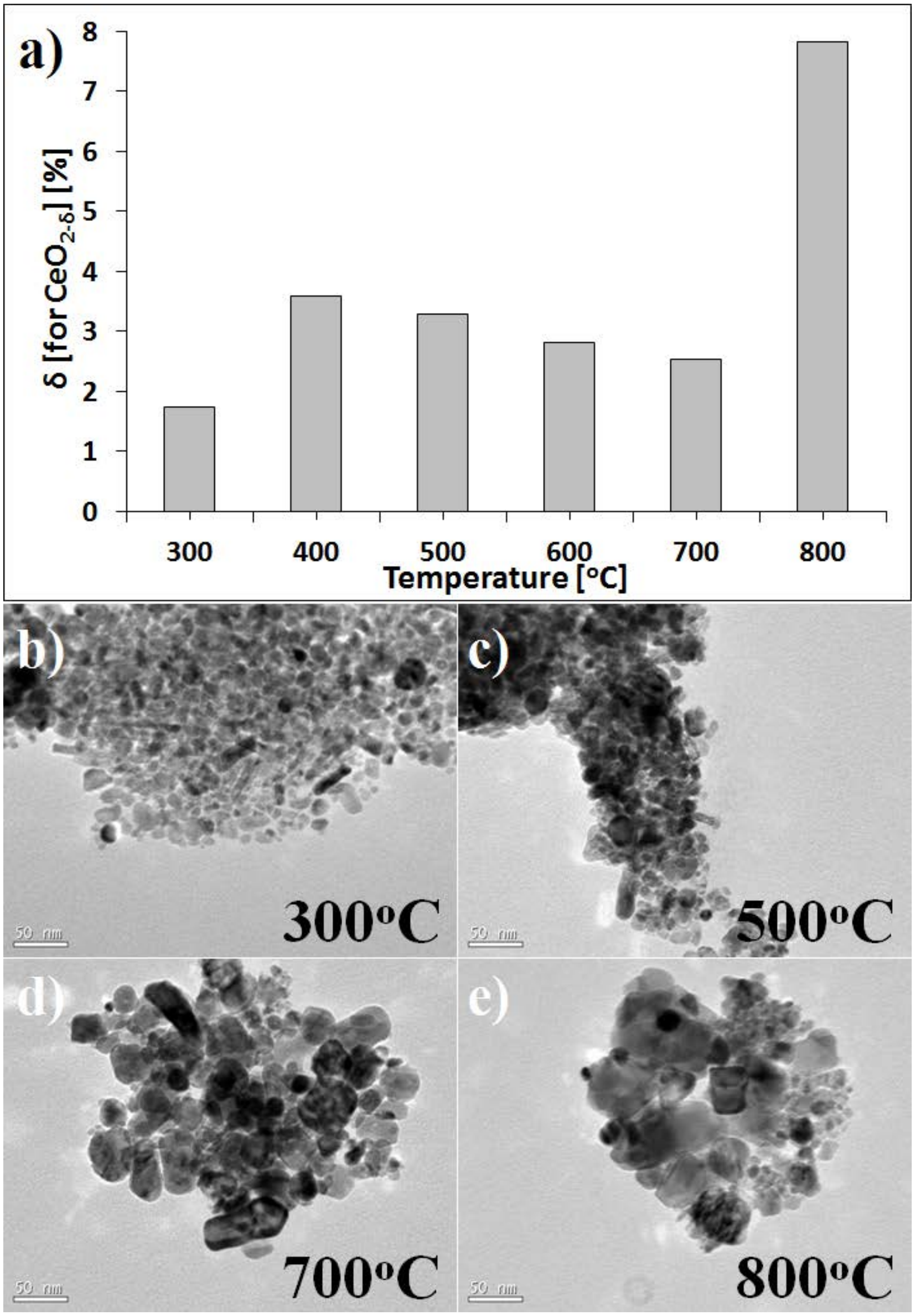

Figure 5. a) Effect of temperature on degree of reduction 'δ' for CeO_2 nanorods, during $CeO_2 + \delta\ H_2 = CeO_{2-\delta} + \delta\ H_2O$ in TGA under flow of H_2 (20 sccm); Typical TEM micrographs of CeO_2 nanorods (scale bar = 50 nm) after 3 cycles of CLC in TGA with H_2 as fuel (20 sccm) and air as oxidant (20 sccm) at b) 300°C, c) 500°C, d) 700°C, e) 800°C. As expected, the nanorod morphology is unstable at the periodic redox conditions of CLC.

Further increasing the temperature to 800°C, results in a sharp rise in reducibility (δ ~ 8%) due to accessibility of bulk CeO_2 at elevated temperatures (i.e. the strong acceleration of oxygen bulk diffusion). In contrast to CeO_2, La_2O_3 does not show any significant reducibility over the temperature range of 600 – 800°C (Figure 6). Both trends in reducibility of ceria and lanthana are in good agreement with results from H_2-TPR experiments for similar oxides reported previously[106].

Despite the observation of some reducibility of ceria, the amount of oxygen release (~0.7 wt.% of the oxide at 800°C) is too small to be of interest for CLC. While ceria (and lanthana) are hence not of interest as independent oxygen carrier in themselves, their potential as "promoting" support structures was further evaluated, using Ni as "active metal".

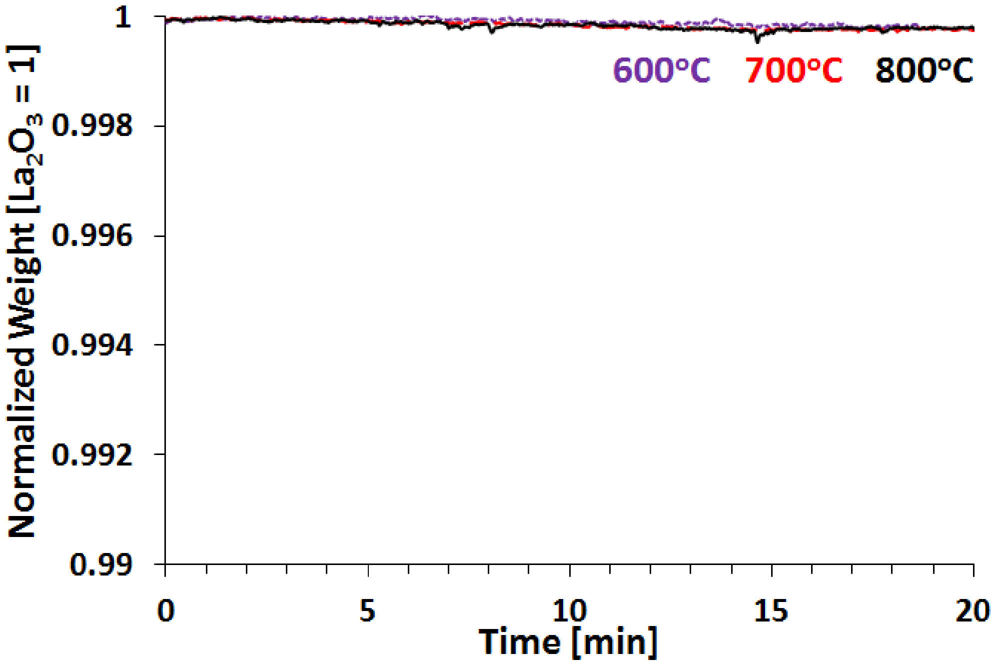

Figure 6. Normalized weight of La_2O_3 as a function of time subjected to reduction in TGA at 600, 700 and 900°C using H_2 as fuel (20 sccm). Unlike CeO_2, La_2O_3 does not show any significant reducibility over the entire temperature range which is confirmed by almost no drop in weight during reduction.

2.2.2 Reactive tests of Ni-based carriers in TGA

2.2.2.1 Reactivity and Stability tests at 800 and 900°C

Ni-based carriers were subjected to cyclic CLC tests in TGA at 800°C to examine their reactivity and thermal stability. As above, the carriers were reduced in H_2 (10 min) and then oxidized in air (15 min) with a N_2 purge (10-15 min) between the two half cycles. Figure 7 shows ten redox cycles for Ni-CeO_2 in TGA at 800°C. One can see the stable periodic operation of the carrier illustrated by the reproducibility of the alternating patterns of redox half cycles with identical carrier weights in the fully oxidized and reduced states, respectively.

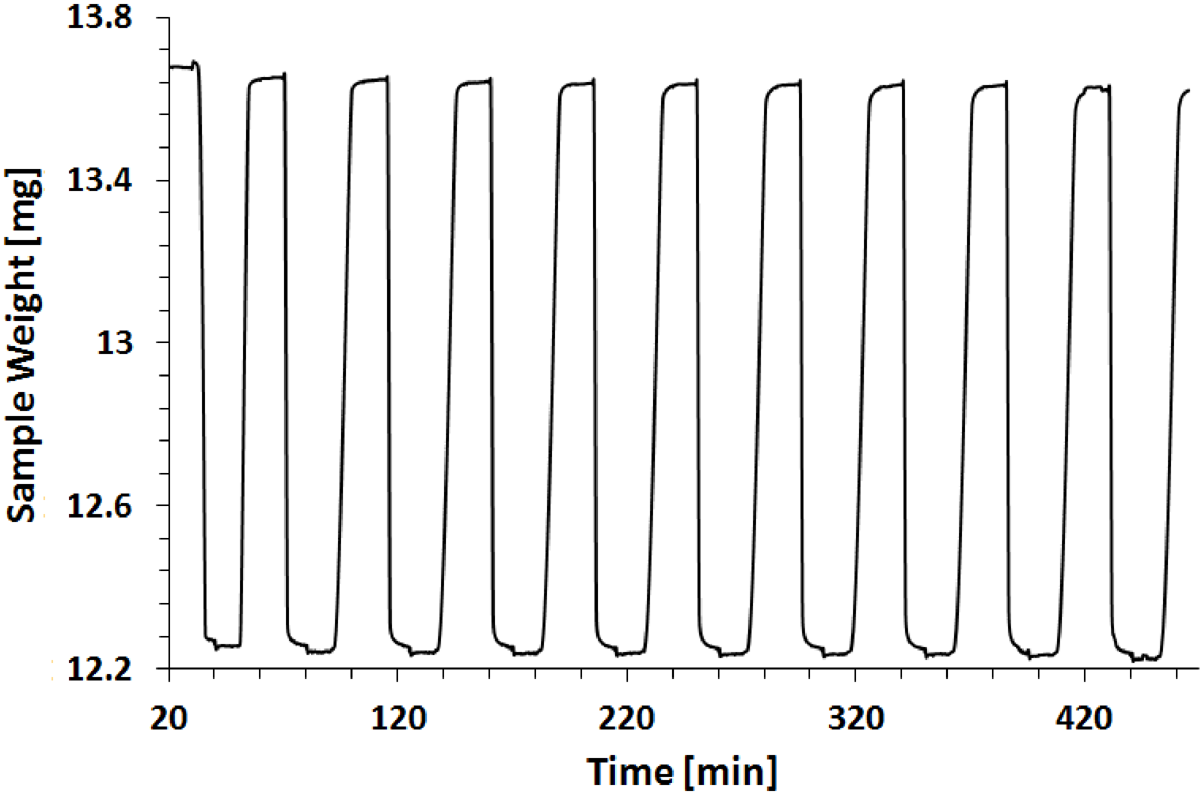

Figure 7. Multiple CLC redox cycles for Ni-CeO_2 in TGA operation at 800°C with reduction in H_2, N_2 purge, and air oxidation (20 sccm).

Similarly, Ni-La_2O_3, Ni-Al_2O_3 and Ni-SiO_2 were evaluated for thermal stability in TGA over 10 cycles at identical operating conditions. Figure 8 shows comparison of carrier conversion (X) profiles as a function of time for 10th reduction half cycle for all carriers, where X is defined as: $X = (W - W_{red})/(W_{ox} - W_{red})$. In this equation, W is the momentary weight of the carrier, W_{ox} is carrier weight in the fully oxidized state, and W_{red} represents the carrier weight in the fully reduced state, calculated based on a full reduction of active metal only. Thus $X = 1$ represents the oxygen carrier in the fully oxidized state and $X = 0$ the active metal in oxygen carrier in the completely reduced state (without any contribution of the reducibility of the support). Significant contributions of the reducibility of the support would hence result in $X < 0$ due to further decrease in carrier weight.

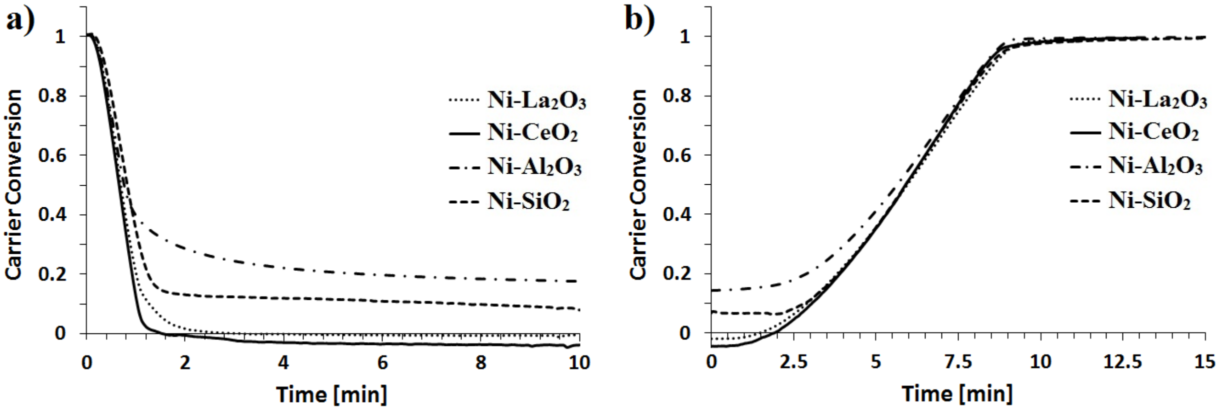

Figure 8. Comparison of carrier conversion as a function of time for various Ni-based carriers during a) reduction half cycle and b) oxidation half cycles for CLC operation in TGA at 800°C with reduction in H_2, N_2 purge and air oxidation (20 sccm).

Although all carriers show stable performance at 800°C, only reducible support based carriers show complete carrier utilization (indicated by a drop of X to zero, Figure 8a). Due to the reducibility of support in Ni-CeO_2, carrier conversion in this case drops even slightly below zero, indicating a small contribution of the CeO_2 oxygen reservoir in addition to NiO during reduction. From this “undershoot” of the conversion; we determine a degree of reduction ‘δ’ over ten cycles of 9.4 %, in good agreement with the 8% reducibility obtained above for pure CeO_2 at 800°C. More significantly, reduction of Ni-CeO_2 is very fast with essentially complete conversion in less than 2 min. In agreement with our observation above that La_2O_3 shows negligible reducibility over the temperature range of the present experiments, Ni-La_2O_3 carriers show complete carrier conversion but no significant additional reduction below X=0. However, although the reducibility of ceria and lanthana supports is insignificant in comparison to NiO, both carriers show complete utilization of carrier in the reduction half cycle, while the carriers based on non-reducible supports, Ni-Al_2O_3 and Ni-SiO_2, show only ~83% and ~92% conversion, respectively, and significantly slower reduction kinetics.

Figure 8b shows a comparison of conversion profiles as a function of time during re-oxidation of the carriers, using the 10th oxidation half cycle for all carriers. Interestingly, the oxidation kinetics is much more similar between the carriers than the reduction kinetics. All carriers undergo complete oxidation (i.e. reach X = 1) with almost identical conversion traces (with only a slightly slower kinetics for the silica-supported carrier).

All carriers were characterized post reactive tests by BET and XRD. Table 2 summarizes the data after the first and after 10 sequential CLC cycles. After the first cycle, XRD shows some sintering of the Ni crystallites, which continues over the full ten cycles (with roughly a doubling of particle size), but all carriers lie in the same range of ~14-18 nm after the first cycle and 20-24 nm after 10 cycles. Only two of the supports were sufficiently crystalline to allow size evaluation of the supporting oxide via XRD (alumina and ceria). Again, most of the sintering occurs over the first cycle, i.e. as a result of first exposure to the high reaction temperature. Interestingly, while the alumina support appears highly stable, ceria particle size almost doubles, without, however, this size increase affecting the observable redox kinetics. XRD patterns of post-reaction oxidized Ni-CeO_2 indicates the presence of only NiO and CeO_2 (Figure 9a). On the other hand, used oxidized Ni-La_2O_3 shows the presence of NiO and La_2NiO_4 (Figure 9b). Surprisingly, the formation of the mixed oxide La_2NiO_4 does not seem to affect the performance of the carrier, suggesting a full reversibility of the formation of La_2NiO_4 during reduction, as also confirmed by XRD (not shown here). The presence of $La(OH)_3$ in XRD is most likely due to the reactivity of La_2O_3 with moisture during transfer of the sample from the TGA to XRD for analysis[107]. The non-reducible supports (Figure 9c, d) show presence of Ni and NiO, confirming the incomplete reduction of the carriers.

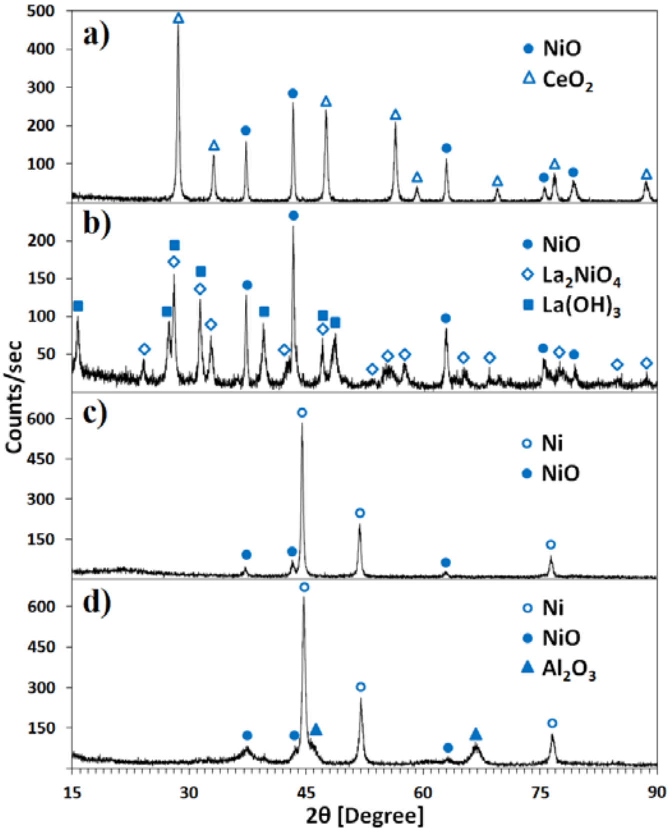

Figure 9. Typical XRD patterns after 10 cycles of CLC in TGA at 800°C with reduction in H_2, N_2 purge and air oxidation (20 sccm) for a) Ni-CeO_2 and b) Ni-La_2O_3, in oxide state; c) Ni-Al_2O_3 and d) Ni-SiO_2, after reduction half cycle detect NiO indicating incomplete reduction.

Similar tests were conducted at 900^oC at otherwise identical experimental conditions to identify the thermal stability of these carriers at slightly higher temperatures. Surprisingly, all carriers continued to show stable performance for 10 cycles for CLC in TGA, with the expected enhancement in redox kinetics, and in carrier conversion for Ni-Al_2O_3 (~83% to ~90%) and Ni-SiO_2 (~92% to 100%). CeO_2 and La_2O_3 based carriers showed complete carrier conversion with an increase in reducibility for CeO_2 to $\delta \sim 14.7\%$.

2.2.2.2 Reactivity tests at 350^oC

To fully elucidate the difference in intrinsic carrier reactivity, further tests were conducted at very low temperature (350^oC) in order to slow down the redox kinetics and hence enhance the difference between the different carriers. Figure 10a and b show a comparison of carrier conversion profiles for reduction and oxidation half cycles for CLC operated in TGA at 350^oC with H_2. As before, Ni-CeO_2 and Ni-La_2O_3 show complete carrier utilization with fast reduction kinetics (~80% carrier conversion in less than 15 min) even at this low temperature. In contrast, Ni-Al_2O_3 and Ni-SiO_2 show much slower reduction kinetics with incomplete carrier conversion (~77% for Ni-Al_2O_3 and ~98% for Ni-SiO_2) in 90 min. Interestingly, the oxidation kinetics is much less affected by temperature for all four carriers: All the carriers show again similar oxidation behavior with an initial period of rapid oxidation followed by slower rate at high conversions. Ni-La_2O_3 stands out by showing fast oxidation in ~13 min. all the way to full carrier oxidation, while all other carriers show incomplete oxidation at the end of 90 min.

Overall, the TGA tests hence demonstrate that reducible supports enable faster reduction kinetics and significantly higher oxygen utilization than non-reducible supports. Moreover, Ni-CeO_2 shows a higher degree of reducibility compared to Ni-La_2O_3. Post-reactive characterization shows that all carriers except Ni-Al_2O_3 displayed signs of moderate sintering with significant loss of surface area, underscoring the superior thermal stability of Al_2O_3 supports. Based on this, Ni-Al_2O_3 and Ni-CeO_2 were chosen for further tests using CH_4 as fuel.

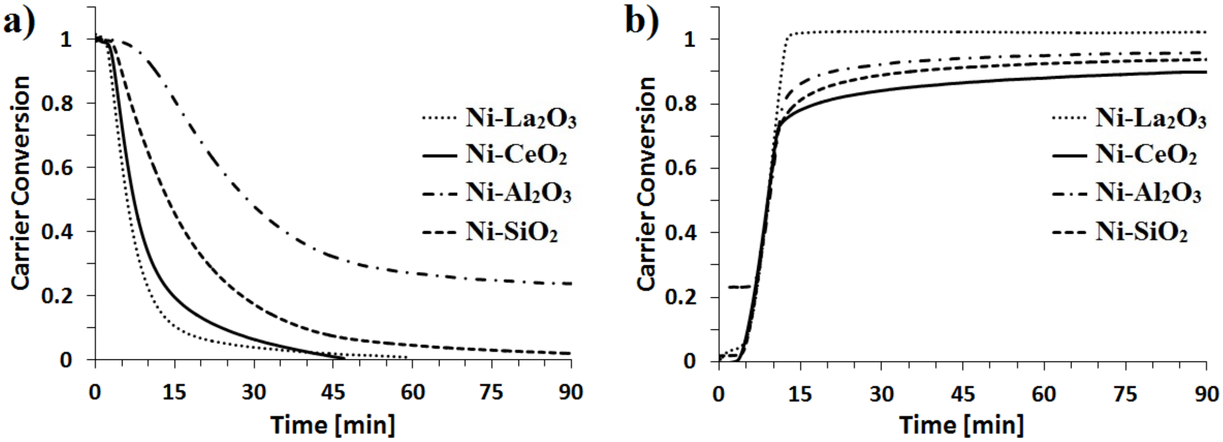

Figure 10. Comparison of carrier conversion as a function of time for various Ni-based carriers during a) reduction half cycle and b) oxidation half cycles for CLC operation in TGA at 350°C with reduction in H_2, N_2 purge and air oxidation (20 sccm).

2.2.3 Reactive tests with CH_4 as fuel in TGA

As above, both selected carriers were first evaluated in multi-cycle TGA tests at 800°C with CH_4 as fuel for 10 cycles. Both carriers showed stable operation over the time frame of the experiment (total of ~6-7 h). Figure 11 shows carrier conversion as a function of time for Ni-CeO_2 and Ni-Al_2O_3 over a single redox cycle. It can be observed that both carriers show fast reduction kinetics, but only Ni-CeO_2 completely utilizes the available oxygen carrying capacity while Ni-Al_2O_3 shows only ~75% carrier conversion. Moreover, carrier conversion again drops below zero for Ni-CeO_2, indicating contributions of CeO_2 reducibility during reduction (with $\delta \sim$ 2.7%). The lower reducibility for CeO_2 compared to the experiments with H_2 above is likely due to the shorter period of exposure and lower flow rate of the reducing gas (2.5 min of 5 sccm CH_4

vs 10 min 20 sccm H_2). During the oxidation half-cycle both carriers show again similar kinetics and the ability to fully regenerate the oxide state.

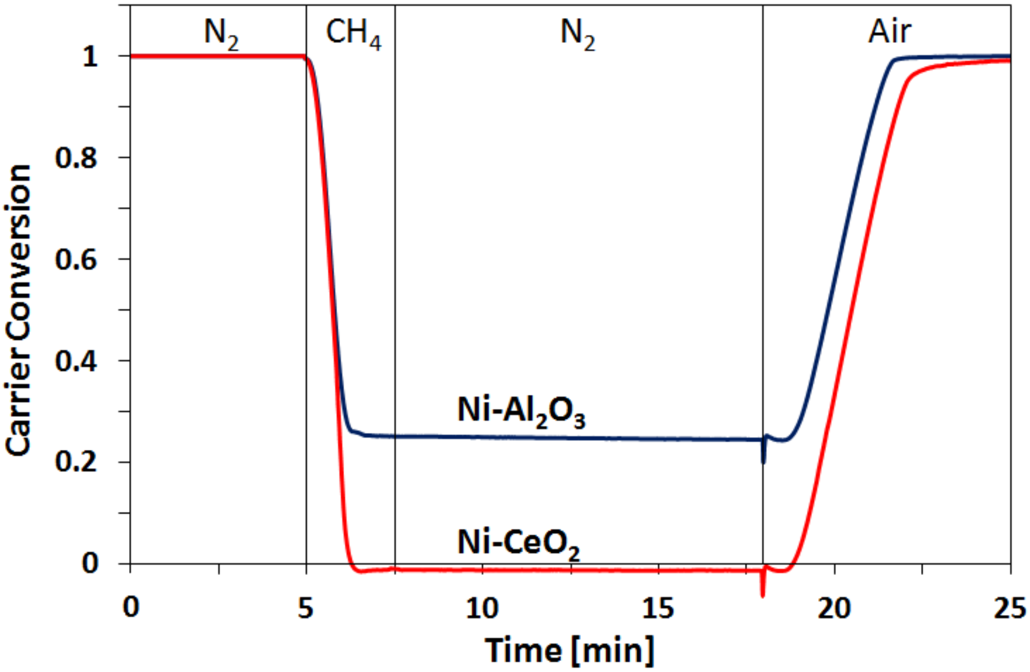

Figure 11. Comparison of conversion profiles for tenth redox cycle of Ni-CeO_2 and Ni-Al_2O_3 for CLC operation in TGA at 800°C with reduction in CH_4 (2.5 min, 5 sccm), N_2 purge and air oxidation (20 sccm).

Post-reactive characterization via XRD and TEM showed only NiO and CeO_2 or Al_2O_3, respectively, i.e. no formation of spinel phases was observed. The average crystallite size of NiO calculated from XRD revealed moderate sintering from 12.7 nm to 23.1 nm for Ni-CeO_2 and 9.7 nm to 19.8 nm for Ni-Al_2O_3. Ceria crystallite size was observed to increase from 9.6 nm (freshly calcined sample) to 17.2 nm, while alumina showed slightly less increase from 6.9 nm to 9.8 nm. As in the reactive tests with H_2 as fuel, alumina-based carriers hence again show better thermal stability, while ceria results in a strong enhancement in Ni reactivity and thus results in complete carrier utilization, indicating that the reducibility of CeO_2 plays an important role in augmenting the carrier performance.

2.2.4 Reactive Tests in fixed-bed reactor

While TGA studies highlight the difference in the reducible and non-reducible carriers based on carrier conversions, these tests are conducted with a large excess of reactive gas stream and thus do not allow access to the conversion of the fuel nor the selectivity of the reaction towards total oxidation, both of which are critical for efficient CLC operation. Further studies were hence conducted in a fixed-bed reactor to evaluate the efficacy of these carriers to completely and selectively combust CH_4 to CO_2 and H_2O during the reduction half cycle

2.2.4.1 Extended reduction in CH_4

As a first step, tests with an extended reduction period (20 min) were carried out to understand the combustion products as a function of carrier oxidation state and to determine a suitable time-window for cyclic fixed-bed reactor operation.

Figure 12a, b shows the concentration profiles during reduction half cycle in fixed-bed reactor operation at 800^{o}C for Ni-CeO_2 and Ni-Al_2O_3 respectively. Ni-CeO_2 (Figure 12a) shows an initial period of reduction (~3-4 min) selective to complete combustion of methane, indicated by a dominant, steady signal for CO_2 , followed by a sharp transition from complete combustion to partial oxidation characterized by the rapid disappearance of the CO_2 signal and simultaneous formation of H_2 and CO. While the CO concentration goes through a maximum at ~5-6 min. and then falls off towards low concentrations at t~10 min., the H_2 concentration stays at a constant, high level throughout the duration of the reduction phase, indicating a transition of the reaction to methane cracking for the strongly reduced carrier.

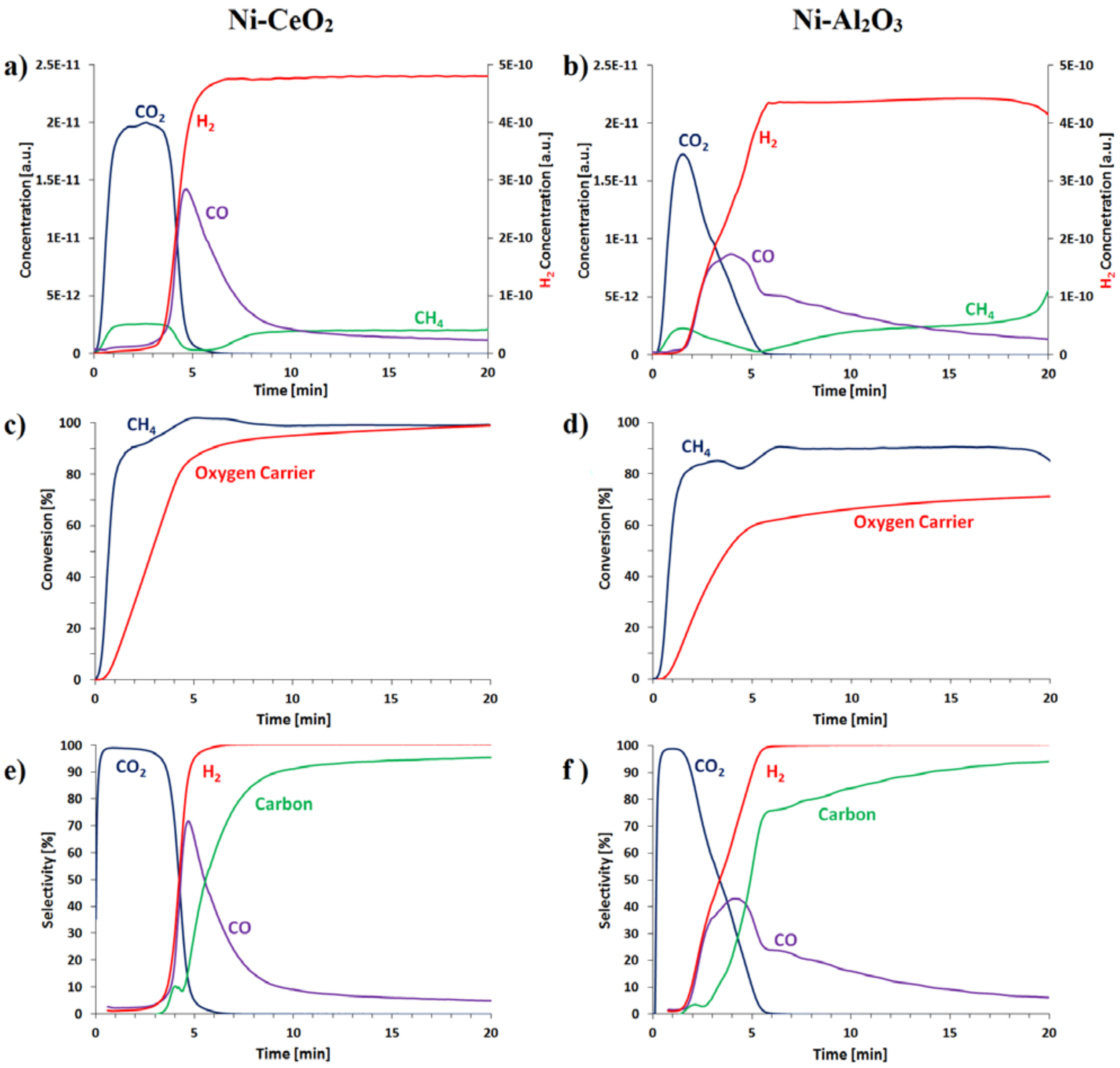

Figure 12. Concentration traces (a & b), CH_4 and oxygen carrier conversion (c & d), and instantaneous selectivity (e & f) as a function of time during an extended reduction (20 min) for Ni-CeO_2 (left column; a, c, e) and Ni-Al_2O_3 (right column; b, d, f) in fixed-bed reactor operation at 800^{o}C with CH_4 in Ar (1 sccm, $y_{CH4} = 16.7\%$).

The same experiment with Ni-Al_2O_3 (Figure 12b) shows a similar succession of these three reaction pathways, but with much less well-defined transitions: A very narrow window with high selectivity for total oxidation (t<1-1.5 min) is followed by relatively weak and prolonged activity for partial oxidation, which overlaps with some residual total oxidation activity, and finally a broad tailing off of CO indicates a transition to significant methane cracking. Interestingly, while Ni-CeO_2 was able to maintain the cracking activity for an extended period of time (>10 min.) without any sign of deactivation due to carbon deposition, Ni-Al_2O_3 shows a drop in catalytic activity for methane cracking by the end of the 20 min of reduction (i.e. during the last minute from 19-20 min. operation), indicated by drop in H_2 signal and simultaneous increase in methane concentration.

Figure 12c-f show these results in terms of (instantaneous) conversion (Figure 12c, d) and selectivity (Figure 12e, f) for Ni-CeO_2 and Ni-Al_2O_3, respectively. Ni-CeO_2 (Figure 12c) shows ~90% fuel conversion during the initial reduction period which is selective to complete combustion as indicated by the broad plateau at 100% CO_2 selectivity over the first ~4 min. (Figure 12e). This is followed by almost complete conversion during the subsequent partial oxidation phase, during which CO and H_2 selectivity increase at essentially identical values up to a maximum in CO selectivity at ~5 min. The identical values for CO and H_2 selectivity suggest that the reaction proceeds in fact along a direct partial oxidation pathway, rather than an initial total oxidation followed by reforming reactions, as often observed in catalytic partial oxidation[108]. Somewhat surprisingly, this also indicates that Ni-CeO_2 is not a very selective catalyst/carrier for partial oxidation under the conditions of chemical looping, despite its well-known catalytic activity and selectivity for partial oxidation in a conventional steady-state reactor set-up where oxygen is fed as molecular oxygen rather than lattice oxygen.

While H_2 selectivity continues to rise to 100%, CO selectivity peaks at ~70% and then falls off rapidly, indicating the formation of carbon as main reaction product, i.e. methane cracking as main reaction path.

The carrier conversion mirrors these trends, increasing linearly to ~80% over the first 5 min of the reduction phase, after which it increases much more slowly towards ~100% at the end of the reduction cycle. Clearly, transition to methane cracking is associated with a largely reduced carrier, i.e. an oxygen starved reaction. Surprisingly, this does not reduce the rate of methane conversion, which remains at ~100% despite the large carbon build-up which is associated with methane cracking.

In contrast to that, Ni-Al_2O_3 (Figure 12d) shows only ~80% fuel conversion with only ~12% carrier conversion during the brief initial reduction period which is selective to complete combustion on this carrier (1 min). Moreover, only ~72% of the oxygen carrier is utilized by the end of reduction half cycle, in agreement with the incomplete carrier conversion observed with H_2 and CH_4 as fuels in the TGA studies at the same temperature. Selectivities (Figure 12f) again show the trends discussed above, i.e. a much shorter initial phase with high selectivity for total oxidation, followed by a period where selectivity for total oxidation and partial oxidation strongly overlap, and finally a transition to methane cracking, which is also more gradual than for the ceria-supported carrier. Interestingly, both CO and C selectivity show a rather discontinuous break in the curves at the point where CO_2 formation stops. Such a break is absent for the ceria-supported carrier (Figure 12e).

While we have no direct evidence for a molecular-level explanation of this observation, it seems reasonable to assume that at this point the surface of the Ni particles is completely reduced, and an oxygen starved reaction proceeds largely via methane cracking, with a small amount of CO formation continuing as bulk oxygen is slowly supplied from the core of the Ni/NiO nanoparticles. Since this bulk diffusion process will be much slower than the catalytic surface reaction at these high reaction temperatures, it does not keep up with the carbon deposition and hence the carrier gets ultimately poisoned by carbon, as indicated in the drop-off on methane conversion towards the end of the cycle (Figure 12d). This is also in agreement with the fact that the carrier conversion for the alumina-supported carrier shows a rather abrupt transition from a fast increase in conversion to a much slower increase at around the same point in time (t ~ 5 min.), as the slow bulk diffusion of oxygen strongly limits the rate of conversion.

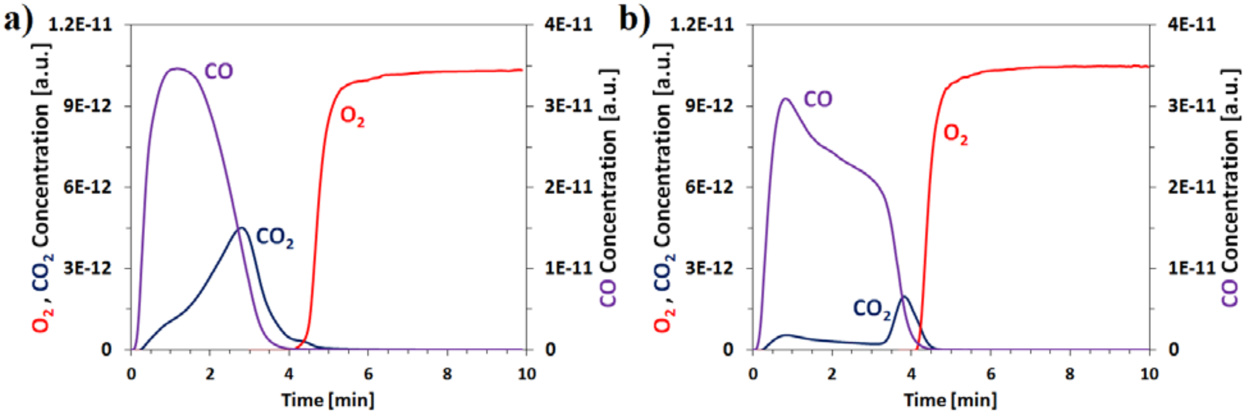

Figure 13. Concentration traces of CO, CO_2, and O_2 during re-oxidation (with air at 800°C) of Ni-CeO_2 (a) and Ni-Al_2O_3 (b) after extended reduction in methane.

The fact that the carrier contained significant amounts of carbon at the end of the extended reduction experiment was confirmed by purging the reactor with argon and then oxidizing the carrier in air (Figure 13). During this oxidation the evolution of large amounts of CO and CO_2 was observed for both carrier materials, indicating burn-off of carbonaceous residues. Once the carbon burn-off was complete, the carriers could be fully re-oxidized in both cases, i.e. despite the large amounts of carbon, carrier regeneration appeared to be unhampered (albeit, aside from the undesired carbon carry-over, in a technical environment, one would expect large hot spots due to the carbon burn-off with detrimental impact on carrier stability and durability).

2.2.4.2 Multi-cycle Fixed-bed CLC Operation

Based on the above discussed results from extended reduction of the carriers with methane, time windows for reduction half cycles were determined for multi-cycle fixed-bed CLC tests using Ni-CeO_2 and Ni-Al_2O_3. Since CLC requires high selectivity towards total combustion of methane in order to avoid dilution of the product stream with non-condensable gases, reduction periods of 3 min and 1 min, were chosen for Ni-CeO_2 and Ni-Al_2O_3, respectively, with an oxidation phase of 5 min (using air), and other experimental conditions as before.

Figure 14 shows the results for Ni-CeO_2 (top row) and Ni-Al_2O_3 (bottom row) during a single reduction (left column) and oxidation half-cycle (right column). Concentration profiles and instantaneous methane conversion are shown again as a function of time. As before, we observe high selectivity towards total oxidation due to the high oxidation state of the carrier, with only minor production of small amounts of H_2 and CO. A methane conversion of ~90% is achieved for Ni-CeO_2 vs ~80% for Ni-Al_2O_3 (dotted lines in Figure 14a, c), at carrier conversions of ~53% and ~14%, respectively, at the end of the reduction half cycle. The very low carrier utilization for the alumina-based carrier is due to a combination of the lower reactivity (i.e. lower methane conversion) as well as the much shorter duration of the reduction phase, which is necessitated by the rapid onset of partial oxidation reactions for this carrier (cp. Figure 12f). It should also be noted that the necessary restriction of the operation of this carrier to only one minute duration of the reduction phase results in concentration traces being largely dominated by dispersion effects in the reactor set-up during the switching from purge to production phases. While in a technical reactor such effects could be minimized (no such attempt was done here), this further underscores that a carrier with such a narrow operation window is unlikely to find industrial application.

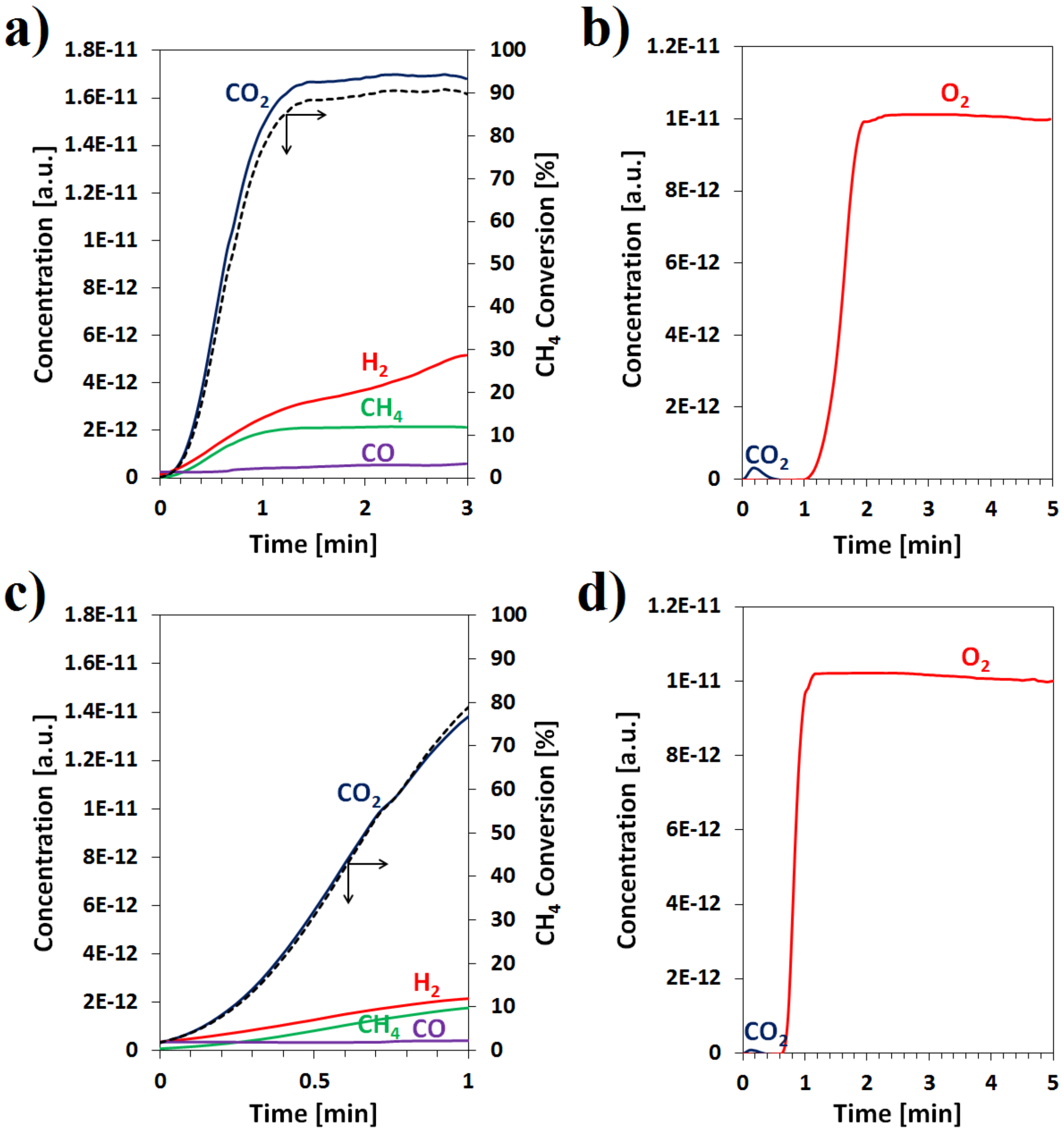

Figure 14. Concentration traces and methane conversion vs time (dashed lines) during the reduction half cycle with CH_4 (1 sccm, y_{CH4} = 16.7mol% in Ar; left column) and concentration traces during the oxidation half cycle with air (20 sccm; right column) during CLC operation in a fixed-bed reactor configuration at 800°C for Ni-CeO_2 (top row; a and b) and Ni-Al_2O_3; (bottom row; c and d).

The concentration time traces during re-oxidation show essentially identical behavior: Oxygen is completely consumed initially, before a sharp oxygen break-through indicates complete carrier re-oxidation. Due to the lower degree of carrier utilization, this break-through occurs sooner over the alumina-based carrier than over the ceria-based one (~0.6 min. vs ~ 1.8 min). In both cases, a small amount of CO_2 at the on-set of the re-oxidation indicates carbon burn-off and hence the presence of a small amount of carbonaceous residue on both carriers. However, the amount of carbon carryover from the reduction half cycle was near the detection limit of our mass spectrometer, and our carbon balance indicates >99% efficiency for carbon capture during the reduction half cycles for both the carriers.

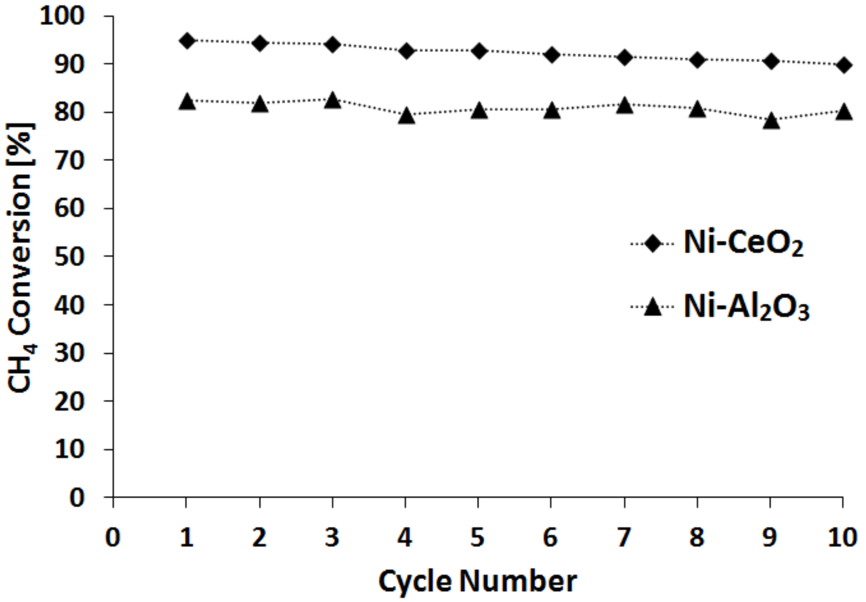

Figure 15. CH_4 conversion versus cycle number during fixed-bed CLC operation at 800°C using methane as fuel (1 sccm, y_{CH4} = 16.7%; reduction time of 3 min for Ni-CeO_2 and 1 min for Ni-Al_2O_3.) and oxidation in air (20 sccm).

Along-with carrier reactivity, their thermal stability in cyclic redox operation is crucial for long-term continuous operation of CLC. Figure 15 hence shows the methane conversion, at the end of reduction half cycle, for both carriers versus cycle number. It can be seen that Ni-

CeO_2 shows overall higher methane conversion (~90-94%) than Ni-Al_2O_3 (~80-82%) over the timeframe of the experiment. More significantly, however, Ni-Al_2O_3 shows stable operation, while conversions over Ni-CeO_2 show a slight, but continuous, decrease.

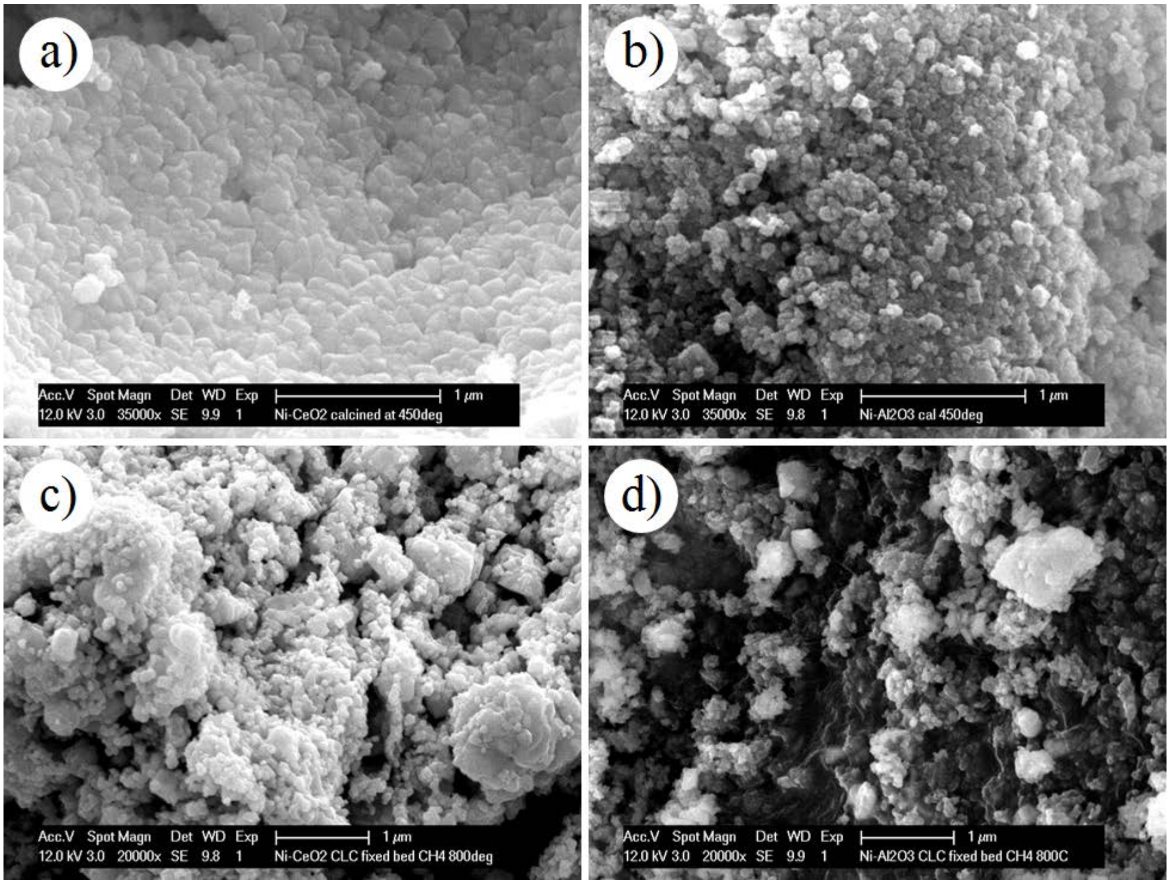

Figure 16. SEM micrographs of Ni-CeO_2 (left column, a and c) and Ni-Al_2O_3 (right column, b and d) after calcination at 450^oC in air for 2 h (top row; scale bar = 1 µm at 35000X magnification); and post fixed-bed CLC operation at 800^oC (bottom row; scale bar = 1 µm at 20000X magnification).

Post-reactive characterization suggests that this slow deactivation for Ni-CeO_2 can be attributed to a (partial) loss of the microstructure of the carrier due to sintering of the ceria support. While XRD analysis of the carriers detected only NiO and CeO_2 or Al_2O_3, suggesting that the individual phases are stable, BET analysis of the Ni-CeO_2 post fixed-bed reactive tests shows a surprisingly severe reduction in surface area from 45.5 to 4.1 m^2/g, whereas Ni-Al_2O_3

carriers show only moderate reduction in surface area from 47.4 to 17.8 m^2/g. SEM micrographs of oxygen carriers (Figure 16) before and after the fixed-bed reactor tests confirm the higher extent of grain growth for ceria-based carriers compared to alumina. Thus, while Ni-CeO_2 shows better reactivity, higher fuel conversion and carrier utilization and, importantly, a broader window of operation for complete combustion compared to Ni-Al_2O_3, it lacks thermal stability at elevated temperature, with some deactivation already apparent over as little as ten cycles of periodic operation. Thus, further work is needed to counter the issue of low thermal stability of ceria[98-99, 109-110] to make the ceria based carriers a more practical option of oxygen carriers.

2.3 SUMMARY

The study in this chapter aimed to evaluating the impact of using reducible oxides (such as CeO_2 and La_2O_3) as oxygen carriers or support materials for CLC in place of widely used non-reducible supports. Towards this end, we conducted a comparative study of reducible (CeO_2, La_2O_3) and non-reducible (Al_2O_3, SiO_2) supports, using Ni as a widely studied “model” for an active metal.

Ceria, in particular, is widely used as promoter and as catalyst support in oxidation reactions due to the fact that, unlike many traditional support materials, cerium oxide plays an important active role as an oxygen storage and transfer material in redox reactions based on the facile and reversible release of lattice oxygen during conversion between Ce^{4+} and Ce^{3+} [111]. Moreover ceria has been shown to enhance the catalytic activity of supported metal particles via strong metal support interactions[112], which motivated the present study into the use of reducible oxides as “active” support matrices in CLC.

Although CeO_2 itself showed some reducibility at higher temperature 800°C, the available oxygen reservoir of such simple reducible oxides is miniscule relative to the oxygen carrying capacity of typical metals. However, we found a pronounced activating effect of reducible oxides on Ni as a typical metal for oxygen carrying purposes: Ni supported on reducible oxides (CeO_2, La_2O_3) showed somewhat accelerated reduction kinetics and, most importantly, significantly enhanced oxygen utilization compared to Ni on conventional, non-reducible oxide supports (Al_2O_3, SiO_2).

A detailed comparison between Ni-CeO_2 and Ni-Al_2O_3 furthermore showed that the ceria-supported carrier displays distinct phases of methane conversion via total oxidation, partial oxidation, and methane cracking, with sharp transitions between these phases based on the oxidation state of the carrier. Ni-Al_2O_3 shows similar phases, but with much less distinct transitions and strong overlap between subsequent phases, which limits its usefulness in practical application. For Ni-CeO_2, it was possible to achieve >90% methane conversion at ~56% carrier utilization and >90% selectivity for complete combustion with negligible carbon formation in cyclic fixed-bed CLC operation at 800°C. However, significant loss in surface area and a drop in methane conversion from 94% to 90% over ten cycles indicate that Ni-CeO_2 does not possess the required stability to become an industrial carrier. This underlying degradation of textural properties and subsequently depression of redox properties of ceria has been observed before[109-110], and the presence of a reducing environment is known to further exacerbate sintering of ceria[113].

While these initial results using reducible supports hence show an intriguing potential for these materials, they also indicate that ceria must be stabilized in order to make it a viable technical support at the harsh high-temperature conditions of CLC. It is well established that doping ceria with a aliovalent metal can arrest the thermal degradation of ceria by maintaining higher surface area even after high temperature thermal treatment and preserving oxygen defects[98-99, 109-110] while also yielding a further enhancement of oxygen mobility and hence reducibility via lowering the energy for vacancy formation[114]. This has been successfully demonstrated previously in catalysis studies using both Zr and La as dopants[96, 98, 109]. Interestingly, DFT study of NiO-CeO_2 have also identified such an effect due to interstitial substitution of Ni in a solid solution of NiO-CeO_2[111], albeit we found no indication of such substitution in our studies.

We have previously observed an increase in catalyst activity for water gas shift which correlated closely support reducibility upon doping the ceria supports with La[96, 106]. Intriguingly, we observed in the present study during the low-temperature oxidation half-cycle (at 350°C) that only Ni-La_2O_3 showed complete re-oxidation, suggesting that La_2O_3 aids in oxidation of the carrier, while CeO_2 had the strongest effect on reduction. Hence, doping ceria with lanthana might not only result in a thermal stabilization of the carrier, but could yield synergistic effects in both oxidation and reduction of the carrier material. Experiments to verify this hypothesis are discussed in section 7.2.2.

Finally, it is tempting to speculate on the reason for the strong enhancement of metal utilization on reducible supports. While our experiments give no direct evidence for a mechanistic explanation, the pronounced differences between Ni-CeO_2 and Ni-alumina could be an indication of a different oxygen transport mechanism: If oxygen diffusion from the bulk to the surface of the Ni particles is limiting the conversion on alumina, as discussed above, and this limitation is absent on ceria, it suggest that a different oxygen transport pathway is present in this carrier, since the morphology of both types of carriers was confirmed to be very similar (both in terms of surface area and, more importantly, Ni particle size, (see Table 2). Since oxygen mobility in ceria, in particular in near-surface layers, is known to be high, we hypothesize that increased utilization of the Ni particles might be due to an enhanced oxygen transport from ceria to the supported Ni particle via the Ni-ceria interface. Oxidation of methane could hence occur via the following mechanism (Figure 17).

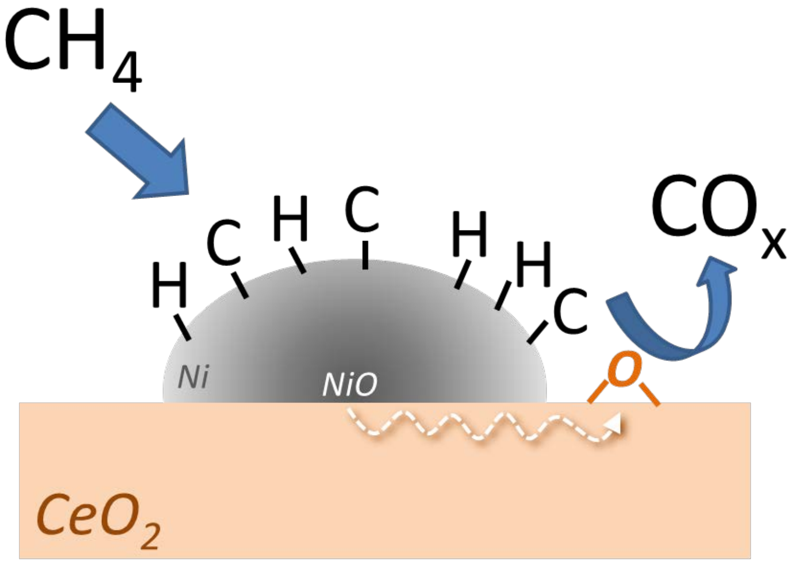

Figure 17. Schematic of a proposed mechanism for the enhanced metal utilization in CLC using reducible supports: Methane is cracked on the (reduced) metal particle surface, and the carbonaceous residue is oxidized in contact with lattice oxygen of the reducible support at the metal/support interface. The lattice oxygen is then replenished from the (still partially oxidized) core of the supported metal particle, resulting in deep reduction of the supported particle.

After reduction of the surface (and near-surface layers) of the NiO particles to the metallic state during the initial phase of the reduction half-cycle, oxygen diffusion in the metal particle becomes too slow to keep up with the surface reaction, resulting in methane cracking on the metallic Ni surface. For alumina-supported particles, this results in a slow deactivation of the carrier due to coking. For ceria-supported particles, however, the Ni-bound carbonaceous species can react at the perimeter of the Ni particles with lattice oxygen of ceria, effectively “gasifying” these species. The lost lattice oxygen is then refilled via oxygen from the (still partially oxidized) core of the Ni particle, resulting in a slow, but continuous further reduction of the Ni particle. Since diffusion is slow in virtually all metal/metal oxide systems of interest for reactive applications, such a mechanism would imply that similar enhancements should be observable upon utilization of reducible supports for essentially all metal-based oxygen carriers. Experiments to this effect are conducted in chapter 3.0 and 4.0 using different metal/s systems.

Overall, the result of the present study suggest that reducible oxides offer a promising path towards high performance oxygen carrier materials for CLC assuming that their thermal stability can be improved and that their attrition resistance—which was not studied in the present investigation—suffices for utilization in circulating fluidized beds, the most commonly proposed reactor configuration for CLC (albeit alternate concepts which impose much less demands on mechanical stability, such as moving bed and even fixed-bed reactors, are also being investigated for this process). Subsequent chapters (chapter 3.0 and 4.0) aim at investigating whether reducible supports have similar activating effects on other metals.

3.0 IRON AND BIMETALLIC IRON-NICKEL OXYGEN CARRIERS FOR CHEMICAL LOOPING COMBUSTION

As seen from previous study (chapter 2.0), Ni-based oxygen carriers are highly active in CLC. Ni-based oxygen carriers are also among the most thoroughly analyzed carriers for CLC due to their high reactivity and near complete fuel conversion when using methane as fuel. However, Ni-based carriers are hampered by high cost and the well-known toxicity of nickel. Among the various metals investigated for CLC, Fe has emerged as an attractive option due to its abundance, low cost, and low toxicity. However, its weak redox characteristics, low fuel conversion, and poor oxygen transport capacity (due to the inaccessibility of some of its oxidation states in practical CLC operation) constitute significant draw-backs. Thus the objective of the present study is to get the best of both the worlds, i.e., we aim at combining less reactive but low cost iron with highly active nickel to improve the carrier performance in CLC due to possible synergistic effects between iron and nickel.

More recently, mixed metal oxide carriers have found attention in CLC with the aim to increase carrier reactivity, improve fuel conversion, maintain carrier mechanical properties, and/or minimize the use of toxic metals. For Cu-Ni mixed oxides, it has been shown that the presence of CuO allows for full conversion of methane to CO_2 and H_2O, while presence of NiO helps to stabilize the low-melting CuO phase during CLC operation at 950^oC[48]. Similarly, in Al_2O_3-supported Co-Ni carriers, the addition of Co enhances the reducibility of the oxygen carrier by inhibiting particle agglomeration and minimizing the formation of stable Ni-aluminates[115-116]. Johansson et al.[117] reported that the addition of only 3% nickel oxide to a bed of iron oxide particles resulted in very high methane conversion, likely due to a catalytic effect of (metallic) Ni for methane reforming to syngas which can easily reduce iron oxide. Similarly, NiO and Fe_2O_3 mixed oxide carriers supported on bentonite were used in a circulating fluidized bed study by Son and Kim[118], and it was found again that carrier reactivity increases with increasing nickel content. Although these studies thus already showed beneficial effects through the use of mixed metal oxides, the carrier materials in most of these studies showed a significant degree of de-alloying, raising the question to what degree these results are due to simple coexistence of the two separate monometallic phases and how truly bimetallic carriers can be stabilized at the demanding conditions of CLC.

In the chapter, we report on a study in which we employ Fe-Ni bimetallic carriers (in the form of $NiFe_2$/$NiFe_2O_4$) with the aim to improve redox kinetics over Fe-based carriers via Ni addition while limiting the use of nickel. Furthermore, we compare the reactivity and stability of these bimetallic carriers on alumina and ceria as supports, respectively. Reducible supports, such as ceria, are widely used in applications such as redox catalysis, automotive exhaust abatement, and water gas shift. In all these applications, the promoting effect of ceria on the active metal phase of the catalyst is due to its oxygen storage capacity, i.e. the facile and reversible release of lattice oxygen via reduction of Ce^{4+} to Ce^{3+}. In chapter 2.0 we demonstrated that ceria can have a strong effect on oxygen carrier performance for monometallic nickel in chemical looping, thus allowing for a much more efficient utilization of the oxygen carrying capacity of the carriers compared to conventional supports[42]. Mono- and bimetallic carriers are subjected to CLC tests using H_2 and CH_4 as fuels in thermogravimetric analysis (TGA), and then further investigated in depth in fixed-bed reactor CLC tests. Our results show that alloying the metal phase can indeed significantly improve carrier reactivity and fuel conversion compared to monometallic iron-based carriers, and that the support matrix plays a crucial role in stability of bimetallic phase with the use of a reducible support strongly enhancing the utilization of the oxygen carrying capacity of the carrier metal.

3.1 EXPERIMENTAL

3.1.1 Carrier synthesis and characterization

Oxygen carriers were prepared in a simple two-step synthesis procedure. First, the support oxide powder was synthesized, followed by deposition of the respective metal(s) via incipient wetness or deposition precipitation technique.

Ceria was synthesized according to the procedure previously explained in section 2.1.1. Alumina (γ-Al_2O_3) (99+%, 80-120 m^2/g, Alfa Aesar) was obtained commercially and used as obtained. Fe-based carriers (40 wt.% Fe) were synthesized via simple deposition-precipitation technique. Briefly, $Fe(NO_3)_3.9H_2O$ (99+%, Sigma-Aldrich) was dissolved in DI water, and 40 mL of the 0.06 M precursor solution was precipitated by 0.5 M NaOH at pH of 9 – 9.5 on 200 mg of the desired support powder suspended in 100 mL DI water. After aging for 2 h, the resulting slurry was centrifuged, vacuum dried at 80 – 100^{o}C, crushed, and finally calcined in air between 450^{o}C and 800^{o}C for 2 h. Monometallic Ni and bimetallic $NiFe_2$ carriers with 40 wt.% metal were synthesized via incipient wetness described before (section 2.1.1). Obtained carriers were calcined at temperatures between 450^{o}C and 800^{o}C.

At this point it is noteworthy compare the total oxygen capacity of both iron and nickel: The theoretical oxygen carrying capacities of pure NiO (NiO ⇔ Ni) and Fe_2O_3 (Fe_2O_3 ⇔ Fe) carriers are 21.4 wt.% and 30 wt.%, respectively. Thus, ideally, iron offers more oxygen for combustion of fuel. But from subsequent set of reactive tests it can be seen practically iron provides much less amount of oxygen for total oxidation of methane.

The materials were characterized at various stages during the experiments e.g. after synthesis, after reactive tests in TGA, and after fixed-bed studies. The specific surface area was determined via nitrogen sorption in a Micromeritics ASAP 2020 gas adsorption analyzer using the BET method. Prior to the measurement, the samples were degassed for 2 h at 200^oC under high vacuum. Sample morphology was determined by TEM using a JOEL 200 electron microscope. Elemental composition and thus metal loading of oxygen carriers was determined by EDAX equipped on Philips XL-30 field emission SEM. XRD measurements were performed with a high-resolution powder X-ray diffractometer (Phillips PW1830) in line focus mode employing Cu Kα radiation (λ = 1.5418 Å) with typical 2θ scans between 15^o and 90^o. Crystal phases were identified based on JCPDS cards. Particle sizes were calculated from the Debye-Scherrer equation and average crystal lattice spacings were determined using Bragg's law.

3.1.2 Reactive tests

Kinetics and thermal stability of the carriers were evaluated in TGA tests (Perkin Elmer TGA-7). H_2 was initially used as a model fuel to characterize carrier performance during redox cycles and CLC tests were conducted with CH_4 as fuel at a fixed temperature of 800^oC to test for carrier selectivity and thermal stability with a particular focus on coke formation on the carriers which would result in undesired carbon carry-over from the reducer to the oxidizer. All experimental conditions were identical to as explained in section 2.1.2.

As a last step, fixed bed experiments were conducted to investigate the effectiveness of carriers for CH_4 conversion to H_2O and CO_2 – crucial for efficient CO_2 capture in CLC. Based on the results in the TGA tests, fixed-bed reactor tests focused entirely on ceria-based carriers, where operating conditions and experimental set-up for fixed-bed tests were kept identical to that of investigations using Ni-based carriers (chapter 2.0).

3.2 RESULTS AND DISCUSSION

3.2.1 Thermal stability of oxygen carriers

As well established from catalysis, the surface area of the materials and the dispersion of the metal phase can have significant impact on the reactivity of the carriers. Therefore, carrier materials were carefully characterized with regard to surface area, crystallinity, and metal particle size. Table 3 summarizes the key carrier characteristics for all Ni-, Fe-, and $NiFe_2$-based carriers tested in this study. Metal loading for all carriers determined by EDX is close to the targeted 40 wt.% metal and the ratio of Fe to Ni in the bimetallic carriers is also close to the stoichiometric ratio of 2 (for $NiFe_2$). The surface area of freshly synthesized CeO_2 samples after calcination at $450^{o}C$ is typically ~80 – 100 m^2/g, which is comparable to the surface area of the (commercially obtained) alumina powder (80 – 120 m^2/g). Irrespective of the nature of the supported metal, alumina-based carriers show significantly higher surface areas than their ceria counterparts. The smaller crystallite sizes of both metal and Al_2O_3 correlate well with this increased surface area. This can be attributed to the well-known significantly lower thermal stability of ceria[98-99, 109-110], as apparent in the rather drastic drop in surface area for ceria-based carriers between 450°C and 800°C calcination (by a factor of ~3.5-13).

Table 3. Detailed characterization of Fe-, Ni-, and $NiFe_2$-based carriers, synthesized by incipient wetness or deposition precipitation technique, after calcination in air at 450 and 800°C

Calcination temperature (°C)	Carriers	Surface area (m^2/g)	Metal oxide particle size (nm)	Support particle size (nm)	Meal wt.% (EDAX)	Crystalline phases in XRD (oxide)
450	$Fe\text{-}CeO_2$	55.1	17.6	9.7	42.4	Fe_2O_3, CeO_2
	$Fe\text{-}Al_2O_3$	88.5	15.2	6.5	39.9	Fe_2O_3, Al_2O_3
	$Ni\text{-}CeO_2$	55.8	12.7	9.6	40.9	NiO, CeO_2
	$Ni\text{-}Al_2O_3$	51.1	9.7	6.9	40.6	NiO, Al_2O_3
	$NiFe_2\text{-}CeO_2$	94.6	-	8.4	40.7 (Fe/Ni = 1.91)	CeO_2
	$NiFe_2\text{-}Al_2O_3$	152.2	-	6.7	41.9 (Fe/Ni = 2.21)	$Al2O_3$
800	$Fe\text{-}CeO_2$	16.2	23.3	14.8	42.4	Fe_2O_3, CeO_2
	$Fe\text{-}Al_2O_3$	45.7	19.3	6.3	39.9	Fe_2O_3, Al_2O_3
	$Ni\text{-}CeO_2$	4.29	18.5	13.4	40.9	NiO, CeO_2
	$Ni\text{-}Al_2O_3$	40.3	12.4	7.6	40.6	NiO, Al_2O_3
	$NiFe_2\text{-}CeO_2$	14.9	24.4	16.5	40.7 (Fe/Ni = 1.91)	$NiFe_2O_4$, CeO_2
	$NiFe_2\text{-}Al_2O_3$	38.3	15.7	7.7	41.9 (Fe/Ni = 2.21)	$NiFe_2O_4$, Fe_2O_3, Al_2O_3

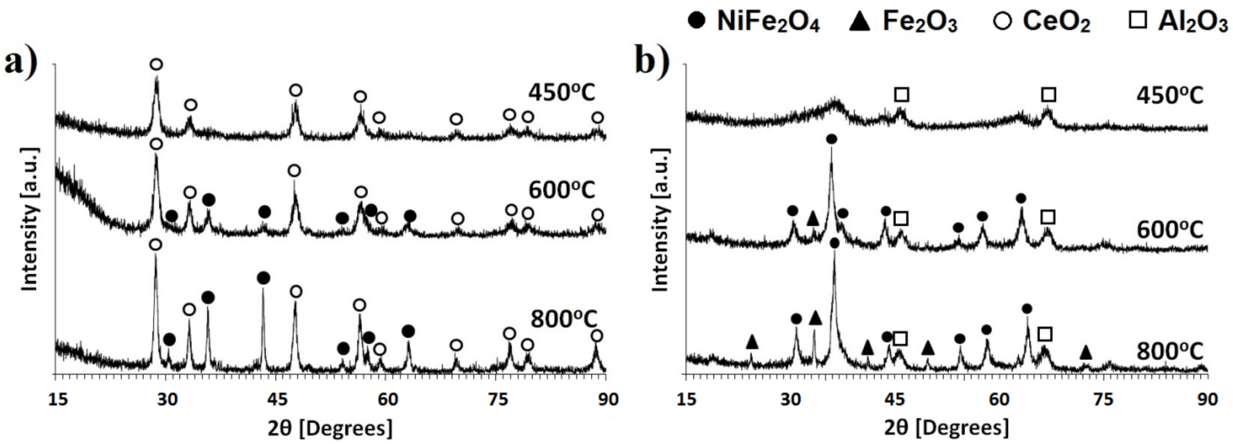

Figure 18. Effect of calcination temperature on a) $NiFe_2$-CeO_2 and b) $NiFe_2$-Al_2O_3 carriers.

All monometallic Ni and Fe carriers were crystalline after calcination at 450°C and XRD only showed the presence of NiO or Fe_2O_3 with their respective support phases. Similarly, for the bimetallic carriers, a crystalline $NiFe_2O_4$ phase is expected in the oxidized carriers according to the phase diagram of Fe/Ni system, which shows a stable Fe-Ni alloy for a Fe/Ni ratio of 2 (i.e. $NiFe_2$ and the respective oxide $NiFe_2O_4$). However, no reflections representing this alloy oxide were detectable in XRD of the bimetallic carriers after calcination at 450°C (Figure 18a, b): The ceria supported bimetallic carrier shows no detectable change in intensity in the vicinity of the expected reflections for $NiFe_2O_4$, while the alumina-supported bimetallic carrier shows a weak, broad peak suggesting the presence of $NiFe_2O_4$ in poorly crystalline state and/or very small size. This is also reflected in the unexpectedly high surface area observed for bimetallic carriers after calcination at 450°C which, unlike for catalysts, is significantly affected by the metal phase due to the rather high weight loadings typical for oxygen carriers (here: 40 wt.%).

Subsequent calcination of the bimetallic carriers at 600°C confirms the presence of $NiFe_2O_4$ for both supports. Further calcination at even higher temperature (T=800°C, the reaction temperature chosen for subsequent CLC tests in the present study), the ceria-based carriers show a stable bimetallic phase with only $NiFe_2O_4$ detectable, while peaks for both monometallic Fe_2O_3 and bimetallic $NiFe_2O_4$ are visible after heat treatment of $NiFe_2$-Al_2O_3 carriers at 800°C.

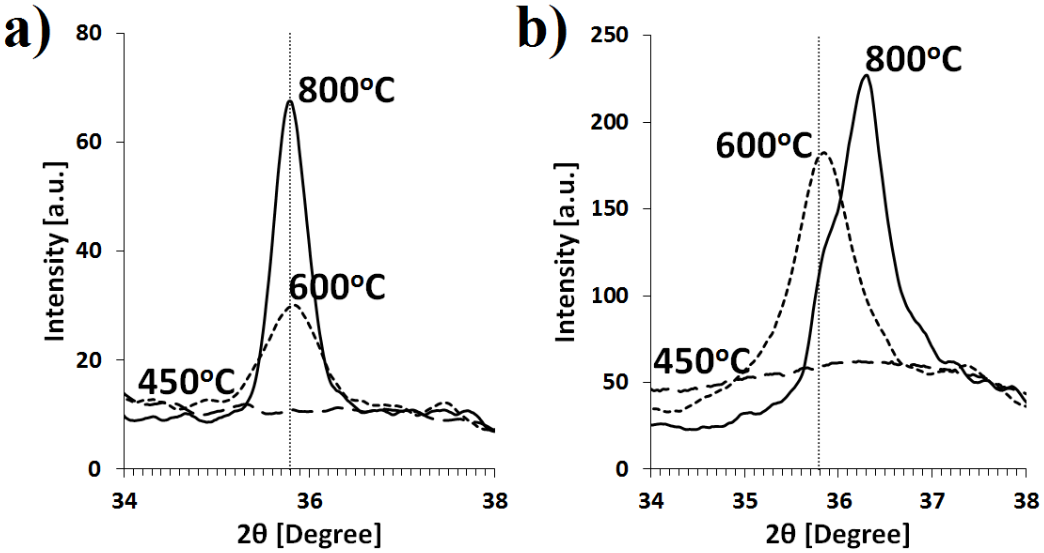

Figure 19. Single XRD peak demonstrating the effect of calcination temperature on phase stability of $NiFe_2O_4$ supported on a) CeO_2 and b) Al_2O_3 as supports (calcined in 0.2 SLM air for 2 h).

The difference in high-temperature stability for $NiFe_2$ supported on ceria vs alumina becomes further apparent in a closer analysis of the diffraction pattern (Figure 19). Unlike for $NiFe_2$-CeO_2 (Figure 19a), the peaks for $NiFe_2O_4$ supported on alumina show a significant shift towards higher 2θ values with increasing calcination temperature (Figure 19b), reflecting a decrease in lattice constant. Table 4 lists the calculated lattice constant for the bimetallic carriers as a function of calcination temperature. For the alumina-supported bimetallics, the lattice constant, which is 0.834 nm for undisturbed $NiFe_2O_4$, decreases from 0.830 nm to 0.821 nm between 600 and 800°C. This decrease can be attributed to the bleeding of Fe^{3+} and simultaneous substitution replacement of Fe^{3+} by (smaller) Al^{3+} as previously reported for Ni-Fe-Al solid solutions[119]. $NiFe_2O_4$ crystallizes in an inverted spinel structure, wherein metal atoms are distributed in two possible sites, A or B. For $NiFe_2O_4$, Ni^{2+} occupies only B sites and Fe^{3+}

occupies both A and B sites in the crystal. With increasing addition of Al in $NiFe_{2-t}Al_tO_4$ crystal, replacement of only Fe^{3+} with Al^{3+} was seen (for $0 < t < 0.9$) by Bara and coworkers, thus resulting in a decrease in lattice parameter[119]. In contrast to that, lattice parameter for $NiFe_2$-CeO_2 remains constant (0.835 nm) and close to the reported literature value for undisturbed $NiFe_2O_4$ (0.834 nm)[120].

Table 4. Lattice parameter of bimetallic $NiFe_2$-based carriers, synthesized by incipient wetness technique, after calcination in air from 450 – 800°C. Typical lattice parameter of $NiFe_2O_4$ = 0.834 nm[120]. $NiFe_2O_4$ is not in crystalline state after calcination at 450°C.

Calcination temperature (°C)	$NiFe_2O_4$ lattice parameter	
	$NiFe_2$-CeO_2	$NiFe_2$-Al_2O_3
450	-	-
600	0.835	0.830
800	0.835	0.821

Thus, while ceria is less thermally stable than alumina, it helps to stabilize $NiFe_2O_4$ but does otherwise not significantly interact with the (bi-)metallic phase, while alumina is—despite its thermal stability—a poor support material as it destabilizes the bimetallic phase through the formation of metal aluminates.

3.2.2 Reactivity tests in TGA

After characterizing the (non-reactive) thermal stability of the carriers, all carrier materials were tested in TGA via periodic exposure to reducing (H_2 or CH_4) and oxidizing (air) gases at 800°C.

The aim of these experiments was to test the carrier stability during exposure to reactive gases and periodic redox conditions. In the first stage of the tests, hydrogen was chosen as model fuel to avoid possible complications due to selectivity issues (partial vs total oxidation of the fuel) and due to (undesired) carbon formation. In the second stage of the evaluation, the carriers were then exposed to cyclic redox using methane as reducing fuel.

3.2.2.1 Reactivity tests with H_2 as fuel

All TGA test were conducted at 800^{o}C with carriers being reduced in H_2 (10 – 35 min) and then oxidized in air (10 min) separated by a nitrogen purge in between the two half cycles. Figure 20 shows ten redox cycles for Fe-CeO_2 during cyclic operation with H_2 and air, respectively, at 800^{o}C. One can see stable periodic operation of the carrier depicted by excellent reproducibility of the alternating patterns of oxidation and reduction half cycles (i.e. weight gain and weight loss of the carrier, respectively) with identical carriers weights in various oxidized or reduced states (within experimental error). Similar tests were also carried out with Fe-Al_2O_3, $NiFe_2$-CeO_2 and $NiFe_2$-Al_2O_3 carriers (not shown here).

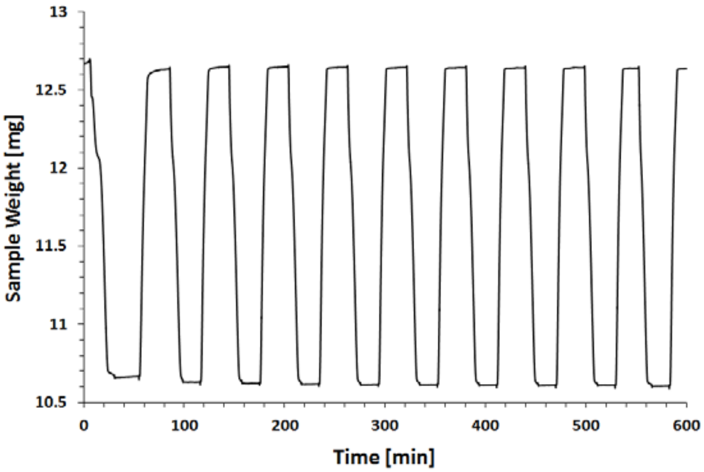

Figure 20. Multiple redox cycles for CLC operation of Fe-CeO_2 in TGA at 800^{o}C with reduction in H_2, N_2 purge, and air oxidation (20 sccm).

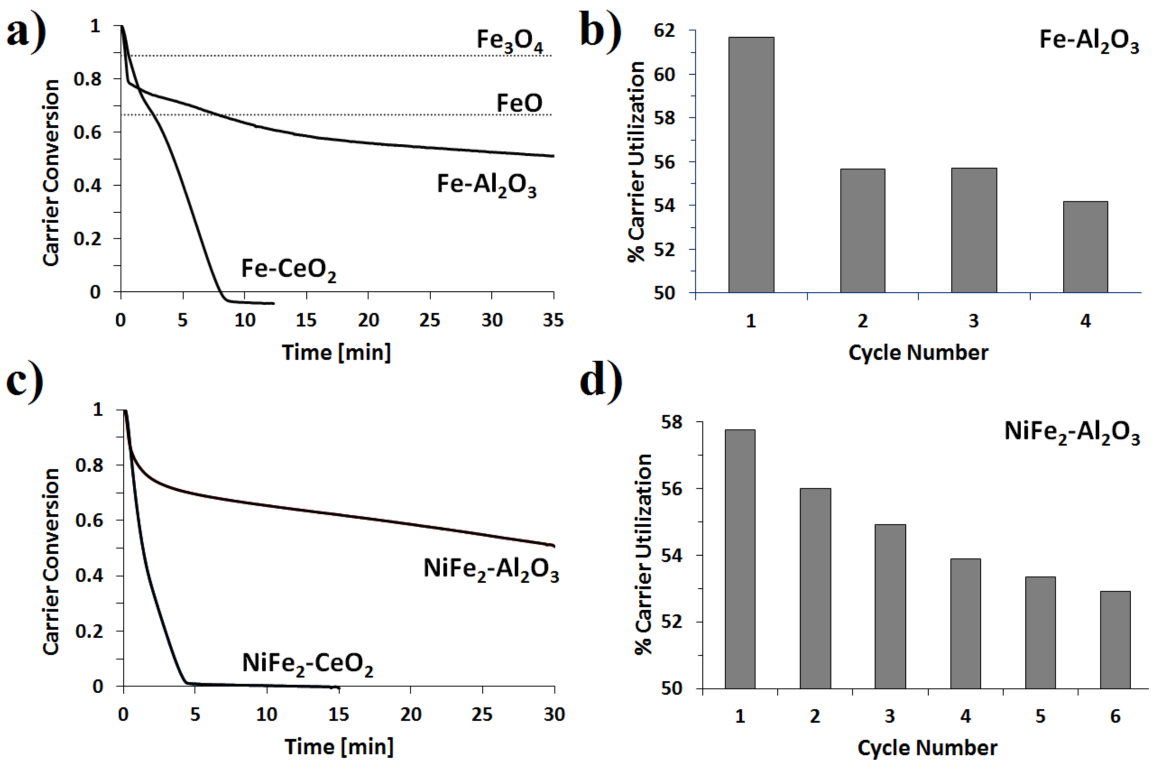

Figure 21. Comparison of carrier conversion for a) Fe-based and c) bimetallic $NiFe_2$-based carriers during the reduction half cycle with H_2 as fuel (20 sccm) in TGA at 800°C. The right-hand graphs b) and d) show the carrier utilization of b) $Fe\text{-}Al_2O_3$ and d) $NiFe_2\text{-}Al_2O_3$, respectively, as a function of cycle number.

Figure 21a shows carrier conversion vs time in a direct comparison between monometallic $Fe\text{-}CeO_2$ and $Fe\text{-}Al_2O_3$ during the last reduction half cycle of their multi-cycle CLC operation with hydrogen. Carrier conversion (X) is defined as: $X = (W - W_{red})/(W_{ox} - W_{red})$. Where W_{ox} is the carrier weight in the fully oxidized state and W_{red} the carrier weight in the fully reduced state, calculated based on the oxygen capacity of the active metal alone (i.e. neglecting any contributions from the support). Thus, $X = 1$ represents the fully oxidized carrier, and $X = 0$ the carrier with a fully reduced metal phase. Further decrease in carrier weight due to support contributions towards the oxygen carrying capacity (which are only possible for reducible supports, i.e. here: ceria) would result in $X < 0$. The dotted lines represent the expected carrier conversion corresponding to the various oxidation states of iron calculated based on the metal loading. One can readily observe that Fe-CeO_2 not only shows complete reduction of the Fe phase with fast redox kinetics, but also shows a marginal, but detectable, contribution due to reduction of ceria (resulting in $X < 0$). This “excess loss” in the carrier weight beyond the expected amount based on the Fe metal loading can be further quantified in terms of the reducibility of support, δ, defined according to the reaction: $CeO_2 + \delta H_2 = CeO_{2-\delta} + \delta H_2O$. The average reducibility ‘δ’ for CeO_2 in Fe-CeO_2 in the present tests is calculated to be 0.112.

In contrast to the ceria-supported carrier, Fe-Al_2O_3 displays fast reduction only in the very beginning of the half cycle (~ first minute) but slows down drastically at ~80% carrier conversion with very slow kinetics for any subsequent decrease in weight. Overall, this carrier barely reaches 50% conversion over the 35 min. duration of this run.

This is further illustrated in Figure 21b, where the carrier utilization is shown for the first 4 redox cycles for the alumina supported carrier: Fe-Al_2O_3 shows ~62% carrier utilization in first reduction half cycle which drops to ~54% by end of the fourth cycle, demonstrating that Fe-Al_2O_3 not only shows poor reduction kinetics, but, more importantly, shows clear signs of progressive deactivation. The carrier utilization for Fe-CeO_2 carriers (not shown), on the other hand, remains stable at nominal values of >100% over the entire 10 cycles (see Figure 20).

Similarly, the bimetallic carriers were evaluated in TGA with regard to thermal stability and reactivity at identical operating conditions, with similar results to the above: Figure 21c shows the comparison of carrier conversion profiles as a function of time during their last reduction half cycle of periodic TGA operation. Once again it can be observed that bimetallic carriers supported on ceria show fast redox kinetics with complete carrier conversion within 5 min into the reduction half cycle, whereas $NiFe_2$-Al_2O_3 carriers show much slower kinetics and hence incomplete carrier conversion even after 30 min of reduction in H_2. The contribution of oxygen carrying capacity from ceria (for $NiFe_2$-CeO_2 carriers) appears to be lower than for the monometallic Fe carriers, but due to the small contributions we cannot exclude that the difference might be due to experimental inaccuracies in the determination of the metal weight loadings. More importantly, however, ceria supports result—beyond complete metal utilization and fast kinetics—again in stable operation (not shown), while alumina-based carriers again are characterized by low utilization and continuous decay in carrier utilization from ~58 to ~53% over six cycles (Figure 21d).

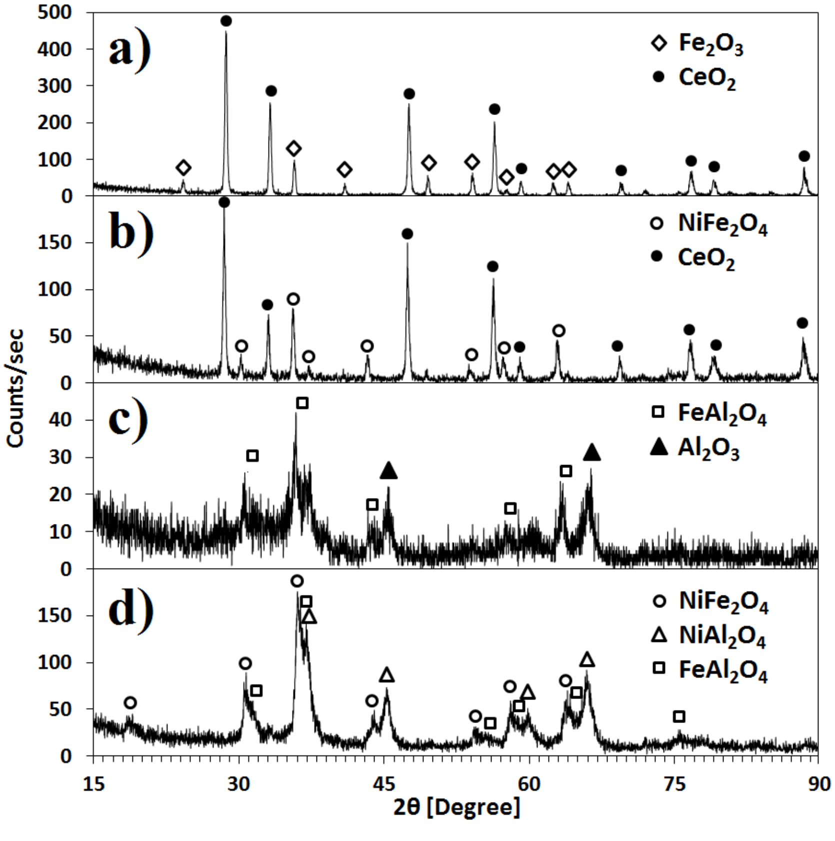

Figure 22. Typical XRD patterns of oxidized a) Fe-CeO_2, b) $NiFe_2$-CeO_2, c) Fe-Al_2O_3 and d) $NiFe_2$-Al_2O_3 carriers after CLC operation in TGA at 800°C (with H_2 as model fuel).

After CLC tests these carriers were withdrawn from TGA in their oxidized state and were further characterized by XRD to investigate the reason behind the low reactivity and deactivation of alumina-based carriers and to verify the phase stability of the $NiFe_2O_4$ phase after exposure to multiple redox cycles at 800°C. Figure 22 shows the XRD patterns for all four carriers (i.e. mono- and bimetallic ceria and alumina carriers). The XRD pattern for the Fe-CeO_2 carrier (Figure 22a) confirms the presence of only Fe_2O_3 and CeO_2, i.e. stable phases, with an increase in the Fe_2O_3 crystallite size from 17.6 nm (after calcination at 450°C) to 21.3 nm post CLC reactive tests at 800°C. Similarly, the bimetallic ceria carriers show only the presence of $NiFe_2O_4$ and CeO_2 phases (Figure 22b), again confirming the excellent phase stability of the bimetallic phase on the ceria support even after exposure to the harsh redox environment of CLC, while the $NiFe_2O_4$ crystallite size after TGA tests (25.3 nm) does not show any significant difference from particle size determined after calcination at 800°C (24.4 nm).

In contrast to that, the XRD patterns for the alumina-based carriers confirm the suspicion—based on the thermal stability tests discussed above (section 3.2.1)—that the formation of Fe-aluminate for the monometallic carrier (Figure 22c) and the de-alloying and formation of both Fe- and Ni-aluminate for $NiFe_2$-Al_2O_3 carriers (Figure 22d) are responsible for the low carrier utilization and slow deactivation of these carriers, as the formation of Fe and Ni-aluminates traps the active metals in a high-temperature stable spinel and thus renders it unavailable for redox kinetics. Assignment of peaks for these carriers was challenging and determination of crystallite size not possible due to poorly defined peaks and complex and overlapping x-ray reflections due to the similarity of the different spinel structures.

Overall, these tests hence show that ceria-supported carriers have faster redox kinetics, better stability, and higher carrier utilization than alumina-supported ones. As a next step, the dependence of these results on the nature of the fuel was tested by transitioning to methane as a (more realistic) fuel with the aim to identify potential differences in redox performance and/or stability due to the more complex nature of this fuel, before finally testing the carriers in fixed-bed studies.

3.2.2.2 Reactivity Tests with CH_4 as fuel

The objective of this set of TGA experiments was to test the carriers with methane as fuel (representing the main constituent of natural gas) while avoiding carbon formation on the reduced metals (which would not only result in undesirable carbon carry-over in a realistic CLC process, but would also complicate evaluation of the TGA experiments due to the concomitant weight increase during reduction due to carbon deposition on the carrier). Thus initial test cycles were conducted to determine the longest reduction time that can be used for the different carriers without coking the carriers. This criterion hence resulted in carrier-specific periods for the reduction half cycles in these tests: ~20 min. for Fe-Al_2O_3, ~18 min. for Fe-CeO_2, ~11 min. for $NiFe_2$-CeO_2, and ~7 min. for $NiFe_2$-Al_2O_3).

Overall, the results with CH_4 as fuel indeed closely match the results observed with H_2: During periodic TGA redox cycles at 800°C with CH_4 as fuel both ceria carriers, Fe-CeO_2 and $NiFe_2$-CeO_2, show stable operation and complete carrier utilization over 10 cycles, while the alumina-supported carriers show very slow kinetics and incomplete carrier utilization. Figure 23 summarizes these results again in analogy to the results with H_2 as fuel (see Figure 21). Figure 23a and c compare the performance of Fe- and $NiFe_2$-based carriers, respectively, for alumina and ceria supports during a single reduction half cycle. While the reduction kinetics with CH_4 is for all carriers significantly slower than that observed in the H_2 tests, the results show the same general trends, with comparatively fast kinetics and full carrier utilization for ceria supports and much slower and incomplete conversion for alumina supports. Similarly, Figure 23b and d show again the low carrier utilization and, for $NiFe_2$-Al_2O_3, the rapid deactivation over just a few cycles. Interestingly, for both carriers, the utilization is significantly lower than in the H_2 tests, suggesting that methane promotes the formation of aluminates. Post-reactive XRD characterization (not shown here) confirms the formation of aluminates again as the reason for the rapid deactivation, while again only Fe_2O_3 and $NiFe_2O_4$ phases were detectable (along-with CeO_2) for Fe-CeO_2 and Fe_2Ni-CeO_2, respectively. Furthermore, Fe-CeO_2 showed only relatively little growth in Fe_2O_3 crystallite size from 17.6 to 24.8 nm, while there is no noticeable difference in $NiFe_2O_4$ crystallite size before (24.4 nm) and after (25.4 nm) CLC tests, as observed before in the tests with H_2 as fuel for $NiFe_2$-CeO_2 carriers.

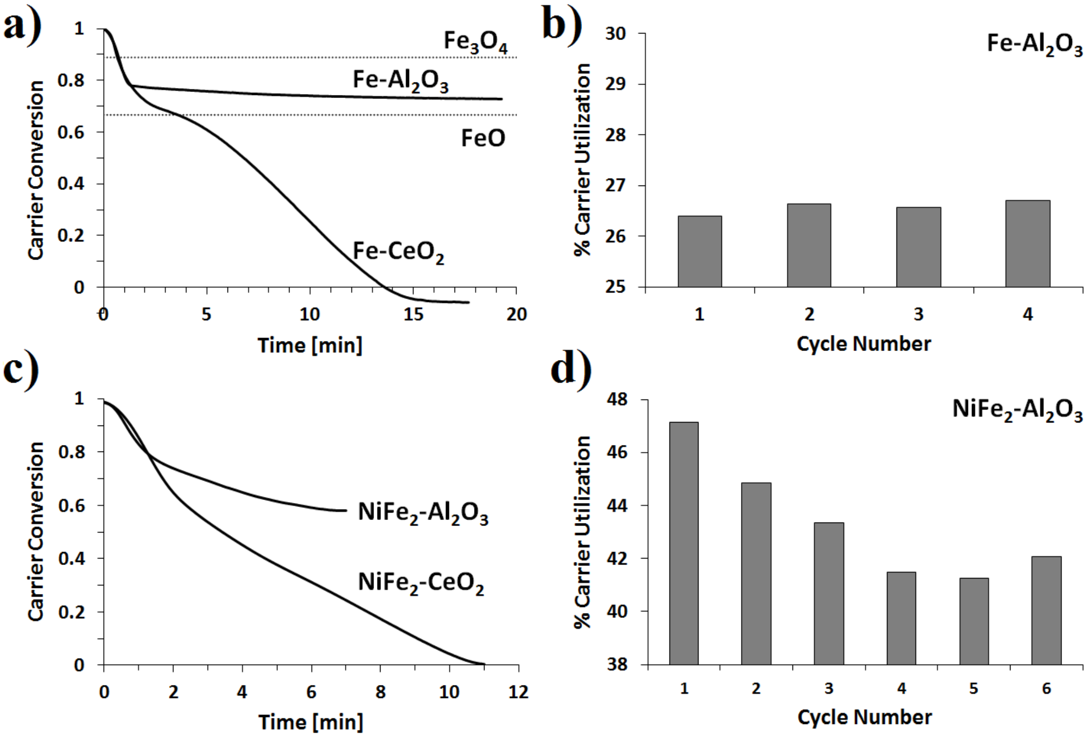

Figure 23. Comparison of carrier conversion for a) Fe-based and c) bimetallic $NiFe_2$-based carriers during reduction half cycle with CH_4 as fuel (5 sccm) during CLC operation in TGA at 800°C. The right-hand graphs b) and d) show the carrier utilization of Fe-Al_2O_3 and $NiFe_2$-Al_2O_3, respectively, as a function of cycle number.

Overall, the use of reducible supports, such as ceria, results in a strong enhancement of the reactivity of the supported metal, i.e. in a synergistic effect, allowing complete carrier utilization with fast redox kinetics as also observed in our previous work (chapter 2.0) with nickel-based carriers[42]. Significantly, however, the use of ceria also endows the bimetallic carrier with much better thermal stability of the nickel ferrite phase, while alumina supports result in rapid de-alloying due to the formation of aluminates.

3.2.2.3 Effect of metal phase on carrier reactivity

While our discussion so far has mostly focused on the impact of the support nature on the reactivity and stability of the carrier, it makes sense at this point to briefly review the results again from the perspective of the metal phase. The objective of the present work was not only to investigate the effect of reducible vs. non-reducible supports for iron and bimetallic carriers, but also to examine how far bimetallic carriers can result in improvement of redox performance of iron based carriers. As mentioned previously, various studies have shown that nickel is a very active metal in CLC and results in fast redox kinetics[29, 33, 47, 66], but suffers from high cost and toxicity. In contrast, iron is economically attractive and environmentally benign, but lacks the high redox activity[21, 33, 47, 66, 118, 121], as also evident in our current work. It is thus temping to evaluate the potential of bimetallic FeNi carriers to get the best of both worlds, i.e. to take advantage of high reactivity of nickel and low cost of iron by alloying Fe and Ni.

Figure 24 shows a direct comparison of Ni-, Fe-, and $NiFe_2$-CeO_2 carriers during reduction half cycle with H_2 (Figure 24a) and CH_4 as fuel (Figure 24b). One can clearly see that—while all three carriers achieve 100% utilization with both fuels—the introduction of highly reactive Ni into Fe-based carriers significantly accelerates the reduction kinetics. The enhancement is more prominent in case of H_2 as fuel than for CH_4. This is somewhat surprising, given the fact that Ni is a much more efficient catalyst for C-H bond activation than Fe (as also reflected in the fact that the reduction kinetics with the much less reactive methane fuel is almost identical to that with H_2 in our experiments). Therefore, one would anticipate a more pronounced promoting effect of Ni in methane oxidation than H_2 oxidation. At this point, we do not have a consistent explanation for this observation.

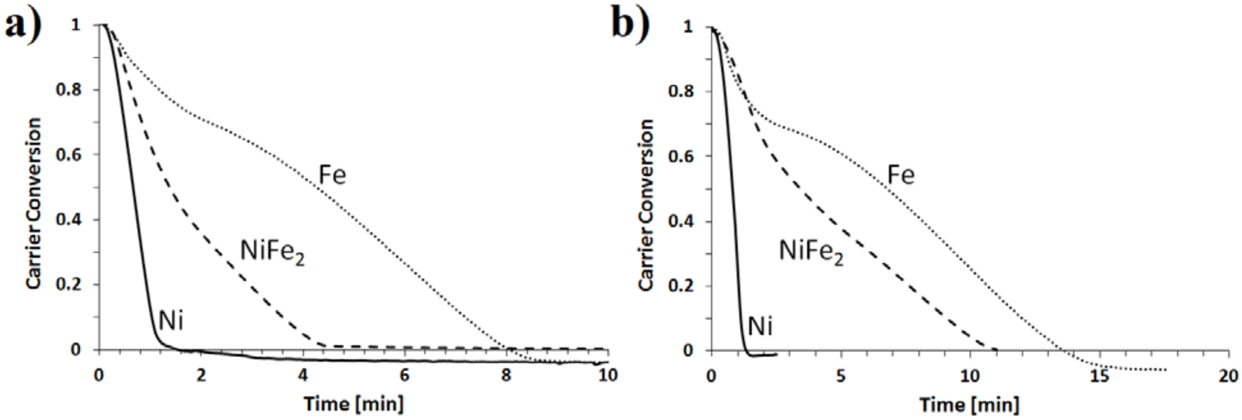

Figure 24. Comparison of ceria based oxygen carriers during reduction with a) H_2 and b) CH_4 in TGA at 800°C.

Generally, during reduction of Fe_2O_3 to Fe, the iron oxide goes through multiple oxidation states $Fe_2O_3 \rightarrow Fe_3O_4 \rightarrow FeO \rightarrow Fe$[122], each with its own crystal structure (Fe_2O_3 (hematite) crystallizes in the corundum structure with a hexagonal close packed array of oxygen, Fe_3O_4 (magnetite) in an inverse spinel, FeO in fcc, and Fe in a bcc structure). Thus, during reduction, the atoms in the crystal structure need to undergo repeated significant rearrangement and hence need to overcome the energy barrier associated with this steric hindrance. In contrast, both NiO and Ni exist in fcc crystal structure, allowing for easy release of oxygen during the reduction. Repeated atomic rearrangement might hence be the cause for the widely observed slow reduction kinetics with Fe-based carriers, and might also explain the clearly visible shoulder in the reduction curves of the Fe carriers at a carrier conversion of ~67% (corresponding to FeO).

Interestingly, Fe and bimetallic carriers show identical reduction curves during the initial phase of reduction with methane, and again virtually identical reduction kinetics (i.e. gradient of the conversion time trace) in later stages (Figure 24b). The main difference hence appears to be the absence of the delay shoulder at the Fe_3O_4-FeO transition point for the bimetallic material. Since both $NiFe_2O_4$ and Fe_3O_4 have the same inverse spinel structure this could tentatively point towards Ni facilitating the rearrangement of the crystal structure.

The conversion traces for H_2 fuel show a similar disappearance of the delay shoulder for Fe upon Ni addition, and again similar rates of carrier conversion between the Fe and $NiFe_2$ carriers for longer times. However, for this fuel, the initial reduction of the bimetallic does not follow the trends observed for Fe (nor those for Ni), but falls in between the two monometallic carriers. This could point to differences in the reaction mechanism for the reduction with the two fuels, but our experiments do not allow for a more detailed differentiation between those.

Overall, by using bimetallic carriers supported on ceria, we attain not only complete conversion with faster reduction kinetics, but are also able to significantly reduce the amount of nickel used in the carriers, thus generally validating the basic motivation for the present study.

3.2.3 Reactive tests in fixed-bed reactor

Although the TGA tests yield important insights into the reactivity and stability of the carrier materials, the flow configuration (and hence the gas-solid contacting pattern) in a TGA is not representative of that in a fixed-bed or fluidized bed reactor, nor does it allow for studies of the selectivity of the gas-solid reaction. Selectivity is an important factor, as CLC aims at (near-)

complete carbon capture via complete combustion of the fuel to CO_2 and steam. Partial oxidation products (such as CO and H_2), and fuel cracking to carbon are undesired. Therefore, as a final step in the present investigation, carriers were investigated in a fixed-bed configuration at conditions otherwise identical to those of the TGA experiments. Due to the clear superiority of the ceria-based carriers in the TGA studies, alumina carriers were excluded from the fixed-bed studies, i.e. the carriers were down-selected to Fe-CeO_2, Ni-CeO_2 and $NiFe_2$-CeO_2.

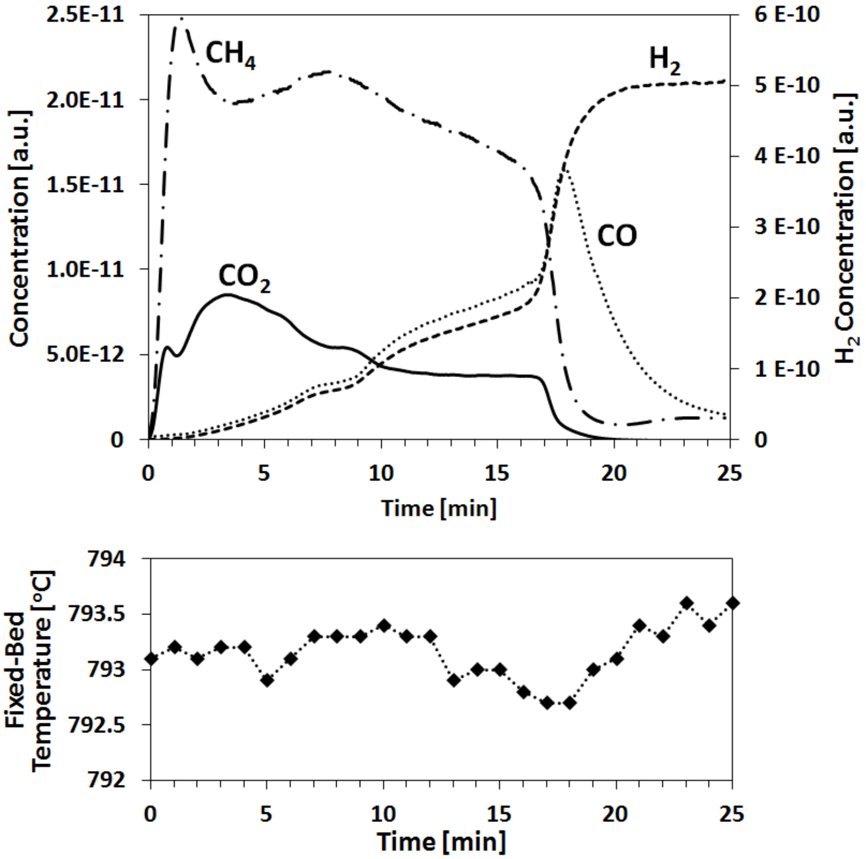

Figure 25. (Top graph) Concentration of various combustion products (after condensation of steam) during reduction half cycle with CH_4 as fuel (1 sccm, 16.7 vol.% in Ar) in fixed-bed reactor operation of $NiFe_2$-CeO_2 (100 mg). Bottom graph: Fixed-bed reactor temperature during reduction half cycle.

Figure 25 (top) shows results for the bimetallic $NiFe_2$-CeO_2 carrier. The concentration traces of various species formed during the combustion of methane in fixed-bed reactor reduction half cycle are shown. The fixed-bed reactor temperature was continuously monitored and remained constant during reduction half cycle at 793^{o}C within +/- 1^{o}C (Figure 25 bottom).

One can distinguish roughly four phases of the methane conversion: An initial period with relatively low activity (i.e. low methane conversion) but high selectivity for total combustion products (as seen in the CO_2 trace; t~0-10 min.). This is followed by a period of mixed selectivity (roughly equal amounts of partial and total oxidation; (t~10-17 min.), before the reaction selectivity switches to a brief period of very selective partial oxidation with near-complete methane conversion (t~17-20 min.), and finally, over an oxygen-starved carrier, to methane cracking as apparent from the disappearance of C-containing products with continued H_2 production (t>20 min.). The reduction half cycle is terminated at t= 25 min for $NiFe_2$-CeO_2 to avoid excess carbon formation on the reduced carrier.

The reactor was then purged in Ar for 30-60 min, and the carrier was then oxidized in 20% O_2 in He (10 min; not shown here). During the oxidation, evolution of CO and CO_2 was observed indicating carbon burn-off. Once the carbon burn-off was complete and the oxygen carrier was re-oxidized, CO and CO_2 concentration dropped off and oxygen break-through was observed – indicating complete regeneration of the carriers.

Fe- and Ni-CeO_2 were similarly tested in the fixed-bed reactor to investigate for their efficacy in methane conversion in reduction half cycle. However, the reduction time were adjusted for all three carriers due to differences in their reactivity towards methane combustion. Characterization of the carriers via XRD after fixed-bed reactor evaluation confirmed again the excellent phase stability of the ceria-supported carriers: In all cases, only reflections for the respective metal oxide and the ceria support, i.e. only NiO, Fe_2O_3, $NiFe_2O_4$ and CeO_2 were detectable.

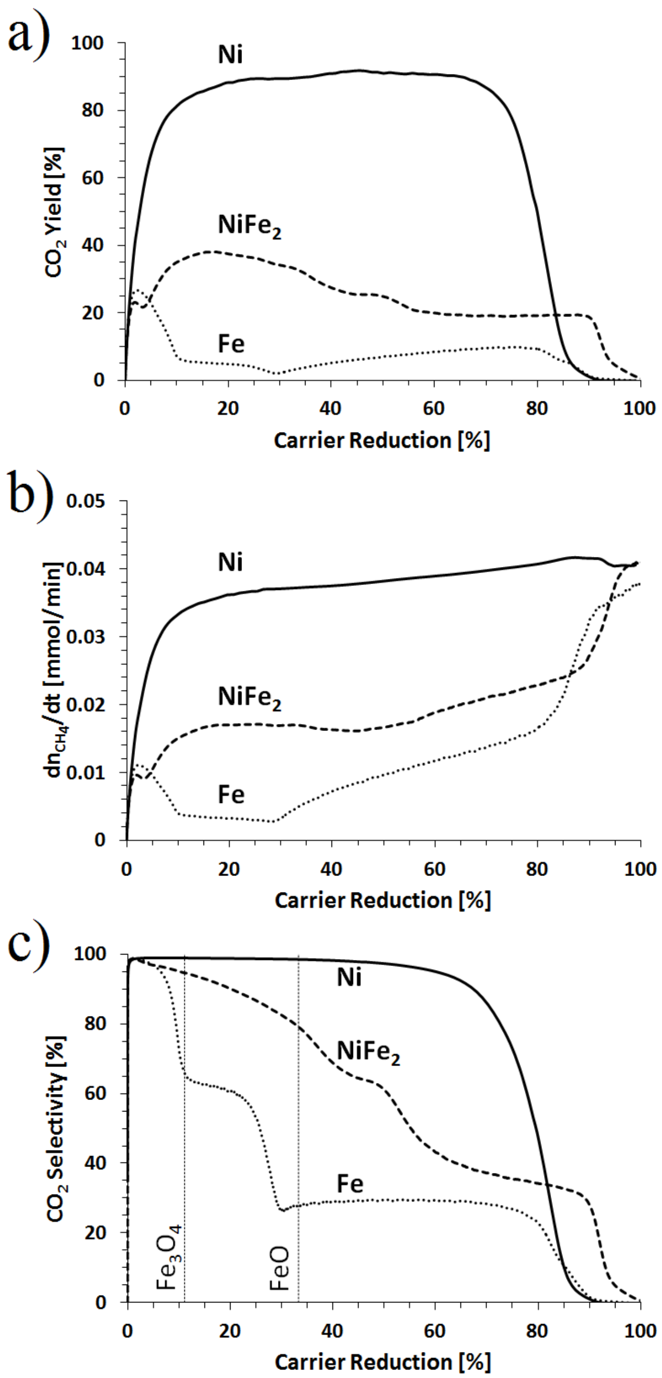

Figure 26. Comparison of a) CO_2 yield, b) rate of methane conversion and c) CO_2 selectivity as a function of carrier reduction for ceria based oxygen carriers (monometallic Ni, Fe and bimetallic $NiFe_2$ during reduction with methane (16.7 vol.%, 1sccm) in a fixed-bed reactor at 800^{o}C.

Figure 26 summarizes and compares the results for all three carriers in the form of CO_2 yield (Figure 26a), rate of methane conversion (Figure 26b), and CO_2 selectivity (Figure 26c) as a function of carrier reduction, where a reduction of zero indicates a completely oxidized carrier and a carrier reduction of 100% the completely reduced carrier. Figure 26a shows that – as expected - Ni shows by far the highest CO_2 yield while Fe shows poor CO_2 yields across the entire range of carrier conversion (i.e. over the entire reduction half-cycle). For the latter, CO_2 yield shows a brief initial maximum and then drops off at ~11% carrier conversion, which roughly translates to the transition from Fe_2O_3 to Fe_3O_4, indicating, as expected, that the highest oxidation state of the carrier shows best selectivity for total oxidation. In contrast to that, Ni shows consistently high CO_2 yields up to very high degree of reduction, i.e. the reaction selectivity is essentially independent on the degree of oxidation of the carrier. Interestingly, the bimetallic carrier shows an increase in CO_2 yield after the initial ~5% carrier reduction, despite the decreasing oxygen content of the carrier.

These differences in carrier reactivity are further reflected in the respective rates of methane conversion (Figure 26b). Ni again shows a very high reaction rate, Fe a very low rate, and the bimetallic $NiFe_2$ carrier shows a strong enhancement of the rate in comparison to monometallic Fe, albeit still only half the rate of the monometallic Ni carrier. Interestingly, all three carriers show strong increases in CH_4 conversion rates towards very high carrier reductions, i.e. convergence of their reactivity for methane cracking in their fully reduced metallic states. This suggests that the difference in the carrier reactivities is not due to different activity for C-H bond scission, but rather due to differences in the ability of the carriers to oxidize the resulting carbonaceous deposits[123-124].

Finally, Figure 26c shows a comparison of CO_2 selectivities vs carrier reduction. Overall, not surprisingly, Ni again shows the highest (near perfect) CO_2 selectivities, and Fe the lowest. Interestingly, CO_2 selectivity over Fe shows four distinct ranges with increasing carrier reduction, separated by surprisingly sharp transitions. The first two of these transitions correspond closely to the points at which a transition to the next lower oxidation state is expected (indicated by the dashed lines in the graph), while the last transition occurs at ~85% reduction, i.e. close to the metallic state of the carrier. Clearly, and not entirely surprisingly, the selectivity of iron oxide decreases with increasing degree of reduction. In its fully oxidized hematite form, Fe-based carriers are hence reasonable carrier materials for CLC, but their very limited range of selective operation between Fe_2O_3 and Fe_3O_4 limits their potential for industrial application. Interestingly, the $NiFe_2$ carrier not only shows significantly enhanced CO_2 selectivity across the entire range of carrier reduction, but also does not show the clear transitions of the monometallic Fe carrier any more but rather shows much weaker shoulders, shifted significantly towards higher degrees of carrier reduction. This agrees with the previously discussed loss of the shoulder in the TGA experiments and suggests again that Ni strongly affects the phase transitions between the different iron oxides. This shifts extends the realistic operational range for the $NiFe_2$ carrier significantly (for example, for a limit of >80% selectivity, it shifts from <10% carrier reduction for Fe to >30% carrier reduction for $NiFe_2$), rendering this carrier of potential practical interest, despite its lower activity and hence reduced CO_2 yields in comparison to Ni carrier.

3.3 SUMMARY

In the present study, mono- and bimetallic Ni/Fe carrier materials were synthesized via a cheap, scalable synthesis technique, using both a non-reducible (alumina) and a reducible (ceria) support material. The ceria supported materials show strongly improved phase stability in comparison to alumina supported ones. In particular, the bimetallic alumina-supported carrier showed significant de-alloying and formation of metal aluminates limiting their carrier utilization. On the contrary, the use of the reducible support results in much faster redox kinetics and complete carrier utilization.

The reactivity of these carriers in TGA and fixed-reactor studies declines in the order Ni > $NiFe_2$ > Fe, with reaction rates as well as selectivity following the same ranking. Interestingly, while Fe-based carriers show distinct, well-defined features reflecting the transition between the different oxidation states of Fe, these features are absent or much weakened for the bimetallic carrier, suggesting that Ni facilitates the transition between the different crystallographic structures associated with the different oxidation states for Fe.

Overall, our results confirm that alloying a less reactive metal, such as Fe, with a more reactive one, such as Ni, can indeed significantly improve the activity of the resulting bimetallic carrier for CLC. In the present case, this allows reduction of the cost and environmental concerns associated with the use of Ni as demonstrated in recent toxicity studies with FeNi oxide[125]. Although such bimetallic carriers constitute a significant improvement over monometallic Fe-based carriers, their performance stills fall short of that of highly reactive Ni-based carriers. Nevertheless, the presented results show that by systematic engineering of the metal phase in engineered oxygen carriers, the activity and stability of these carriers can be strongly improved, resulting in carrier materials with a good balance between cost, toxicity, and reactivity.

4.0 IRON MANGANESE MIXED-OXIDE OXYGEN CARRIERS FOR CHEMICAL LOOPING COMBUSTION

Among the various metals tested for CLC, iron has emerged as an attractive candidate due to the low toxicity, low cost and abundance. However, as illustrated in chapter 3.0, the use of iron as an oxygen carrier metal is hampered due to the poor reactivity with fuel and limited oxygen transfer capacity ($Fe_2O_3 \Leftrightarrow Fe_3O_4$) towards CLC which would necessitate high solid inventory. Apart from iron, manganese also presents the opportunity of using benign and low cost metal as oxygen carrier. Moreover, like iron, it also exhibits multiple oxidation states that could be potentially utilized for total oxidation of fuel. In spite of that, there are only a few studies investigating use of Mn-based oxygen carriers due to their low reactivity and tendency to react with support oxides to form stable spinels[33, 37, 45].

Work from previous chapter shows that combining less reactive iron with highly active nickel, in the form of nickel ferrite, can improve the carrier reactivity[39]. Thus, in this report we intend to investigate the effect of combining iron with manganese – a relatively non-toxic and cheaper alternative to nickel. In fact, the system of unsupported Fe-Mn has been used before with in-situ X-ray capabilities to understand phase evolution during reduction and re-oxidation of these carriers. The study showed that metals phase segregate during reduction[126]. However, the Fe-Mn system has been predominantly explored in context of chemical looping oxygen uncoupling (CLOU), as it is promising for gas phase oxygen release due to its favorable thermodynamics[127], which has been confirmed experimentally[128-129].

Hence, in the present study, we focus the study on investigating Fe-Mn system specifically for CLC application. We intend to alloy iron and manganese with various Fe/Mn ratios with the aim to understand the effect of Fe-Mn composition on CLC activity and stability. Based on our previous work (chapter 2.0 , 3.0)[39, 42], which underscores the advantage of using reducible oxides as active supports to strongly increase the oxygen carrying capacity of supported metal, we stabilize the Fe-Mn phase onto a CeO_2 matrix. Compared to conventional supports like alumina, ceria allows good phase stability of supported bimetallic nickel ferrite, and thus we intend to investigate phase stability of Fe-Mn alloy on ceria. In this study, carriers are synthesized by incipient wetness technique and are subsequently characterized to detect the formation of bimetallic phases. With understanding of various mono- or bimetallic phases present in the samples, the Mn_xFe_{1-x}-CeO_2 carriers are subjected to CLC tests using H_2 and CH_4 as fuels in a thermogravimetric analyzer (TGA) and then further investigated in fixed-bed reactor CLC tests. Our results show that, depending on the Fe/Mn ratio, different types of mixed oxide phases can be obtained that show different reactivity in the CLC tests. The effectiveness of combining iron and manganese can be hampered in some cases due to the large-scale de-alloying and re-alloying of the carriers during redox operation. We observe that, compared to monometallic iron- or manganese-based carriers, manganese doped with iron can indeed significantly improve carrier reactivity and fuel conversion. Moreover, unlike various supports, ceria facilitates good stability of supported manganese oxides and mixed metal oxides of iron and manganese.

4.1 EXPERIMENTAL

4.1.1 Carrier synthesis and characterization

Synthesis of oxygen carriers using low-cost and scalable techniques is critical in limiting the cost of oxygen carrier manufacturing. Thus, in this study oxygen carriers were synthesized in a simple and scalable two-step procedure. First the ceria support was synthesized, and Fe and Mn were deposited by incipient wetness technique.

Ceria was synthesized according to the procedure previously explained in section 2.1.1. Monometallic Mn and mixed-oxides of Fe-Mn carriers with 40 wt.% metal were synthesized via incipient wetness described before (section 2.1.1). Obtained carriers were calcined at temperatures at 800^{o}C and/or 900^{o}C.

The carriers were thoroughly characterized at different stages of the experiments, i.e. after synthesis, after reactive tests in TGA, and after fixed-bed reactor tests. The specific surface area was determined via nitrogen sorption in a Micromeritics ASAP 2020 gas adsorption analyzer using the BET method. Prior to the measurement, the samples were degassed for 2 h at 200^{o}C under high vacuum. After calcination at 900^{o}C for 2 h, all the carriers were found to have surface area <5 m^2/g. Unlike conventional alumina-based oxygen carriers, the low surface area upon sintering the carriers can be explained by the relatively low thermal stability of ceria as support[98-99, 109-110]. X-ray diffraction (XRD) measurements were performed with a powder X-ray diffractometer (Phillips PW1830) in line focus mode employing Cu Kα radiation (λ = 1.5418 Å) with typical 2θ scans between 15^o and 90^o. Crystal phases were identified based on JCPDS cards. Average crystal lattice spacings were determined using Bragg's law. The JEOL JEM-2100F high-resolution transmission electron microscope (HR-TEM) was used to conduct electron energy-loss spectroscopy (EELS) to be able to determine local spatial elemental composition in the sample.

4.1.2 Reactive tests

Initially pure H_2 was used as a model fuel to characterize carrier performance during redox cycles without the added complexity of carbon formation that is associated with use of methane as fuel. Kinetics and thermal stability of the carriers with H_2 as fuel were evaluated in thermogravimetric analyzer tests (Perkin Elmer TGA-7). Subsequently, CLC redox cycles were conducted (TA instruments, SDTQ600) with CH_4 as fuel to test for carrier selectivity and thermal stability with a particular focus on carbon formation on the carrier material that would result in undesired carbon carry-over from the reducer to the oxidizer. All experimental conditions were identical to as explained in section 2.1.2.

As a last step, fixed bed experiments were conducted to investigate the effectiveness of carriers for CH_4 conversion to H_2O and CO_2 – crucial for efficient CO_2 capture in CLC. Wherein, operating conditions and experimental set-up for fixed-bed tests were kept identical to studies investigating Ni_xFe_{1-x}-CeO_2 carriers (chapter 2.0, 3.0).

4.2 RESULTS AND DISCUSSION

4.2.1 Formation of bimetallic phases and their stability

Understanding the catalyst morphology and structural properties is important to confidently establish the structure-activity relationships. In context of Chemical Looping Oxygen Uncoupling (CLOU), the combined metal oxides of iron and manganese were shown to have strong dependence on the Fe/Mn ratio for their ability to release oxygen. However, powder XRD results were inconclusive to determine the exact composition of monometallic and bimetallic phase[128, 130]. Along the same lines, this study aims at investigating the effect of the Fe/Mn ratio upon carrier performance in CLC redox cycles. As a result, oxygen carriers were carefully characterized to understand their material properties and to investigate for formation of bimetallic Fe-Mn phases that could potentially impact the carrier reactivity in CLC redox cycles.

In the present study, we have synthesized Mn_xFe_{1-x}-CeO_2 carriers, with x = 0, 0.1, 0.33, 0.5, 0.8, 0.9, and 1. The various concentrations of iron and manganese were chosen to investigate the effectiveness of bimetallic Fe-Mn and doped-Mn or Fe phases for their reactivity with total oxidation of methane. The possibility of forming different mixed oxide phases due to variations in the Fe/Mn ratio could be understood by studying the Fe-Mn phase equilibria in air. The Fe-Mn system in air is well understood, and Fe_2O_3 and Mn_2O_3 are known to show mutual solubility up to temperatures of approximately 1000^oC[127]. The Fe-Mn system in air is observed to show a spinel solid solution (Fe_3O_4-Mn_3O_4) with comparable amounts of Fe and Mn, a hematite solid solution with large excess of iron (Fe_2O_3 with some manganese oxide dissolved in it), and Mn_2O_3 or Mn_3O_4 solid solutions (depending on temperature) in manganese rich cases (α-Mn_2O_3 or Mn_3O_4 with some iron oxide dissolved in the structure)[127]. Thus, the literature data confirms that iron and manganese show affinity towards each other that can result in formation of various bimetallic phases, depending on their relative concentrations.

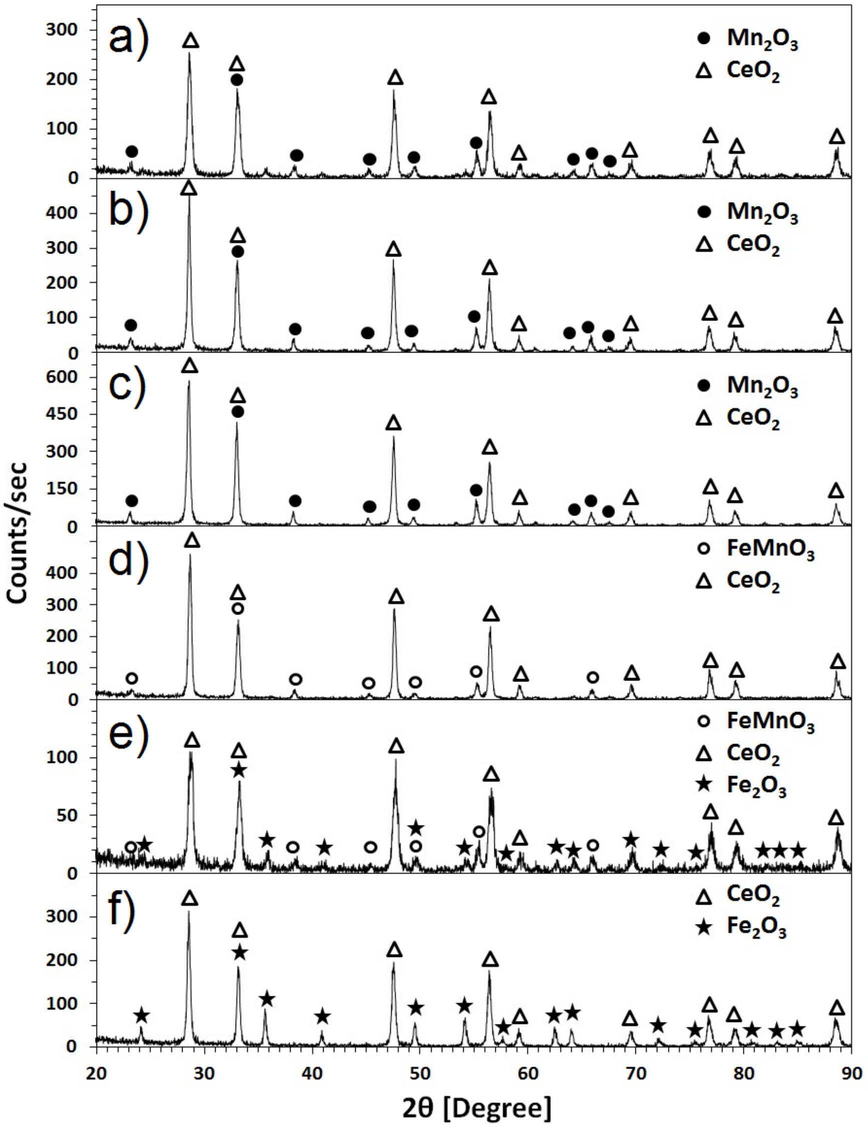

Figure 27. Typical X-ray diffraction pattern of Mn_xFe_{1-x}-CeO_2 carriers after calcination at 900°C for 2 h (0.2 SLM air) where a) x = 1, b) x = 0.9, c) x = 0.8, d) x = 0.5, e) x = 0.33 and f) x = 0.1.

Figure 27 shows the x-ray diffraction pattern of Mn_xFe_{1-x}-CeO_2 oxygen carriers subjected to calcination in air at 900°C for 2 h. In the case of Mn-CeO_2 (Figure 27a), it can be seen that peaks corresponding to only Mn_2O_3 and CeO_2 are detected and no signs of spinel formation between manganese oxide and ceria are observed. It is well known that manganese shows high tendency to react with the support oxides forming spinel structures that are inactive in redox cycles[33]. Absence of such spinels with use of ceria as support confirms the excellent stability of manganese on ceria. Upon doping some iron into manganese oxide (Figure 27b, c), no separate peaks of Fe_2O_3 are observed, indicating that iron is dissolved into the Mn_2O_3 structure. A bimetallic bixbyite phase ($FeMnO_3$) is observed with stoichiometric amounts of Fe and Mn (Figure 27d). Over-stoichiometric amounts of iron compared to manganese in the carrier shows a mixture of bixbyite and residual-free Fe_2O_3 phase (Figure 27e). Such behavior has been observed before with ball milled samples[131]. On the other hand, doping Mn into iron oxide shows only Fe_2O_3 peaks (Figure 27f), which suggests that manganese is dissolved into hematite.

Information of nominal weight loadings of iron and manganese coupled with detection of the Fe_2O_3 phase allows for logical peak assignment in XRD analysis. However, determination of relative quantities of $FeMnO_3$ (JCPDS PDF #: 76-0076) and Mn_2O_3 (JCPDS PDF #: 78-0390) is not possible, as both the aforementioned oxides show peaks at same position with almost identical relative peak intensities. Below about 300K, α-Mn_2O_3 transforms from a cubic to an orthorhombic crystal structure[132-133], while $FeMnO_3$ exhibits cubic bixbyite phase[134]. Despite exhibiting different crystal structures around room temperature, distinguishing between Mn_2O_3 and $FeMnO_3$ by means of lattice parameters is not possible, as they exhibit near identical values[133-134]. However, verifying formation of the bimetallic phase is important to understand their reactivity in redox cycles.

$Mn_{0.5}Fe_{0.5}$-$CeO_{2,}$ containing stoichiometric amounts of iron and manganese, was chosen for further tests to confirm the formation of the bimetallic $FeMnO_3$ phase. Specifically, $Mn_{0.5}Fe_{0.5}$-CeO_2 was chosen due to the ease of analysis, as complete incorporation of iron into stoichiometric amount of manganese would only form $FeMnO_3$ and would not result in separate Fe_2O_3 peaks in x-ray pattern. Calcination temperature variation was chosen as a test parameter: Powders obtained from the synthesis of samples were first calcined at 800°C for x-ray analysis, and subsequently the oxygen carriers were calcined at the CLC operation temperature of 900°C.

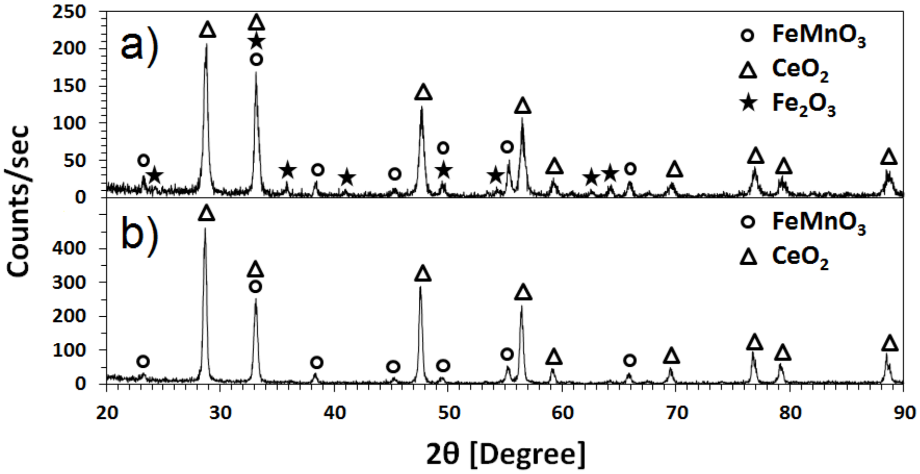

Figure 28. X-ray diffraction pattern demonstrating the effect of calcination temperature a) 800°C and b) 900°C on $Mn_{0.5}Fe_{0.5}$-CeO_2 (calcined in 0.2 SLM air for 2 h). Calcination of carriers at 900°C leads to loss of free Fe_2O_3 phase confirming formation of bimetallic $FeMnO_3$ phase.

Figure 28 shows the XRD pattern of $Mn_{0.5}Fe_{0.5}$-CeO_2 calcined at a) 800°C and b) 900°C. It can be seen that the carrier calcined at 800°C clearly displays the presence of free Fe_2O_3 phase in the sample, whereas the peaks corresponding to Fe_2O_3 disappear upon calcination of sample at 900°C. Thus, absence of any peaks strongly suggest that all the iron oxide is incorporated into the cubic bixbyite structure of $FeMnO_3$, and if there is any residual free iron oxide present in the sample, it is under the detection limit of the XRD analysis.

Furthermore, TEM equipped with electron energy loss spectroscopy (EELS) was used to understand the special distribution of various metals at nanometer scale. Figure 29 illustrates a typical TEM and elemental maps of individual elements (i.e. Mn, Fe and Ce) in the $Mn_{0.5}Fe_{0.5}$-

CeO_2 sample. From the figure, it can be observed that iron and manganese are well dispersed in the sample, and they are found in close vicinity of each other. During the EELS analysis, no separate islands of free iron devoid of manganese were found. Thus EELS analysis provides an indirect evidence of formation of $FeMnO_3$ in the $Mn_{0.5}Fe_{0.5}$-CeO_2 sample.

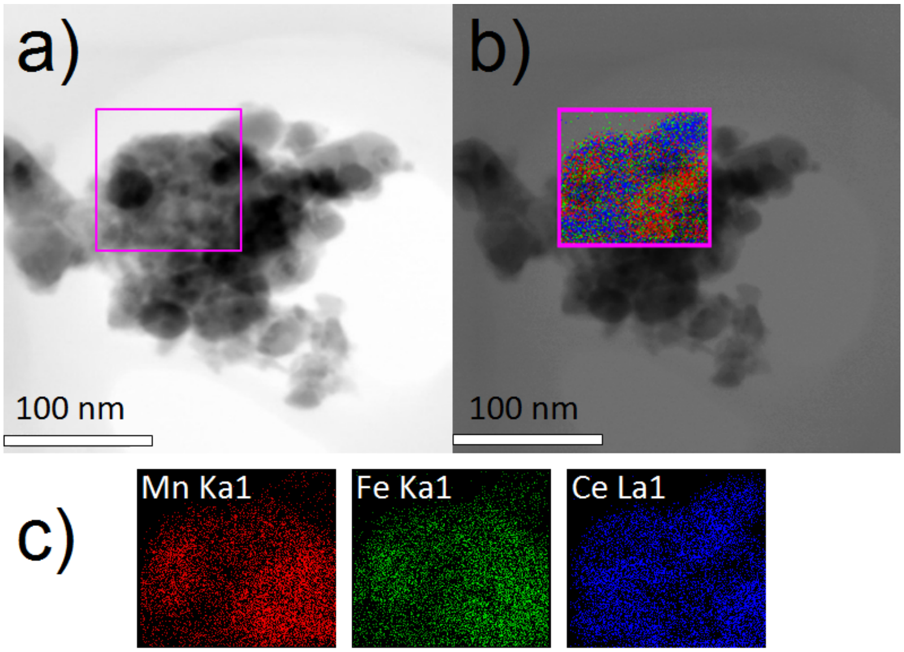

Figure 29. a) TEM; b) TEM with superimposed elemental maps and c) elemental distribution of individual elements Mn (left), Fe (middle) and Ce (right) in $Mn_{0.5}Fe_{0.5}$-CeO_2 carrier (calcined at 900°C in 0.2 SLM air for 2 h). EELS analysis confirms occurrence of Fe and Mn in close vicinity at nanometer scale.

Additionally, Rietveld refinement as an auxiliary test was performed using the commercially available software PANalytical X'Pert Highscore Plus to determine quantitative phase composition of $Mn_{0.5}Fe_{0.5}$-CeO_2. The required high resolution data was obtained by powder diffraction measurements using Brukers D8 Discover, equipped with LynxEye Detector. Rietveld analysis resulted in good fitting and $Mn_{0.5}Fe_{0.5}$-CeO_2 was found to contain 42.6% $FeMnO_3$, 0.2% Mn_2O_3, 0.4% Fe_2O_3 and 56.8% CeO_2. Here, the metal weight loading is in close agreement with the nominal weight loading of the carriers (40 wt.%). Thus Rietveld analysis also re-confirms that $FeMnO_3$ is the major phase containing iron and manganese (with minimal amounts of free Mn_2O_3 and Fe_2O_3). Thus, having understood the material properties of the oxygen carriers, we next subject them to CLC redox cycles to investigate any possible advantage of alloying iron with manganese.

4.2.2 Reactivity tests in TGA

After understanding the material properties of the carriers, all the carriers were tested in TGA via periodically exposing them to reducing (H_2 or CH_4) and oxidizing (air) environments at 900^oC. The objective of these experiments is to test the carrier stability and reactivity and to determine the carriers' oxygen carrying capacity during redox cycles. Higher oxidation state manganese oxides (i.e., MnO_2 and Mn_2O_3) are known to be thermally unstable at elevated temperatures, as a result of which (depending on operating conditions like temperature and oxygen partial pressure), they undergo thermal decomposition to lower a oxidation state oxide[127]. Although the mechanism of gaseous oxygen release is a key principle behind CLOU, it is not the focus of this work. In our study, we are interested in avoiding the complications of simultaneous gas phase and gas-solid phase combustion reactions and aim to only investigate the gas-solid redox kinetics relevant in CLC. Thus, we choose the operation temperature of 900^oC, where Mn_3O_4 is the stable oxide in equilibrium with air[127]. In the initial stages of the experiments, hydrogen was used as the model fuel to avoid complications due to undesired carbon formation. In the later stage of the evaluation in cyclic operation, carriers were exposed to a reducing environment of methane.

4.2.2.1 Reactivity tests with H_2 as fuel

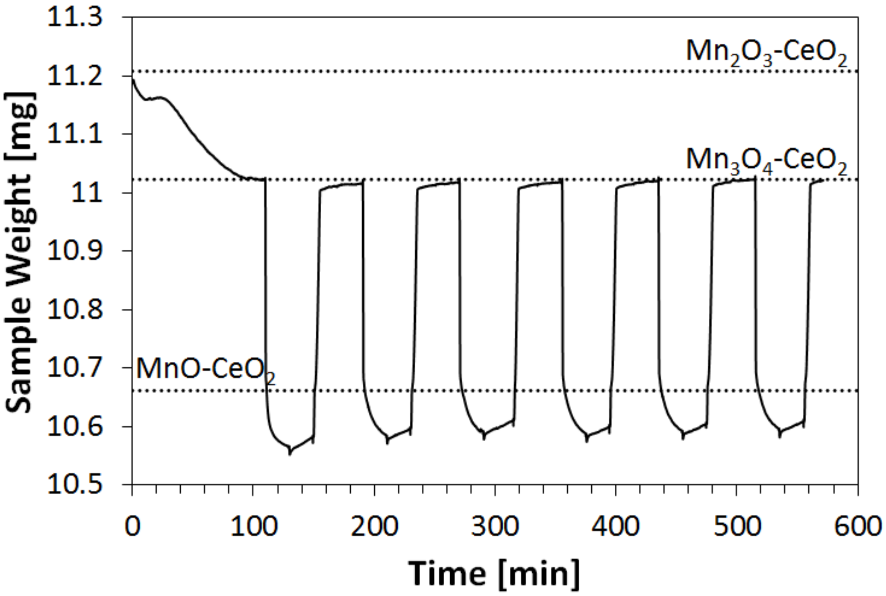

Figure 30. Stable CLC redox cycles of Mn-CeO_2 in TGA at 900°C with reduction in H_2, N_2 purge, and air oxidation (20 sccm). The dotted lines show the expected sample weight for various oxidation states of manganese (calculations based on nominal weight loading of Mn).

All TGA tests were conducted at 900°C with carriers being reduced in H_2 (10 – 30 min) and then oxidized in air (10 – 15 min) separated by a N_2 purge in between the two half cycles. Figure 30 shows six redox cycles for Mn-CeO_2 during cyclic operation with H_2 and air. The dotted lines in the figure depict the expected sample weight corresponding to various oxidation states of manganese (calculated based on metal weight loading). In TGA experiments, Mn_2O_3-CeO_2 carrier material was heated to the operation temperature under an inert atmosphere with 50°C/min ramp rate. It can be seen that sample thermally decomposes releasing oxygen and constantly loses weight upon exposure to elevated temperature. The carrier weight eventually stabilizes at Mn_3O_4-CeO_2. One can see that the carrier shows stable periodic operation in the time-frame of the experiment, which can be observed by almost identical carrier weight in reduced and oxidized state over a number of cycles. The carrier shows high reactivity with rapid loss/gain of weight in reducing/oxidizing environment. The reduction of Mn_3O_4 is restricted to MnO (confirmed in XRD, not shown here), which can also be seen from proximity of the expected and actual sample weight in post-reduction purge phase. We speculate that the extra loss of weight can be explained by reduction of ceria or the thermodynamically stable MnO phase, albeit no partially reduced MnO or elemental Mn was observed in XRD. Re-oxidation is rapid and oxidation of MnO is restricted to Mn_3O_4 oxidation state. Thus, Mn-CeO_2 shuttles between $Mn_3O_4 \Leftrightarrow MnO$ during redox cycling with reduction in hydrogen and re-oxidation in air at 900^oC. Compared to manganese, the contribution of ceria to oxygen carrying capacity is very limited, nevertheless use of ceria as support allows for stable operation of supported manganese. Moreover, the stable weight of oxygen carrier in the purge phase preceding reduction indicates that Mn_3O_4 decomposition at 900^oC is not plausible, thus eliminating any possibility of CLOU-related activity in our experiments. Similarly, other Mn_xFe_{1-x}-CeO_2 carriers that were tested for 5 – 10 cycles in CLC under the same operating conditions demonstrated stable operation (not shown here).

Compared to Mn-CeO_2, the redox cycling of these mixed oxides is more interesting to explore due to presence of the bimetallic $FeMnO_3$ phase. The last redox cycle in cyclic operation of $Mn_{0.5}Fe_{0.5}$-CeO_2 is shown in Figure 31. Dotted lines again represent the expected sample weights in various oxidation states of the carrier. From material characterization it was found that $Mn_{0.5}Fe_{0.5}$-CeO_2 upon calcination at 900^oC forms the $FeMnO_3$ phase (Figure 27d, Figure 28). Reduction of $Mn_{0.5}Fe_{0.5}$-CeO_2 is two staged. In the initial stage, exposure to hydrogen results in very rapid reduction in weight and subsequent slow reduction is preceded by a distinct break in reduction profile. It can be seen that the carrier weight corresponding to the characteristic break is in good agreement with reduction of the carrier into a physical mixture of FeO and MnO or possibly an alloy of the kind (Mn,Fe)O. Moreover, the sample weight in post-reduction purge correlates well with the mix of (MnO + Fe)-CeO_2, which was confirmed in x-ray diffraction (Figure 32a). Thus, the second stage of the reduction is conversion of (Mn,Fe)O, or wüstite, into metallic iron. It is interesting to note that the bimetallic carrier undergoes de-alloying and phase segregated iron oxide is reduced to Fe, while reduction of manganese in the presence of iron is still restricted to MnO.

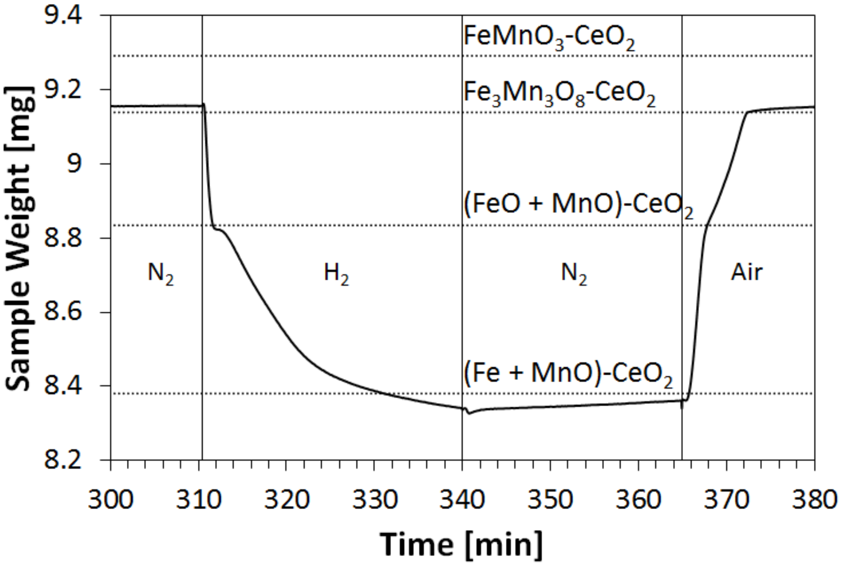

Figure 31. A CLC single redox cycle of $Mn_{0.5}Fe_{0.5}$-CeO_2 in TGA at 900°C with reduction in H_2, N_2 purge, and air oxidation (20 sccm). The dotted lines show the expected sample weight for various oxidation states of manganese (calculations based on nominal weight loadings of Fe and Mn).

Similarly, re-oxidation of the de-alloyed carrier consists of two steps with different rates of oxidation. Once again, the sample weight corresponding to the transition point between the two processes is in good agreement with the break observed in the reduction profile. Upon re-oxidation, metals undergo re-alloying forming the $Fe_3Mn_3O_8$ phase (Figure 32b). The carrier is not oxidized all the way back to $FeMnO_3$ but to a lower oxidation state of $Fe_3Mn_3O_8$. Absence of any Fe_2O_3 peaks in XRD (Figure 32b) insinuate that phase segregated iron was completely incorporated into the manganese structure. Furthermore, similar to the re-oxidation of manganese, which results in formation of Mn_3O_4 (and not Mn_2O_3), iron associated with manganese is also restricted to the $Fe^{2+/3+}$ oxidation state.

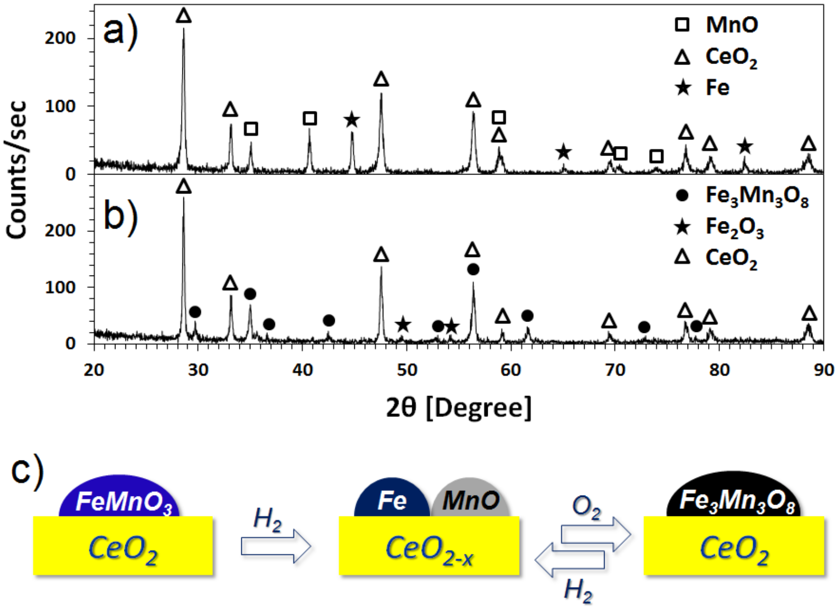

Figure 32. X-ray diffraction pattern of $Mn_{0.5}Fe_{0.5}$-CeO_2 after a) reduction in H_2 (20 sccm) and b) re-oxidation in air (20 sccm) at 900°C; c) An illustration of unusual de-alloying and re-alloying of iron and manganese observed during redox cycling of $Mn_{0.5}Fe_{0.5}$-CeO_2 in CLC at 900°C.

Unlike in the case of $Mn_{0.5}Fe_{0.5}$-CeO_2 with equal amounts of Fe and Mn, the $Mn_{0.33}Fe_{0.67}$-CeO_2 carrier with over-stoichiometric amounts of iron (i.e. Fe/Mn > 1), free iron is found to undergo oxidation to Fe_2O_3. This results in a mix of $Fe_3Mn_3O_8$ and Fe_2O_3 along-with CeO_2 (not shown here). Thus, these Mn_xFe_{1-x}-CeO_2 carriers show unusual de-alloying and re-alloying behavior which is shown here in a simple schematic (Figure 32c). Although use of ceria stabilizes the supported manganese, it is unable to alter the thermodynamics of iron and manganese oxides and maintain the integrity of the bimetallic phase during redox operation. Such atypical large-scale migration of metals when exposed to redox environment has been reported before, where reduction of the bixbyite phase resulted in formation of a (Mn,Fe)O alloy phase which subsequently bleed metallic iron[126]. Table 5 summarizes various iron and manganese phases detected by XRD at different stages of redox cycling.

Table 5. Various phases of iron and manganese detected by XRD for Mn_xFe_{1-x}-CeO_2 carriers subjected to calcination and redox cycling at 900°C. Phases in parenthesis are minor phases in the sample with only one or two peaks detected (with low intensity) in the XRD spectrum.

Carriers	Various phases containing iron and manganese (detected by XRD)		
	After calcination	After redox cycling in TGA at 900°C	
		Reduced (H_2 or CH_4)	Re-oxidized (air)
Mn-CeO_2	Mn_2O_3	MnO	Mn_3O_4
$Mn_{0.9}Fe_{0.1}$-CeO_2	Mn_2O_3	MnO, (Fe)	Mn_3O_4
$Mn_{0.8}Fe_{0.2}$-CeO_2	Mn_2O_3	MnO, (Fe)	Mn_3O_4
$Mn_{0.5}Fe_{0.5}$-CeO_2	$FeMnO_3$	MnO, Fe	$Fe_3Mn_3O_8$
$Mn_{0.33}Fe_{0.67}$-CeO_2	$FeMnO_3$, Fe_2O_3	MnO, Fe	$Fe_3Mn_3O_8$, Fe_2O_3
$Mn_{0.1}Fe_{0.9}$-CeO_2	Fe_2O_3	MnO, Fe	Fe_2O_3
Fe-CeO_2	Fe_2O_3	Fe	Fe_2O_3

In the case of Fe-rich carriers, calcined $Mn_{0.1}Fe_{0.9}$-CeO_2 only show the presence of Fe_2O_3 and no separate Mn-oxide peaks are observed in XRD (Figure 27f). These carriers were also subjected to redox cycling in TGA using H_2 as fuel and XRD of the reduced sample confirms the presence of metallic Fe along-with ill-defined peaks of MnO (Table 5). Thus, the sample shows some signs of de-alloying, and subsequent re-oxidation of the carrier only detected Fe_2O_3. This observation with the material balance in TGA indicates that in the case of Fe-rich carriers, manganese is able to go in-and-out of the Fe-oxide structure depending on the reducing or oxidizing environment.

Similarly, calcined Mn-rich carriers ($Mn_{0.9}Fe_{0.1}$-CeO_2 and $Mn_{0.8}Fe_{0.2}$-CeO_2) show presence of only Mn_2O_3. Surprisingly, carriers removed from redox cycling in the reduced state confirm formation of MnO with only one or two peaks of metallic iron in XRD (Table 5). This suggests that potentially most of the iron is still present in the MnO structure. Re-oxidation of the carriers forms Mn_3O_4 and shows no signs of the free iron oxide phase.

Table 5 provides the details of various oxides exhibited by Mn_xFe_{1-x}-CeO_2 carriers during redox cycling. With that understanding, we compare all the carriers subjected to redox cycles using hydrogen to investigate the effect of composition [i.e. Fe-content = $n_{Fe}/(n_{Fe} + n_{Mn})$] on their oxygen carrier utilization and reduction kinetics (Figure 33a). Here, carrier utilization is defined as the ratio of oxygen consumed to total oxygen in place. For example, in the case of pure iron or manganese, shuttling between $Fe_2O_3 \Leftrightarrow Fe$ or $Mn_2O_3 \Leftrightarrow Mn$ would result in carrier utilization of 1. The line going across (with a positive slope) represents the carrier utilization obtained in the case of an oxygen carrier which consists of a physical mixture of iron and manganese; moreover, it does not take into account any surplus oxygen that can be supplied by a reducible support like ceria. Since manganese is known to only shuttle between $Mn_3O_4 \Leftrightarrow MnO$ and partially utilize the oxygen, it results in a rather low carrier utilization of 0.22, as represented by that line. For the pure Fe case, carrier utilization is 1, since iron can shuttle between Fe_2O_3 ⇔ Fe. Thus, going across from pure Mn to pure Fe, the carrier utilization represented by the line continuously increases with increasing iron content. Here, the rate of reduction is represented by the rate of loss of oxygen moles (averaged over 0 – 80% oxygen utilization) [$(dn_o/dt)_{avg}$], and further normalized by weight of the oxygen carrier [W_{ox}] in the oxidized state. Typically in the end stages of reduction, the rate of oxygen loss substantially slows down due to exhaustion of active material; thus, the rate of loss of oxygen is averaged only in the range of 0 – 80% oxygen consumption.

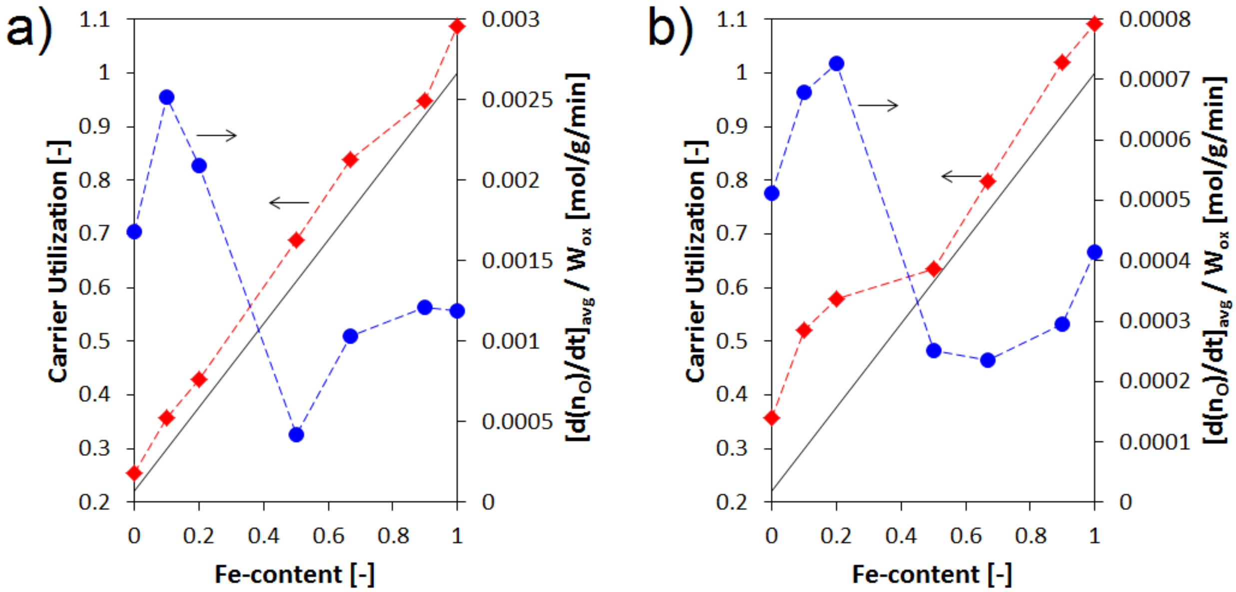

Figure 33. Carrier utilization and rate of loss of oxygen moles ($d(n_o)/dt,_{avg}$) (averaged over 0 – 80% oxygen utilization) normalized by oxide weight (W_{ox}) as a function of Fe-content for Mn_xFe_{1-x}-CeO_2 carriers in redox cycles performed in TGA at 900°C using a) H_2 and b) CH_4 as fuel. Here, gray line corresponds to the expected carrier utilization with a physical mixture of Fe- and Mn-oxides. (Here, oxygen carrier operating between Fe_2O_3 ⇔ Fe or Mn_2O_3 ⇔ Mn would result in carrier utilization = 1).

From Figure 33a, it can be seen that carrier utilization obtained during redox cycling of Mn-CeO_2 is in agreement with the carrier cycling between $Mn_3O_4 \Leftrightarrow MnO$. Similarly, as expected, Fe-CeO_2 shows complete carrier utilization. The slight increase in the carrier utilization compared to the expected theoretical values can be attributed to the reduction of ceria support. Such contribution of oxygen due to buffering capacity of reducible oxide supports has been observed before[39, 42]. In the case of Mn_xFe_{1-x}-CeO_2 carriers, carrier utilization obtained during experiments is in close agreement with the theoretical values that one would obtain with a physical mixture of iron and manganese. This makes logical sense, as we observe evidence for de-alloying of iron and manganese during reduction half cycle in TGA experiments (refer Table 5). De-alloying results in formation of free MnO and Fe; unlike FeO, which completely reduces to metallic iron, MnO being a thermodynamically stable phase cannot be reduced further. Although iron and manganese re-alloy during subsequent re-oxidation, such large-scale de-alloying eliminates any possibility of synergistic effects from combining iron and manganese with the aim of altering the thermodynamic properties of the manganese oxides.

However, from the normalized rate it can be seen that pure manganese shows a higher rate of reduction compared to iron. Additionally, doping small quantities of iron into manganese seems to further increase the rate of oxygen consumption. As observed before, iron is completely dissolved into the Mn_2O_3 structure. It is enticing to speculate that the presence of dopant in Mn_2O_3 crystals can potentially alter the nature of bound oxygen that is in place, thus making it more facile to react with the fuel. Carriers with $FeMnO_3$ as the major phase show reduced rates of oxygen loss. Such drops in the rate of oxygen release can be understood by the concurrent de-alloying of the carriers. We observe fast reduction kinetics up until formation of FeO + MnO or a mixed phase of (Mn,Fe)O (see Figure 31), and subsequent reduction is quite slow (and relatively slower than pure iron). It has been observed that reduction of (Mn,Fe)O is rather slow and consists of gradual bleed-out of iron atoms which form large iron particles big enough to be detected by XRD[126]. Thus such drops in the average rate can be attributed to the large-scale migration of iron. With Fe-rich carriers, doping of manganese seems to show marginal effects.

Overall, TGA cyclic tests with hydrogen show that in-situ de-alloying of iron and manganese hampers any possible synergy. On the contrary, the large-scale migration of iron slows down the reduction rates. Surprisingly, doping manganese with iron shows fast redox kinetics. As a next step, we look to validate these results by employing methane as fuel for CLC tests in TGA. Here, the aim is to investigate carrier stability and identify potential differences in redox performance as a function of carrier composition.

4.2.2.2 Reactivity tests with CH_4 as fuel

The objective of these experiments was to test the carriers with methane as fuel (main component of natural gas) while avoiding any sort of carbon deposition on the reduced carriers. Such carbon formation and subsequent carry-over into the oxidation half cycle is not only undesirable from a process point-of-view, but it also complicates the evaluation of the TGA experiments due to concomitant weight increase in the reduction half cycle. Thus, initial cycles were conducted to determine the maximum possible reduction time that can be used without coking the carriers. All carriers were tested for 5 – 10 redox cycles and were found to demonstrate stable operation (not shown here).

Overall, results obtained with use of methane as fuel closely match that of H_2 fueled CLC tests in TGA (see Figure 33). Once again we observe that Fe-CeO_2 utilizes complete oxygen capacity, while Mn-CeO_2 illustrates relatively low carrier capacity. Fe-rich material and carriers with $FeMnO_3$ as a major phase show a tendency to de-alloy during the reduction half cycle (see

Table 5), thus the oxygen carrying capacity or carrier utilization is restricted and is in close proximity of the Fe-Mn carriers with a physical mixture of both the oxides. Independent of the type of fuel used, Mn-CeO_2 shows a higher rate of reduction compared to Fe-CeO_2, confirming the relatively high reactivity of manganese supported on ceria. Due to the presence of concomitant de-alloying of the $FeMnO_3$ containing carriers, the average rate of reduction goes down, which can again be attributed to the slow reduction of (Mn,Fe)O oxide. As of now, we do not completely understand the reason behind the relatively lower rate of reduction for $Mn_{0.1}Fe_{0.9}$-CeO_2 compared to Fe-CeO_2 carriers, but the Fe-rich carrier trends obtained with use of CH_4 as fuel are in good agreement with those that use H_2 as fuel.

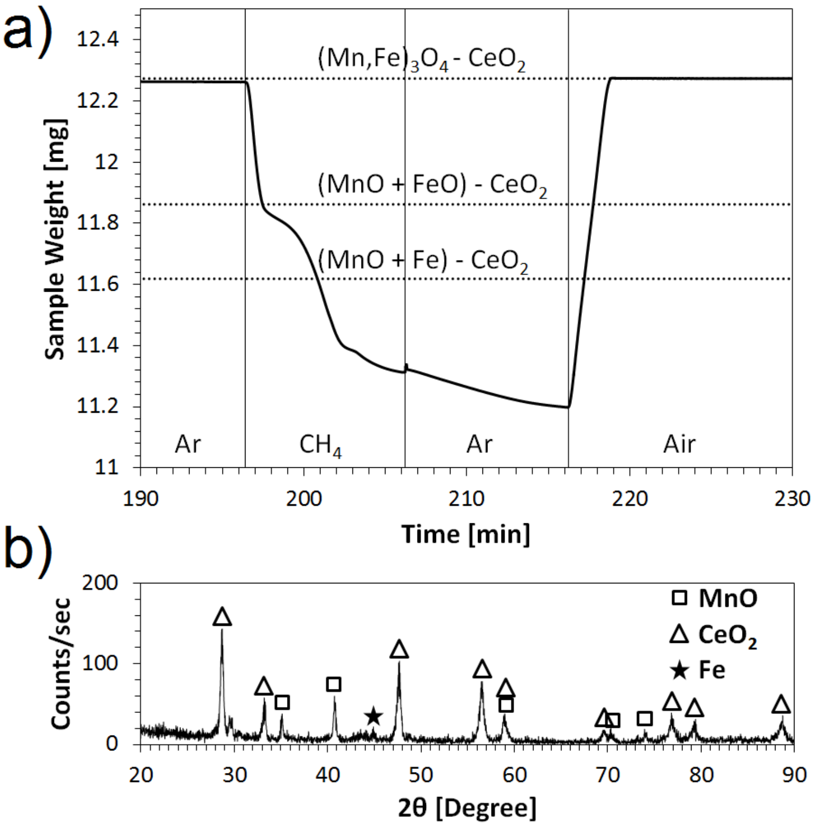

Figure 34. a) A single redox cycle of $Mn_{0.8}Fe_{0.2}$-CeO_2 in TGA at 900°C using CH_4 as fuel (5 sccm), argon purge (20 sccm) and air oxidation (20 sccm); b) XRD of $Mn_{0.8}Fe_{0.2}$-CeO_2 carrier after reduction in TGA using CH_4 at 900°C.

However, in case of Mn-rich carriers, we see the consistent increase in the rate of reduction while using both H_2 and CH_4 as fuels. Since we don't observe a distinct phase of metallic Fe, we believe that most of the iron is still in the Mn-oxide structure during the redox cycle, and thus accelerates the oxygen release. Interestingly, unlike in the TGA tests with H_2 as fuel, Mn-CeO_2 and Mn-rich carriers show a clear increase in the oxygen carrying capacity when redox cycles are fueled with methane. This observation is counter-intuitive, as carbon based fuels are less reactive compared to pure hydrogen. Moreover, the oxygen carrying capacity seems to increase with increasing amounts of doping of iron into the manganese structure. Such Mn-rich oxygen carriers were also found to show higher activity and oxygen release capacity in CLOU tests[128]. The unusual increase in the carrier utilization cannot alone be explained by the deeper reduction of ceria or complete reduction of iron within the manganese structure.

Figure 34a shows a cycle in detail for $Mn_{0.8}Fe_{0.2}$-CeO_2 carriers using CH_4 as fuel at 900°C. It can be seen that upon exposure to reducing environment the sample rapidly loses weight and forms the (Mn,Fe)O phase or mix of FeO and MnO. Further reduction to MnO and Fe does not show a distinct break in the weight curve, and the carrier loses a lot more weight than estimated (with reduction rates higher than that of bulk ceria reduction, which is inherently sluggish[42]). Moreover, the sample in the reduced state shows no distinctly clear phase of Fe but a single very low intensity peak is observed, which indicates that iron is still present in the MnO structure (see Figure 34b). EELS analysis (not shown here) on the $Mn_{0.8}Fe_{0.2}$-CeO_2 also failed to detect any phase segregated iron particles, and iron was found to be in close vicinity of manganese, which supports the above argument. Thus, based on the observations, one can hypothesize that during reduction of the (Mn,Fe)O phase, Fe^{2+} occupying the Mn^{2+} sites in the fcc structure might be undergoing reduction to form Fe^0 centers. Formation of such species can create unsatisfied valances in the MnO structure, possibly making it more facile to reduce. However, we only observe the MnO phase in XRD (Figure 34b), and no metallic manganese phase is detected. Detection of such an unstable phase (e.g. MnO_{1-y}) would be difficult, as it might undergo oxidation while transferring the sample from TGA to XRD in ambient conditions.

Thus, use of Mn_xFe_{1-x}-CeO_2 oxides with a bixbyite or hematite phase are unable to demonstrate any sort of synergistic effect due to the accompanying de-alloying behavior of carriers during reduction half cycle. On the other hand, surprisingly, Mn-rich oxides doped with some iron are found to be much more reactive than pure manganese. Moreover, stable weights of all Mn_xFe_{1-x}-CeO_2 mixed oxides at 900^oC during the CLC purge phase (prior to reduction in TGA) indicates that CLOU activity is absent or minimal at our experimental conditions. As a last step, we conduct redox tests in a fixed-bed reactor to understand the fuel conversion, product selectivity, and also to validate the above observations in TGA experiments.

4.2.3 Reactivity tests in fixed-bed reactor

TGA reactive tests provide important insights into carrier reactivity, oxygen carrying capacity and stability of the oxygen carrier materials, however the flow configuration (and hence gas-solid contacting pattern) in a TGA are not representative of conditions in fixed-bed or fluidized bed reactors. TGA also does not yield any understanding of fuel conversion or product selectivity for the fuel conversion. Selectivity in the fuel oxidation reaction is a critical parameter in comparing carriers' efficacy in the CLC process, as CLC aims at maximizing the carbon capture via complete combustion of fuel to CO_2 and steam. Herein, side reactions like partial oxidation of fuel and pyrolysis are undesired. Thus, as a last step in the present investigation Mn_xFe_{1-x}-CeO_2 carriers were subjected to redox operation in a fixed-bed reactor configuration.

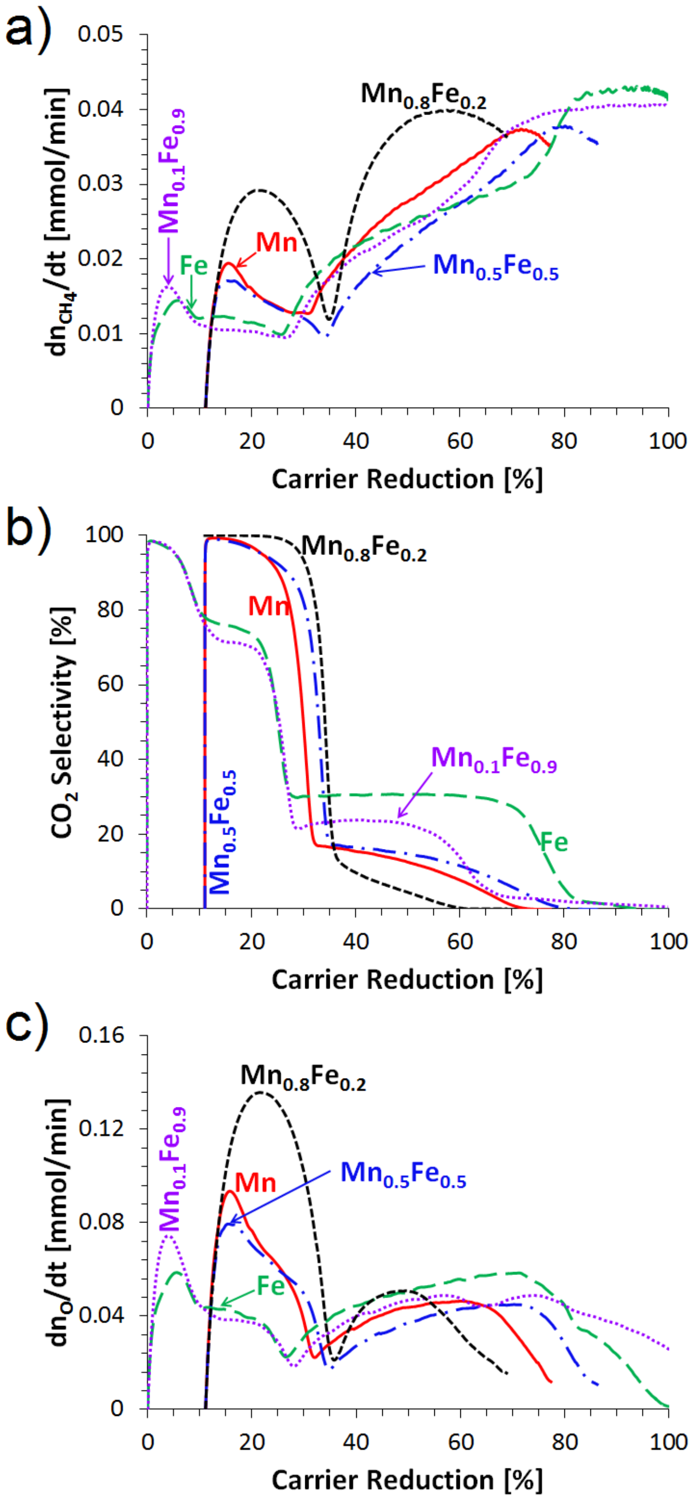

Figure 35. Comparison of a) rate of methane conversion, b) CO_2 selectivity and c) rate of oxygen consumption as a function of carrier reduction for select Mn_xFe_{1-x}-CeO_2 carriers during reduction with methane (16.7 vol.%, 1 sccm) in fixed-bed reactor at 900°C.

Figure 35 compares performance of some Mn_xFe_{1-x}-CeO_2 carriers during methane reduction in the fixed-bed reactor. For comparison purposes, we distinguish the mixed oxide carriers in three different sets, depending upon the nature of their bimetallic phase. We compare i) monometallic iron and iron doped with manganese ($Mn_{0.1}Fe_{0.9}$-CeO_2), ii) monometallic manganese and manganese doped with iron ($Mn_{0.8}Fe_{0.2}$-CeO_2), and iii) a bixbyite phase of iron and manganese ($Mn_{0.5}Fe_{0.5}$-CeO_2) with pure Mn-CeO_2. Figure 35 compares the results of the above-mentioned carriers in the form of rate of methane conversion (Figure 35a), CO_2 selectivity (Figure 35b), and rate of consumption of oxygen in carrier (Figure 35c) plotted as functions of % carrier reduction. As a convention in this study, the oxidation state of Fe_2O_3 or Mn_2O_3 is considered to be the fully oxidized state of the carrier. Utilizing the knowledge of various oxidation states observed in TGA studies (in re-oxidized state, determined by XRD analysis) and aforementioned nomenclature, we can state that carrier reduction of Fe-CeO_2 and $Mn_{0.1}Fe_{0.9}$-CeO_2 begins at carrier reduction equal to zero, as the re-oxidized carriers were found to exist in the Fe_2O_3 state. However, in the case of monometallic manganese, doped Mn-based carriers and $Mn_{0.5}Fe_{0.5}$-CeO_2 carriers were re-oxidized to Mn_3O_4 or $Fe_3Mn_3O_8$. This accounts for a loss of 11.1% of oxygen carrying capacity (e.g. $Mn_2O_3 \Leftrightarrow Mn_3O_4$), thus the carrier reduction starts at 11.1%.

In the case of Mn-CeO_2, the initial reduction of the carrier from Mn_3O_4 to MnO is highly selective for total oxidation (see Figure 35b), and it also demonstrates a relatively higher rate of oxygen carrier consumption (see Figure 35c) compared to subsequent reduction of the carrier. It should be noted that, under the reducing environment of methane, reduction of Mn-oxide below MnO is observed, as shown in Figure 35. Both the observations are in good agreement with TGA studies. Comparing the CO_2 selectivity of Fe- and Mn-CeO_2, we can see that Fe-CeO_2 is only selective towards total oxidation during reduction from Fe_2O_3 to Fe_3O_4 (which would account for ~11% of the oxygen in place). In contrast, Mn-CeO_2 shows high CO_2 selectivity during reduction of Mn_3O_4 to MnO (equivalent to ~22% of oxygen consumption). Although fuel conversion is incomplete in the current set of operating conditions, when compared to monometallic iron, manganese-based carriers show higher reactivity, which is depicted as rate of consumption of fuel and oxygen carrier. Thus, use of Mn-CeO_2 instead of Fe-CeO_2 not only results in higher carrier reactivity, but it also doubles the usable fraction of the oxygen carrier.

Furthermore we compare the effect of combining iron and manganese together. Firstly, comparing Fe- and $Mn_{0.1}Fe_{0.9}$-CeO_2 carriers, it can be seen that doping small amounts of manganese in iron does not significantly enhance the carrier reactivity. Both the fuel conversion and rate of oxygen loss from the carrier show a marginal improvement in the case of $Mn_{0.1}Fe_{0.9}$-CeO_2. The first ~11% of carrier reduction, which correlates well with transition of carrier from Fe_2O_3 to $Fe_3O_{4,}$ is selective for total oxidation, but it does not show any improvement upon doping the pure iron with manganese. The Fe-rich carriers do not show any added benefits for total oxidation of methane, which is the focus of the present report, albeit the improved fuel consumption during later stages of the reduction is promising for partial oxidation of methane (not shown here).

Secondly, we compare the monometallic Mn-CeO_2 and bimetallic $Mn_{0.5}Fe_{0.5}$-CeO_2 to probe for any possible improvement in carrier performance due to the bixbyite alloy phase of iron and manganese. One can see that alloying the iron and manganese in the form of the $FeMnO_3$ does not improve the carrier reactivity, which is evident from similar rates of fuel and oxygen consumption in both the cases. On the other hand, when compared to Mn-CeO_2, one can argue that the concurrent de-alloying of the carriers can be the cause for relatively low rates of methane conversion with $Mn_{0.5}Fe_{0.5}$-CeO_2. As observed in TGA, de-alloying of the carrier during the reduction process should result in formation of metallic iron, therefore increasing the overall oxygen carrying capacity of the carriers. Higher extents of carrier reduction of $Mn_{0.5}Fe_{0.5}$-CeO_2 carriers compared to Mn-$CeO_{2,}$ as shown in Figure 35, support this argument.

Lastly, we compare the effect of doping manganese with some iron. We can clearly see that Mn-rich carriers ($Mn_{0.8}Fe_{0.2}$-CeO_2) results in sharp increases in the reactivity of the carriers with near 100% selectivity for CO_2 formation during initial conversion of $(Mn,Fe)_3O_4$ to (Mn,Fe)O, which results in ~11% to ~33% carrier reduction. During the abovementioned reduction, it can be seen that Mn-rich carriers demonstrate high rates of methane and oxygen carrier conversion compared to Mn-$CeO_{2,}$ which is in good agreement with our TGA results. Such unusual increases in the carrier reactivity have been previously observed in context of chemical looping oxygen uncoupling studies conducted in a batch-fluidized bed reactor[128-129]. Doping iron into the manganese structure can potentially make the release of lattice oxygen more facile. Although the cause of such dramatic increases in the carrier reactivity is not completely understood at this point, it is a very promising direction for further development of manganese-based carriers. Better understanding of the root cause for such behavior can further allow us to tailor the metal phase of the oxygen carriers and improve their reactivity in CLC.

4.2.4 Brief comments on process engineering aspects of using Fe- and Mn-based carriers

The metals chosen in the present investigation (iron and manganese) are abundant, environmentally benign and both are relatively inexpensive candidates when compared to highly reactive and expensive metals like nickel and copper. However, as demonstrated in the present work, compared to iron which is currently considered to be a most suitable candidate for CLC, manganese shows higher reactivity and doubles the usable oxygen carrying capacity (refer Figure 33 and Figure 35) selective for total oxidation of methane ($Mn_3O_4 \Leftrightarrow MnO$ vs $Fe_2O_3 \Leftrightarrow Fe_3O_4$). This increased oxygen carrying capacity and carrier reactivity can help reduce the solid inventory of oxygen carrier in the looping reactors. Furthermore, from the process point-of-view, uses of Mn-CeO_2 carriers provide another opportunity to alleviate the complexity of heat integration between a generic endothermic reducer (with the exception of copper) and exothermic air reactor. The following set of equations (R19 – R22) show the heat of reaction at 900^oC for reduction and oxidation in Fe- and Mn-based systems. It can be seen that use of manganese ($Mn_3O_4 \Leftrightarrow MnO$) results in an exothermic reducer as well as oxidizer, which is not the case with use of iron ($Fe_2O_3 \Leftrightarrow Fe_3O_4$). Thus, employing manganese-based carriers also potentially presents an opportunity for effective use of fixed-bed reactors in CLC applications with an autothermal mode of operation.

Iron ($Fe_2O_3 \Leftrightarrow Fe_3O_4$):

Reduction: $12\ Fe_2O_3 + CH_4 = 8\ Fe_3O_4 + CO_2 + 2\ H_2O$ $\Delta H_R = +\ 149.2$ kJ/mol…(R19)

Oxidation: $8\ Fe_3O_4 + 2\ O_2 = 12\ Fe_2O_3$ $\Delta H_R = -\ 950.6$ kJ/mol …(R20)

Manganese ($Mn_3O_4 \Leftrightarrow MnO$):

Reduction: $4\ Mn_3O_4 + CH_4 = 12\ MnO + CO_2 + 2\ H_2O$ $\Delta H_R = -\ 103.0$ kJ/mol …(R21)

Oxidation: $12\ MnO + 2\ O_2 = 4\ Mn_3O_4$ $\Delta H_R = -\ 698.4$ kJ/mol …(R22)

Net Reaction of Combustion:

$CH_4 + 2\ O_2 = CO_2 + 2\ H_2O$ $\Delta H_R = -\ 801.4$ kJ/mol …(R23)

4.3 SUMMARY

In the present study, mono- and bimetallic Fe and Mn carrier materials were synthesized using a low cost, scalable technique using ceria as support material. The obtained carriers were evaluated with regard to their bimetallic phase stability, reactivity, oxygen carrying capacity and cyclic redox stability using H_2 and CH_4 as fuels in TGA and fixed-bed reactor studies.

We observe that use of ceria as support facilitates excellent phase stability and consistent redox operation of supported manganese, which is typically prone to react with the support matrix forming spinel structures inert in redox cycling e.g. Al_2O_3. Furthermore, both TGA and fixed-bed reactor studies confirm the high reactivity and oxygen carrying capacity of Mn-CeO_2 in CLC compared to Fe-CeO_2 ($Fe_2O_3 \Leftrightarrow Fe_3O_4$; ~11% vs $Mn_3O_4 \Leftrightarrow MnO$; ~22%). Thus, better redox kinetics and oxygen carrying capacity coupled with low toxicity and favorable thermodynamics of the reduction half process make Mn-based oxygen carriers an attractive and pragmatic alternative to iron.

Upon redox cycling of Mn_xFe_{1-x}-CeO_2 carriers it was found that carriers show stable redox operation, however carriers with a bixbyite $FeMnO_3$ phase showed large scale migration of iron and manganese phases. These carriers were found to undergo de-alloying during reduction forming a mix of Fe and MnO, and subsequently were observed to re-alloy during the re-oxidation half process. As a result, combining iron and manganese in such carriers was not beneficial. However, the sluggish de-alloying of these carriers has an adverse effect on the carrier reactivity. On the other side of the spectrum, in case of manganese doped with iron ($Mn_{0.8}Fe_{0.2}$-CeO_2 and $Mn_{0.9}Fe_{0.1}$-CeO_2), a strong improvement in the carrier reactivity was observed over Mn-CeO_2 in TGA and fixed-bed studies.

Overall, our results show that combining relatively low reactive metals like iron and manganese can also yield synergistic effects: By replacing an inherently reactive dopant (like Ni or Cu) by a low cost, low reactivity and environmentally benign Fe, we can not only augment the carrier reactivity at reduced cost, but also potentially mitigate the environmental impact of using such synthetic oxygen carriers. Although these doped oxygen carriers show significant improvement over monometallic Fe or Mn, Mn_xFe_{1-x}-CeO_2 mixed-oxides are inherently complex system to analyze. Therefore, it is important to further the mechanistic understanding of redox processes of these carriers to be able to clearly elucidate the most critical parameter for oxygen carrier design. Nevertheless, the present results suggest that systematic engineering of the metal phase of oxygen carriers and use of support material active in oxygen transport can strongly improve the reactivity of synthetic manganese-based oxygen carriers in the looping process.

5.0 CHEMICAL LOOPING – A NOVEL PROCESS FOR SYNGAS GENERATION VIA PARTIAL OXIDATION OF METHANE

Up until now the work was mainly focused on optimizing the carrier materials' structure and composition to maximize their activity for total oxidation in CLC – an emerging technology for clean combustion of fossil-fuels with inherent CO_2 capture. However, a recent boost in the domestic natural gas reserves has been a strong incentive for developing novel processes to convert natural gas into valuable chemicals. Therefore, in the present work, we apply the chemical looping principle for partial oxidation of methane (CLPOM) in fixed-bed reactor with aim to produce synthesis gas – a valuable feedstock used in production of value added chemicals and vast array of intermediates.

As explained before (section 1.2.1), chemical looping can be used for partial oxidation of methane by limiting the oxidation of fuel in the reducer while the oxidizer half of the process remains the same. Conceptually, performing methane partial oxidation in chemical looping configuration is more advantageous over conventional steam reforming of methane (SRM) and catalytic partial oxidation of methane (CPOM). Flameless oxidation of fuel and inherent separation of oxygen from air by oxygen carriers makes the CLPOM process more economical and safe to operate compared to SRM and CPOM. Chemical looping has been used for syngas generation either by adjusting the C/O ratio in the reducer reactor or by selection of carriers which are inherently selective for syngas formation. For example, high reactivity of nickel has been the impetus behind its use as a carrier material for partial oxidation, but it suffers from coke formation. On the other hand, iron-based materials are selective but lack sufficient reactivity[66].

Therefore, in the present work, we aim to maximize selectivity and reactivity for syngas generation by optimizing both factors: i) selection of appropriate oxygen carrier and ii) operation of redox process to tune C/O ratio in the fuel reactor. To that effect, we synthesize mixed oxides of iron and nickel with the aim of combining the high reactivity of nickel with selective oxidation properties of iron. These mixed metal oxides of Fe and Ni are supported on ceria. A reducible oxide like ceria, known for its oxygen buffering capacity, was chosen as support matrix because it strongly assists in oxygen transport and is observed to show improved oxygen carrying capacity of supported metal[39, 42]. Secondly, these oxygen carriers were then scanned in the fixed-bed reactor to determine the most optimal candidate for syngas generation. The selected carrier was then partially reduced in methane to form syngas. The carrier was only partially reduced to avoid coke formation, which is typically associated with deeper carrier reduction. Subsequently, the carrier was subjected to incomplete re-oxidation to avoid over-oxidation of carriers that results in CO_2 formation in subsequent reduction steps. Thus, by changing the duration of reduction and oxidation, the relative amount of oxygen and carbon in the fuel reactor was tuned to suppress CO_2 and coke formation. As a last step, a brief reactor modelling study was conducted to evaluate the feasibility of conducting CLPOM in a periodically operated fixed-bed reactor in order to avoid carrier attrition, which is typically associated with the use of fluidized bed reactors.

5.1 EXPERIMENTAL

5.1.1 Carrier synthesis and characterization

Since metal-based carriers act as a source of oxygen for fuel oxidation, a large solid inventory in the reactors can be anticipated. Therefore synthesis of oxygen carriers using low-cost and scalable techniques is critical in limiting the cost of oxygen carrier manufacturing. Previously (chapters 2.0, 3.0, 4.0) we have seen that use of reducible oxides like ceria renders the supported metal phase thermally stable and more reactive in redox processes. Thus, in this study oxygen carriers were synthesized in a simple and scalable two-step procedure. First the ceria support was synthesized, and Fe and Ni were deposited by incipient wetness technique.

Ceria was synthesized according to the procedure previously explained in section 2.1.1. Mixed oxides of iron and nickel (Ni_xFe_{1-x}-CeO_2) with 40 wt.% FeNi weight loadings were synthesized by simple incipient wetness technique explained in section 2.1.1. Ni_xFe_{1-x}-CeO_2 carriers (x = 0, 0.02, 0.12, 0.33 and 1) were prepared to investigate the effect of doping less reactive iron with nickel on partial oxidation activity during reduction with methane. Obtained carriers were calcined at temperatures at 900^{o}C.

The obtained oxygen carriers were subjected to various characterization techniques to better understand the structural and textural properties of the carriers. The specific surface area was determined via nitrogen sorption in a Micromeritics ASAP 2020 gas adsorption analyzer using the BET method. Prior to the measurement, the samples were degassed for 2 h at 200^{o}C under high vacuum. After calcination at 900^{o}C for 2 h, all the carriers were found to have surface area <8 m^2/g (refer Table 6). The relatively low surface area of the carriers after calcination at 900^{o}C can be explained by the limited thermal stability of ceria at high temperatures[98-99, 109-110].

As reported in Table 6, actual wt.% of FeNi metals in carriers (obtained by EDAX) are in close agreement with the nominal weight loadings.

Table 6. Summary table of characterization results for Ni_xFe_{1-x}-CeO_2 carriers subjected to calcination at 900°C. (Phases marked with asterisk (*) are minor phases).

Oxygen Carrier	BET surface area (m^2/g)	Various phases of iron and nickel detected by XRD	Ni weight loading (wt.%)	
			Targeted	Actual (EDAX)
Fe-CeO_2	3.5	Fe_2O_3, CeO_2	0	- (Fe wt.% = 42.4)
$Ni_{0.02}Fe_{0.98}$-CeO_2	2.7	Fe_2O_3, $NiFe_2O_4^*$, CeO_2	1	3.1
$Ni_{0.12}Fe_{0.88}$-CeO_2	0.7	Fe_2O_3, $NiFe_2O_4^*$, CeO_2	5	8.6
$Ni_{0.33}Fe_{0.67}$-CeO_2	3.6	$NiFe_2O_4$, CeO_2	13.78	14.5
Ni-CeO_2	7.7	NiO, CeO_2	40	40.9

X-ray diffraction (XRD) measurements were performed with a powder X-ray diffractometer (Phillips PW1830) in line focus mode employing Cu Kα radiation ($\lambda = 1.5418$ Å) with typical 2θ scans between 15° and 90°. Crystal phases were identified based on JCPDS cards. XRD results are summarized in Table 6. In all Ni_xFe_{1-x}-CeO_2 cases there were no interactions between the supported metal phase/s and the ceria support. In carriers with low doping of nickel (i.e., x = 0.02, 0.12 in Ni_xFe_{1-x}-CeO_2), Fe_2O_3 was observed to be the major phase, while $NiFe_2O_4$ was observed as a minor phase (characterized by some very weak intensity peaks in XRD). For $Ni_{0.33}Fe_{0.67}$-CeO_2, $NiFe_2O_4$ was the only Fe-Ni phase detected along with CeO_2. In case of mono-metallic carriers, only Fe_2O_3 and NiO phases were detected with CeO_2 respectively.

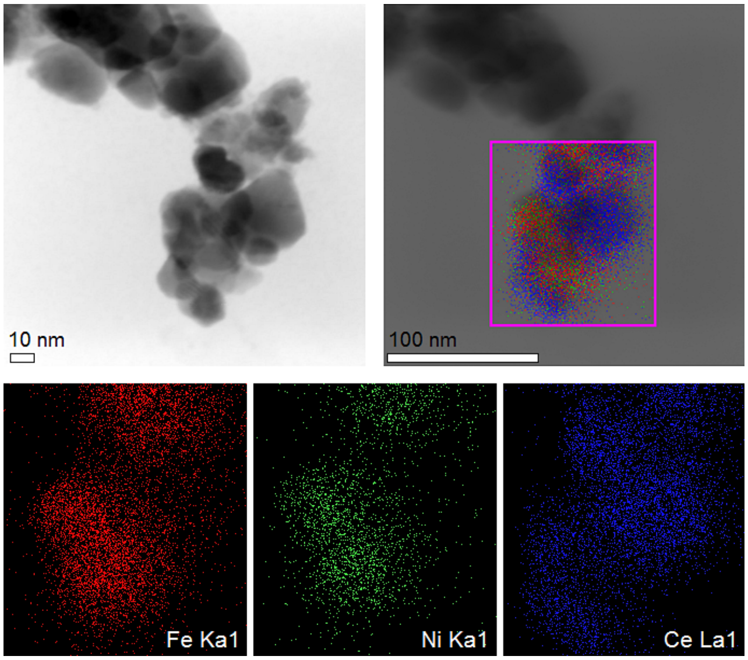

Figure 36. (top left) TEM, (top right) TEM with superimposed elemental map and (bottom) elemental distribution of individual elements Ni (left), Fe (middle) and Ce (right) in $Ni_{0.12}Fe_{0.88}$-CeO_2 carrier calcined at 900°C in 0.2 SLM air for 2 h. EELS analysis confirms occurrence of iron and nickel in close vicinity at nanometer scale.

In the case of Ni-doped carriers, to better understand the structure-activity relations, it is important to understand the dispersion of nickel in the metal phase. Thus, JEOL JEM-2100F high-resolution transmission electron microscope (HR-TEM) was used to conduct electron energy-loss spectroscopy (EELS) to be able to determine local spatial elemental composition in the sample. Figure 36 shows the EELS analysis for a typical $Ni_{0.12}Fe_{0.88}$-CeO_2 sample, which suggests that nickel is well dispersed in the sample and occurs in close proximity of iron.

Furthermore, there are no independent large islands of nickel observed; this has been confirmed in the XRD which is devoid of NiO peaks (not shown here).

5.1.2 Reactive tests

Initially, carriers were subjected to extended reduction using methane in fixed-bed experiments to investigate for their reactivity and selectivity for CH_4 conversion to H_2 and CO (with desired ratio of H_2:CO ~2). These experiments were used to determine the carrier reduction range that is selective for partial oxidation of methane. Selected carriers were then subjected to multi-cycle fixed-bed CLPOM operation where carriers were partially reduced and subsequently incompletely regenerated to maximize syngas formation and abate/eliminate the methane conversion to total oxidation or methane cracking products. Operating conditions and experimental set-up for fixed-bed tests were kept identical to previous studies. See section 2.1.2 for details of experimental set-up.

5.2 RESULTS AND DISCUSSION

5.2.1 Fixed-bed reactor extended reduction in methane

5.2.1.1 Monometallic iron and nickel

Depending on the nature of oxygen carrier and available oxygen to carbon ratio, methane conversion can result in total oxidation, partial oxidation or catalytic cracking. Therefore, to effectively utilize the oxygen carrier for partial oxidation of methane, one has to understand the entire spectrum of products obtained at various stages of the reduction of oxygen carrier using methane. To this effect, we subject the oxygen carriers to reduction in methane and analyze the composition of effluent product gases from the fixed-bed reactor as a function of conversion i.e. reduction of oxygen carrier.

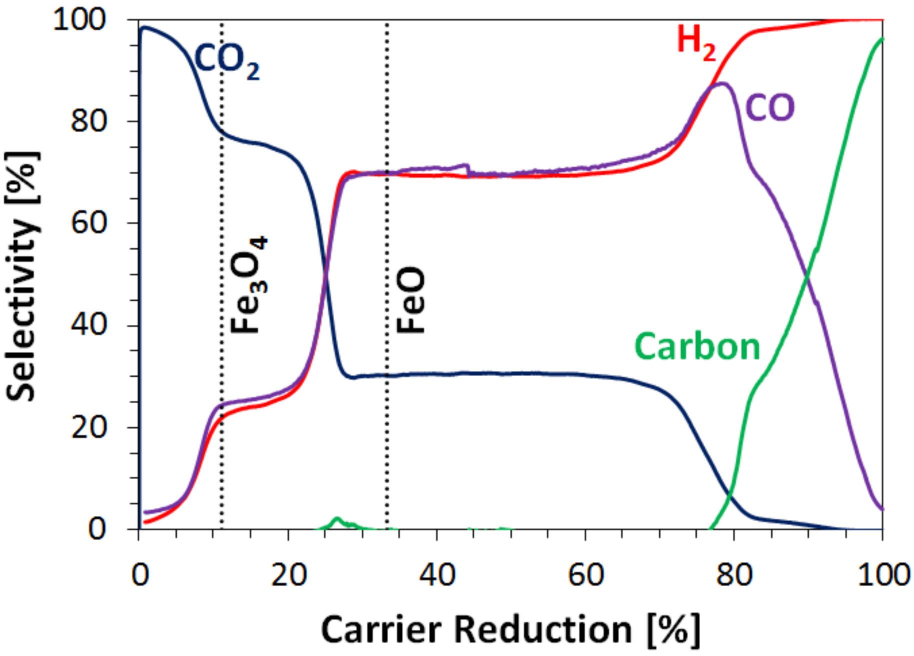

Figure 37. Selectivity of various products as a function of carrier reduction during reduction of 100 mg Fe-CeO_2 fixed-bed at 900°C with methane (16.7 vol.%, 1sccm).

Figure 37 traces the selectivities of various products as a function of % carrier reduction in the case of Fe-CeO_2. The dotted vertical lines in the graph represent the % carrier reduction corresponding to various oxidation states of iron oxide. It can be seen that upon contacting methane with completely oxidized iron, i.e. Fe_2O_3, methane conversion shows high selectivity for CO_2 formation. Thus with a large reservoir of oxygen in place, i.e. with high oxygen to carbon ratio, methane conversion is driven towards total oxidation to form CO_2 and H_2O. Overall, the reduction of Fe_2O_3 to form Fe_3O_4 is very selective towards the total oxidation of methane, which is well known in chemical looping community[29, 39]. Further reduction of carrier from Fe_3O_4 to FeO can be thought of as a transition period where selectivity for total oxidation drops while that of partial oxidation gradually increases. However, continued reduction of carrier from FeO to metallic iron predominantly favors partial oxidation to form syngas with selectivities 70% and above. Almost identical selectivities of H_2 and CO (which are normalized by stoichiometric coefficient) also indicate a syngas ratio (H_2:CO) close to two. Compared to total oxidation of methane, partial oxidation stoichiometrically requires only one-fourth the amount of oxygen. Thus, with greater extent of carrier reduction, the oxygen reservoir is depleted, and the oxygen to carbon ratio drops. This causes the methane conversion to become more selective towards syngas generation. As the oxygen carrier gets completely reduced, methane cracking is favored, which is indicated by rising carbon selectivities and concurrently receding CO selectivity. Thus, we observe that various oxidation states of iron are selective towards different methane conversion pathways. In other words, the degree of oxidation of carrier or oxygen to carbon ratio can selectively drive the methane conversion towards total or partial oxidation.

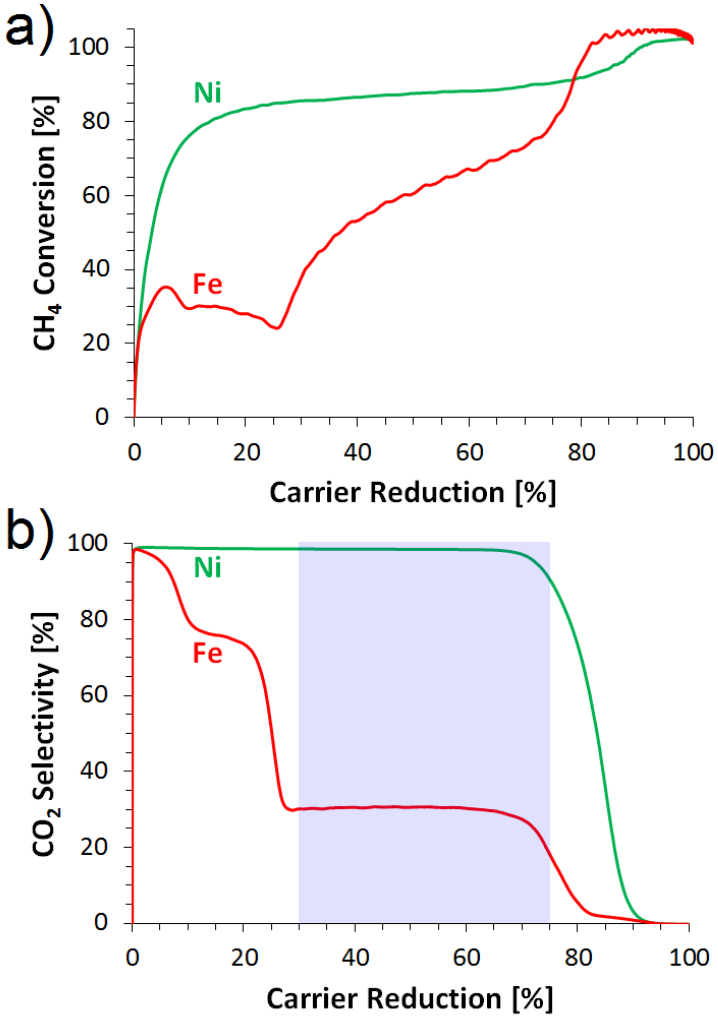

Figure 38. a) Methane conversion and b) CO_2 selectivity during reduction of Fe- and Ni-CeO_2 in a fixed-bed reactor at 900°C using methane (16.7 vol.%, 1sccm). The shaded box in the graph of CO_2 selectivity shows an approximate optimal window of carrier reduction (30 – 75%) for redox cycling of Fe-CeO_2 with aim to effectively generate of syngas while avoiding undesired products like total oxidation and soot/coke formation.

For efficient generation of syngas using Fe-CeO_2 one has to avoid i) the initial period of reduction which is selective for total oxidation of methane (carrier reduction < 30%) and ii) deeper reduction of carrier that promotes methane cracking (carrier reduction > 75-80%). In terms of operation, the oxygen carrier needs to be partially reduced and then only partially re-oxidized to maximize CO selectivity in CLPOM operation. Thus, in the case of Fe-CeO_2, operation of redox cycles roughly in the window of 30 – 75% carrier reduction is necessary for maximizing the formation of desired product, i.e. syngas. The range of carrier reduction/conversion favorable for partial oxidation is shaded in Figure 38b which depicts CO_2 selectivity for Fe- and Ni-CeO_2. One can observe that in this shaded region selectivity for total oxidation will be minimal for Fe-CeO_2, and substantial selectivity for carbon formation is seen after carrier reduction of ~80% (refer Figure 37). During reduction, if the initial phase of total oxidation and later methane cracking is avoided, iron-based carriers seem to be an appropriate choice of metal for partial oxidation of methane, albeit its activity to convert methane is low, which can be seen from the methane conversion in Figure 38a. Fe-CeO_2 shows near complete conversion only when the carrier is more than 75-80% reduced, however this reduction leads to methane cracking (refer Figure 37).

On the other hand, nickel is known for its good C-H scission activity[62, 123]. Thus, we also tested Ni-CeO_2 in methane reduction, which, in comparison to iron, shows much improved methane conversion (see Figure 38a). However, as shown in Figure 38b, during the initial 80% of carrier reduction, nickel is almost exclusively selective for total oxidation of methane. Subsequent reduction of nickel shows strong activity for partial oxidation (not shown), but compared to iron, it yields a very small fraction of usable oxygen with a narrow window of operation for syngas generation. Since metallic nickel is the most studied non-noble metal catalyst in catalytic partial oxidation of methane[135], the observation that nickel is not the primary choice of metal is counter-intuitive. It should be noted that the metallic state of nickel (Ni^0) is catalytically active in syngas generation, but in this study we are interested in partial oxidation of methane using molecular oxygen associated with metal. Thus, we observe that, unlike Ni^0, nickel associated with oxygen, i.e. nickel oxide (NiO_x), is primarily selective for total oxidation.

5.2.1.2 Tailoring the metal phase

In the previous section we observed that iron is selective for partial oxidation but shows poor methane conversion, whereas nickel is not selective for syngas generation but has excellent methane conversion activity. To get the best of both the worlds, we combine iron and nickel together at various ratios and tailor the metal phase to produce an oxygen carrier that demonstrates good activity in methane conversion (due to C-H bond scission activity of nickel) as well as good selectivity for partial oxidation (due to low oxidation strength of iron oxides).

Figure 39a shows the CO selectivity for various Ni_xFe_{1-x}-CeO_2 carriers during extended reduction in a fixed-bed reactor at 900^oC. It can be seen that amount of nickel present in the metal phase has a significant impact on the CO selectivity. One can observe that monometallic iron demonstrates good CO selectivity right from ~30% carrier reduction, whereas pure nickel is more selective towards total oxidation of methane and shows noticeable CO selectivity for a very small fraction of carrier utilization, i.e., 80 – 95% carrier reduction. Thus, as one would expect, an increase in the amount of nickel would result in diminishing CO selectivity. Figure 39a confirms that the behavior of FeNi carriers is along the same lines; i.e., increasing nickel reduces the CO selectivity. Using moderate amounts of nickel doping (e.g. $Ni_{0.12}Fe0_{.88}$-CeO_2), however, still maintains good CO selectivity with a higher peak CO selectivity compared to that of iron. Additionally, combining iron with nickel results in carriers that begin methane cracking at an earlier stage in the carrier reduction. This can be seen from the CO selectivity that falls off precipitously after the strong peak. To objectively compare all the carriers, it is necessary to first understand the effect of Ni-doping on syngas ratio and then compare the carriers during the reduction period that mainly favors partial oxidation.

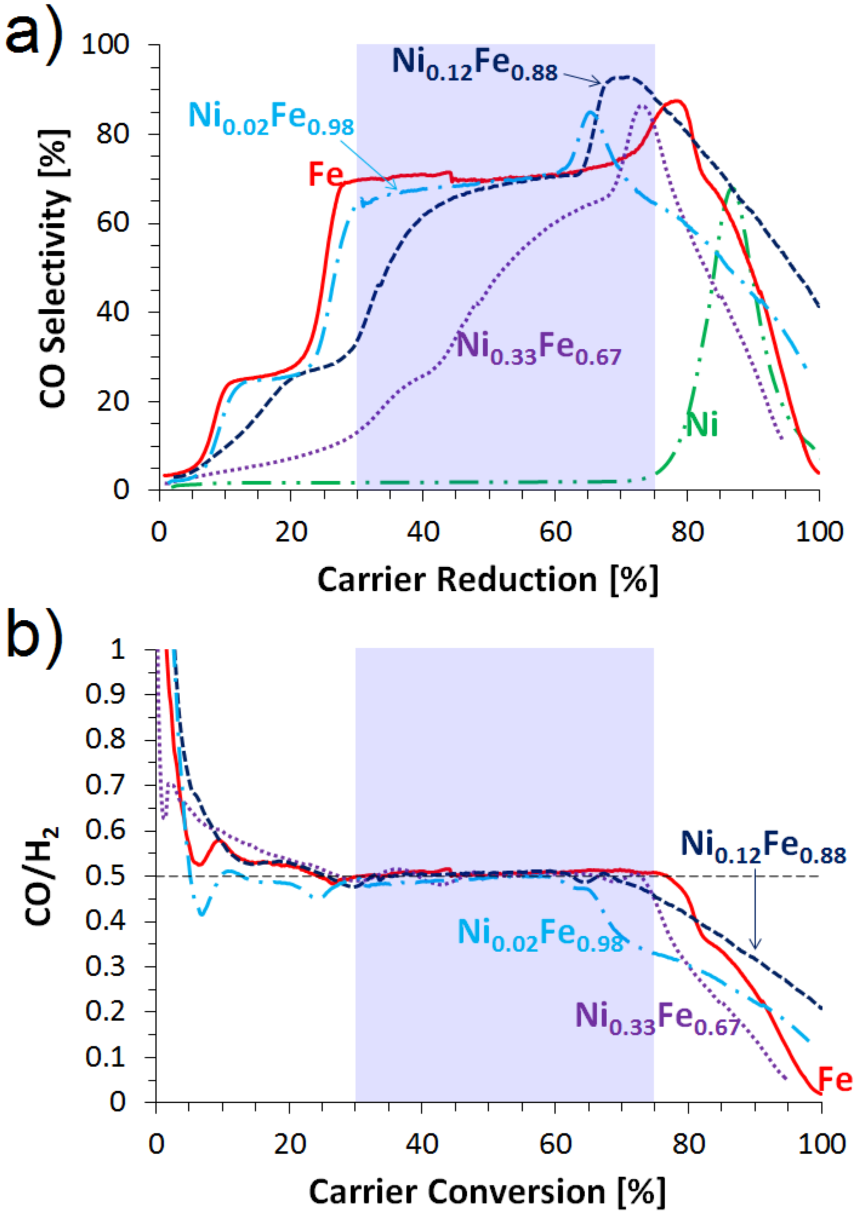

Figure 39. a) CO selectivity and b) CO/H_2 ratio during reduction of Ni_xFe_{1-x}-CeO_2 carriers in a fixed-bed reactor at 900°C using methane (16.7 vol.%, 1sccm). CO selectivity is a strong function of amount of Ni-doping in Ni_xFe_{1-x}-CeO_2 carriers. The shaded box in the graphs shows an approximate optimal window of carrier reduction (30 – 75%) that would be necessary in order to achieve good CO selectivity with syngas ratio (CO/H_2) close to 0.5. CO/H_2 curve for Ni-CeO_2 is not shown because it does not show any significant CO selectivity in the range of carrier conversion of interest (30 – 75% carrier reduction).

Figure 39b shows the $CO:H_2$ ratio for Ni_xFe_{1-x}-CeO_2 carriers. For all carriers, the $CO:H_2$ ratio in the beginning of carrier reduction shows values higher than 0.5. But the syngas ratio shown in this case does not have a physical meaning because total oxidation of methane mainly results in formation of CO_2 and steam, while partial oxidation is a secondary reaction (see CO selectivity in Figure 39a). As the carrier reduction of ~30% is approached, all the carriers show significant CO selectivity (Figure 39a) with $CO:H_2$ ratio close to 0.5 (Figure 39b) which is desired in downstream processing of syngas. As the carrier gets reduced, CO selectivity peaks off and carbon formation via methane cracking takes on a dominant role. Consequently, as carrier reduction exceeds ~75%, the $CO:H_2$ ratio drops due to depleting CO concentration and concomitant H_2 formation due to methane pyrolysis.

Hence, to maximize the ability to produce syngas in the reducer with a $CO:H_2$ ratio of 0.5, it is necessary to avoid methane cracking (in the end stages of carrier reduction) as well as CO_2 formation (in the initial stages of reduction). As a result, with Fe-CeO_2 as reference, we chose 30 – 75 % carrier reduction as an optimal window for CLPOM operation. We aimed to compare Ni_xFe_{1-x}-CeO_2 carriers in this carrier reduction window to understand the effect of Ni-doping on CO selectivity and, more importantly, methane conversion – a significant factor in determining the effectiveness of carriers. Specifically, the carrier reduction range of 30 – 75% was chosen because this reduction period was found to be most selective for partial oxidation of methane for Fe-CeO_2 and yielded a syngas ratio that is desirable (refer Figure 38 and Figure 39b).

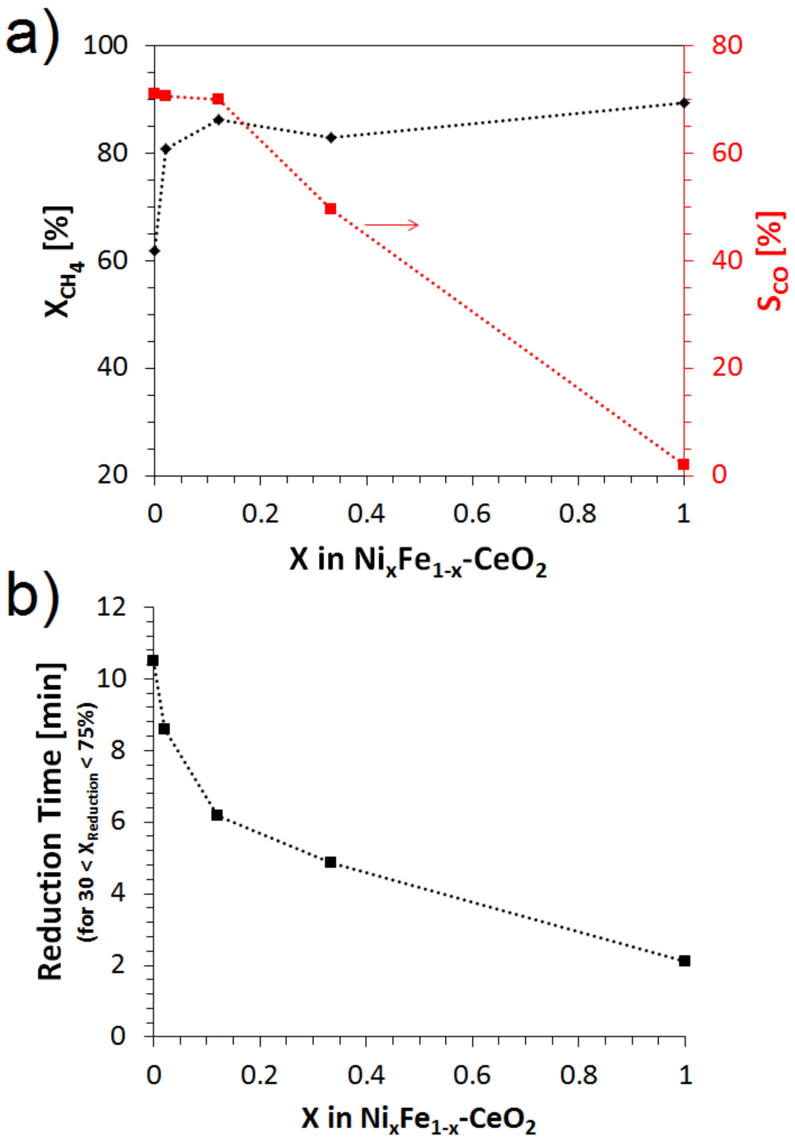

Figure 40. a) Integral methane conversion, CO selectivity and b) reduction time calculated using optimal window of operation for CLPOM (30 < carrier reduction < 75%) during reduction of Ni_xFe_{1-x}-CeO_2 carriers in fixed-bed reactor at 900°C using methane (16.7 vol.%, 1sccm).

Figure 40a determines the effect of doping concentration of nickel (x) in Ni_xFe_{1-x}-CeO_2 on integral methane conversion and integral CO selectivity during carrier reduction range of 30 – 75%. In this range, one can observe that Fe-CeO_2 shows ~70% CO selectivity; however it demonstrates very poor methane conversion ~60%. On the other extreme of the spectrum, Ni-

CeO_2 displays ~90% methane conversion but it is almost exclusively selective for CO_2 formation, yielding less than 5% CO selectivity in the entire reduction range. Although addition of excessive amounts of nickel (e.g. $Ni_{0.33}Fe_{0.67}$-CeO_2) drops CO selectivity, moderate doping concentrations of nickel are favorable for partial oxidation. It can be seen that just 1 wt.% Ni doping in the Fe-based carriers results in a strong enhancement in methane conversion. An increase in the doping concentration of nickel (e.g. 5wt.% Ni in $Ni_{0.12}Fe_{0.88}$-CeO_2) further increases the activity. More importantly, upon comparison of these carriers in the reduction zone favorable for partial oxidation, it is evident that small amounts of Ni doping actually results in a strong enhancement in methane conversion activity without compromising the CO selectivity. We believe that such improved reactivity of carriers is due to the presence of catalytically active and well dispersed nickel in the iron oxide. The homogeneous dispersion of nickel was confirmed in EELS analysis (refer Figure 36). In the catalysis community, nickel is well-known for its ability in activating methane[123, 135]. Therefore, we hypothesize that the presence of highly reactive centers like nickel surrounded by iron oxides could act as catalytically active centers for methane activation. Once the molecule of methane is activated over the nickel centers, the surrounding iron oxide can act as a source of oxygen for further oxidizing it into CO and H_2. Presently, there is no evidence to back the hypothesis, however findings with Ni-rich carriers show that exposure of methane to a large concentration of nickel oxides favors CO_2 formation over CO, as a result of which CO selectivity drops precipitously. This observation aligns well with the excellent behavior of nickel oxides in converting methane to CO_2 and steam. Therefore, using our findings we hypothesize that, as nickel concentration is increased above a threshold limit, one would expect a switch from a dispersed to a separate phase of nickel. Such dispersed nickel species could assists in activating methane for syngas generation; on the other hand, separate nickel oxide islands would not only activate nickel but also over-oxidize the carbonaceous species to form total oxidation products.

The increased activity of oxygen carrier upon nickel doping is also illustrated in Figure 40b which shows the on-stream time taken for reducing carriers from 30 – 75%. It is evident that nickel is far superior in reactivity compared to pure iron, but doping small amounts of Ni onto iron dramatically reduces the reduction time. For example, reducing $Ni_{0.12}Fe_{0.88}$-CeO_2 compared to Fe-CeO_2 takes ~40% less time. Thus, nickel doping not only augments the methane conversion while limiting the use of toxic and expensive nickel, but it also increases the rate of the reduction reaction – a factor that can strongly influence the solid inventory and/or circulation rates in the looping process.

Upon testing the effectiveness of Ni_xFe_{1-x}-CeO_2 carriers in extended methane reduction, it was evident that there is a need to define a redox operation zone ($30 < \text{carrier reduction} < 75\%$) that should be used to maximize the methane conversion to syngas. Further integral analysis with respect to CO selectivity and methane conversion suggested that $Ni_{0.12}Fe_{0.88}$-CeO_2 is a good candidate for partial oxidation of methane. In the aforementioned experiments, $Ni_{0.12}Fe_{0.88}$-CeO_2 demonstrated the highest methane conversion with sustained high selectivity for partial oxidation. Therefore, in the next step of the study, $Ni_{0.12}Fe_{0.88}$-CeO_2 is chosen to test for cyclic redox operation of CLPOM in a fixed-bed reactor, where the carrier would be partially reduced and subsequently partially re-oxidized.

5.2.2 Multi-cycle CLPOM operation in fixed-bed reactor

During cyclic operation, to avoid methane cracking and subsequent carbon carryover in oxidation, reduction half cycles were terminated once the CO concentration peaked through a maximum. During oxidation, cycle times were reduced (in initial cycles) to abate CO_2 formation in the succeeding reduction half process. As a result of such operation, initial cycles were transient in nature (not shown) where reduction and oxidation times were adjusted to maintain CO formation and progressively minimize CO_2 formation. However, redox operation reached a steady state in about 8 – 10 cycles with a reduction time of 6.5 min and an oxidation duration of 2.5 min.

Figure 41 shows twelve representative cycles for the cyclic reduction and oxidation of $Ni_{0.12}Fe_{0.88}$-CeO_2 at 900^oC with methane and 20% O_2 in He, respectively (Figure 41a), as well as the concentration traces for one reduction (Figure 41b) and oxidation half cycle (Figure 41c). One can see that the carrier shows stable operation with no changes in height or shape of the concentration traces with time within error. This confirms the stability of the oxygen carriers in the timeframe of the experiments.

From Figure 41b, it can be seen that during reduction, completely circumventing the CO_2 formation is not possible. Unconverted methane is also mainly observed in the beginning of the cycle. However, unlike in the extended reduction runs where the carrier was completely re-oxidized, H_2 and CO are formed with high concentration right from the on-set of the reduction half process. The reduction half process was stopped once the CO concentration peaked through a maximum to avoid carbon deposition on the partially reduced carriers. During re-oxidation (Figure 41c), a small amount of carbon is burnt-off which is seen in the form of CO and CO_2. The amount of carbon formed was accounted to be ~3% of the carbon fed during reduction.

Further optimizing the experimental set-up and operation scheme can be useful for completely eliminating carbon formation, albeit it was not the focus of the current study. Moreover, the absence of oxygen break-through indicates the intended incomplete re-oxidation of the oxygen carrier to avoid excessive CO_2 formation in the following reduction half cycle.

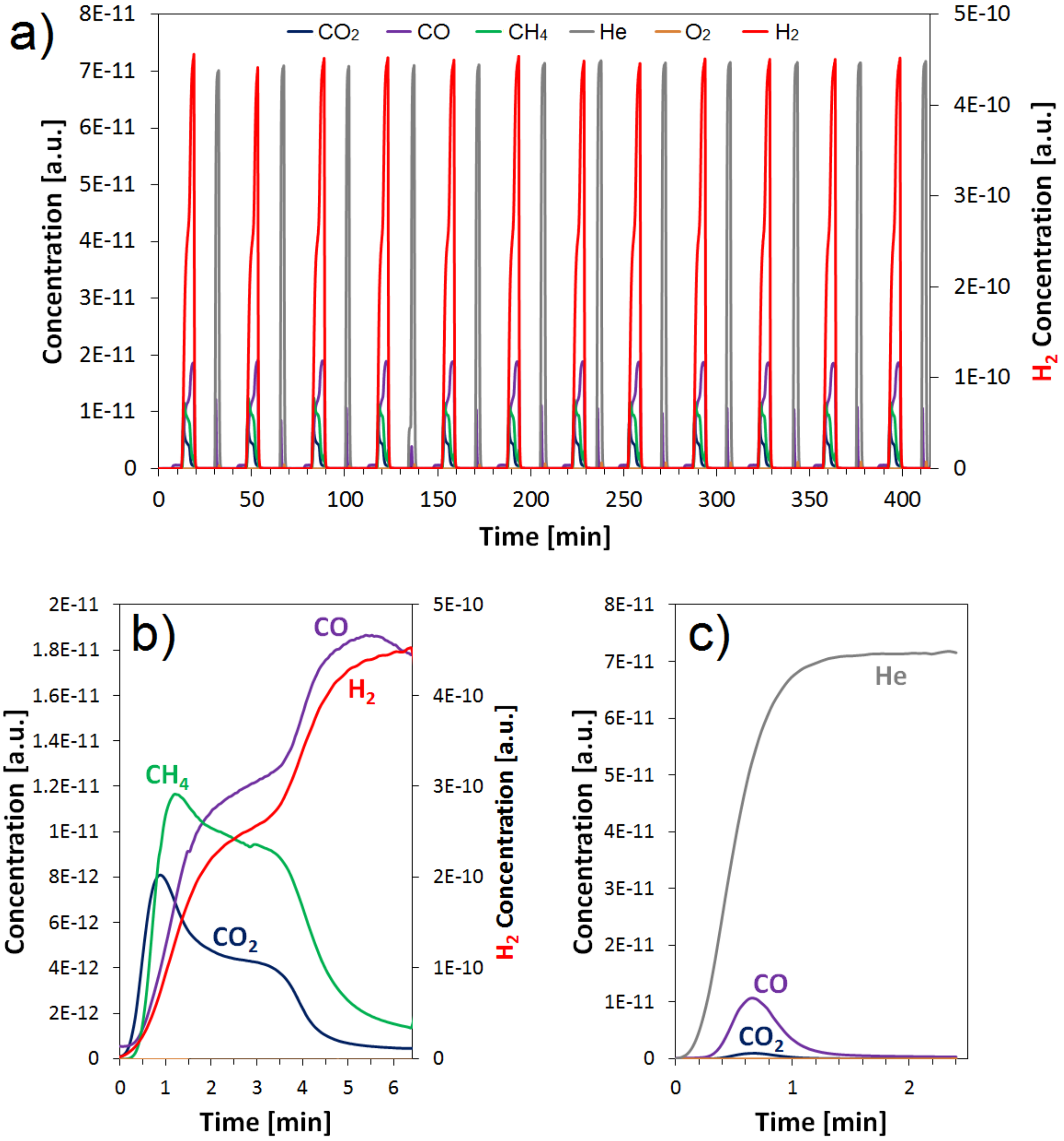

Figure 41. (a) Multi-cycle CLPOM operation of $Ni_{0.12}Fe_{0.88}$-CeO_2 at 900°C with (b) reduction in methane (16.7 vol.%, 1sccm) and (c) re-oxidation of carriers in 20% O_2 in He (10 sccm) during a single redox cycle.

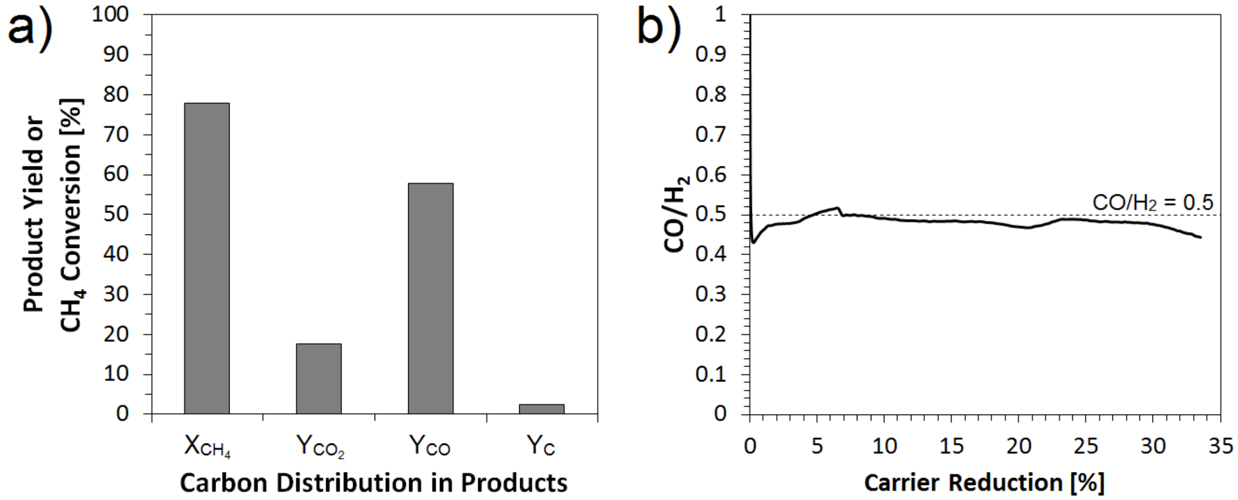

Figure 42. a) Methane conversion and product yield; b) syngas ratio (CO/H_2) during a reduction half cycle from multi-cycle CLPOM operation of $Ni_{0.12}Fe_{0.88}$-CeO_2 at 900°C.

Figure 42a shows the overall methane conversion during the entire reduction half cycle with distribution of carbon between CO_2, CO and carbon products. It can be seen that ~78% of methane fed during reduction half cycle was converted. CO was formed with ~58% yield while ~18% of carbon was in the form of CO_2. Figure 42b shows the syngas ratio ($CO:H_2$) in the entire reduction half cycle. Due to partial re-oxidation of carriers, syngas is formed from the on-set of reduction with a ratio of $CO:H_2$ ~0.5; albeit, CO_2 formation cannot be suppressed completely.

From the point-of-view of using Fe-based materials for CLPOM, one would like to shuttle oxygen carriers between FeO ⇔ FeO_{1-x} (refer section 5.2.1). Hence, it is noteworthy to mention that Fe_2O_3 is known to undergo sequential reduction and form products in the order of Fe_3O_4, FeO and Fe; however re-oxidation of metallic iron is not a set of steps in series[122]. As a result, eliminating carbon formation on reduced or partially reduced carriers is relatively an easy task and can be done with good control, albeit effectively limiting carrier re-oxidation to FeO is difficult and would need more work. On the other hand, formation of any Fe_2O_3 during re-oxidation is detrimental, as it will mainly facilitate total oxidation of methane[122]. This can be a possible cause for CO_2 formation in our experiments. Although issues like further improving the methane conversion and making the process exclusively selective towards partial oxidation needs more work, the present study nevertheless shows that chemical looping offers a good opportunity for tuning the reducer operation to generate syngas – a valuable feedstock in the chemical industry. Moreover, the present work also underscores the importance of using engineered oxygen carriers for selectively driving the system towards desired products.

5.2.3 Fixed-bed reactor calculations

In the chemical looping community, a circulating fluidized bed (CFB) is thought to be the most viable reactor configuration. However, operation of fluidized beds is also associated with issues like attrition, effective solid transport and gas leakage. Alternatively, CLC operation in a fixed-bed reactor (FBR) has been proposed, but heat management has been the critical issue with FBR due to excessive temperatures and formation of hot spots[136]. Unlike in the case of CLC, limiting the over-oxidation of carriers in CLPOM as well as altered gas/solid ratio (due to stoichiometry) in partial oxidation can have significant impacts on associated the exothermicity. These factors may, therefore, result in a strong reduction in the maximum temperature attained in FBR. A rise in fixed-bed temperature is a strong function of heat of reaction and also the capacity of the bed material to retain the heat (which is, in turn, dependent on gas/solid ratio). On the other hand, cyclic operation of partial oxidation in FBR provides an opportunity to effectively heat integrate the typically exothermic oxidizer and endothermic reducer in looping processes. In fact, cyclic operation of fixed-bed reactors in a reverse flow manner for mildly exothermic catalytic partial oxidation has been shown to be highly efficient in achieving excellent heat-integration during autothermal operation[137-140]. Therefore, as a last step in the current investigation, a fixed-bed reactor model was used and analyzed in order to evaluate the feasibility to conduct CLPOM in a periodically operated FBR. The current analysis, however, is limited to a periodically operated fixed-bed configuration with concurrent feed of methane as fuel and air as an oxidizing gas.

This exercise is based on a model using dynamic analysis of the pseudohomogeneous energy balance for a fixed-bed reactor, which was previously published by Kuipers and co-workers for conventional CLC[136] and later adapted by our group for chemical looping steam[75] and dry reforming[84] processes. The primary aim of the model published by Noorman et al.[136] is to determine the temperature excursion in the fixed-bed reactor using the energy balance, which can be solved analytically if a number of simplifying assumptions are made. It is assumed that the carrier in the bed is in the completely reduced state, and, until complete conversion is attained, it reacts instantaneously with air, i.e. with infinitely fast reaction rate. Similarly, instantaneous and complete reaction is assumed with methane during reduction. Although neither of the assumptions, i.e. infinite reaction rates and complete conversion, is completely true in our case (as seen in section 5.2.2), the analysis based on these assumptions will yield a conservative estimate for the expected maximum temperature rise in fixed-bed.

Coupling of the gas-solid reaction and convective gas flow yields two spatially separated travelling wave fronts which move through the reactor bed with different velocities: The velocity of the heat front (v_h), where heat is transferred from the fixed bed to the gas phase, and the velocity of the reaction front (v_r), where all the oxygen fed in the form of air reacts with the oxygen carrier:

$$v_h = \frac{\rho_g v_g C_{P,g}}{\varepsilon_s \rho_s C_{P,s}} \qquad \text{… Eq. (8)}$$

and

$$v_r = \frac{\rho_g v_g w_{g,O_2}^{in} M_{act}}{\varepsilon_s \rho_s w_{act} M_{O_2} \xi} \qquad \text{… Eq. (9)}$$

(Please refer to the Nomenclature section for variable meanings). It is assumed that the heat capacities of the gas and the solid ($C_{P,g}$ and $C_{P,s}$) and the solid density (ρ_S) are constant, and that the influence of pressure drop over the fixed bed and the variation of the mass flow rate can be neglected. Since the heat of reaction (ΔH_R) and specific heat capacity of the reactants ($C_{P,g}$) are only weakly dependent on temperature over the temperature range of interest, average values for ΔH_R and $C_{P,g}$ were utilized, and the calculations are not dependent on a specific reference temperature.

Assuming furthermore that the gas phase volumetric heat capacity is negligible, the heat produced by the oxidation of the oxygen carrier is taken up entirely by the solid carrier, and the energy balance can be written as

$$\frac{\rho_g v_g w_{g,O_2}^{in}}{M_{O_2}}\left(-\Delta H_R\right) = \varepsilon_s \rho_s C_{P,s}\left(v_r - v_h\right)\left(T_{\max} - T_0\right) \qquad \text{… Eq. (10)}$$

Substituting equations (11) and (12) in (13) and rearranging gives the maximum temperature rise in the bed:

$$\Delta T_{\max} = \left(T_{\max} - T_0\right) = \frac{-\Delta H_R}{\dfrac{C_{P,s} M_{act}}{w_{act}\xi} - \dfrac{C_{P,g} M_{O_2}}{w_{g,O_2}^{in}}} \qquad \text{… Eq. (11)}$$

As already pointed out by Noormal et al., under the given assumptions, maximum temperature rise is independent of the gas velocity[136]. The above observation indicates that fixed-bed reactors should be robust against the changes in the production capacity. The decoupling of maximum temperature rise in fixed-bed reactors from gas flow is due to the assumption that the heat capacity of the gas phase is small in comparison to the solid phase, which results in negligible convective heat transport with the gas flow. The assumption can be expected to be broadly applicable due to the large difference in the volumetric heat capacities between solids and gases. Furthermore, Eq. (11) is independent of reaction rate due to the assumption of infinitely fast reaction rates. Noorman et al. validated the robustness of their model for CLC of methane: It was observed that as long as the rates were sufficiently fast, their analytical solution showed little sensitivity to changes in the reaction rate coefficients (even for changes by a factor of as much as 7). In our case, non-instantaneous reactions and incomplete conversion can result in temperature increase which would be of a lesser magnitude than what is observed in this analysis.

While previous analyses had focused on the use of different metals, to continue with the theme of partial oxidation, here we focus on the use of different oxidation states of a single metal (Fe) for total or partial oxidation of methane. For pure Fe carriers, in principle CLC can be performed by utilizing the transitions between various oxidation states of iron, for example, $Fe_2O_3 \Leftrightarrow Fe_3O_4$ or $Fe_2O_3 \Leftrightarrow Fe$, etc. From section 5.2.1.1 we observed that the $FeO \Leftrightarrow Fe$ transition is selective for partial oxidation. Thus, the aim of the present analysis is to investigate three different cases with the objective to understand how utilization of different oxidation states affects the maximum temperatures to be expected in chemical looping combustion or partial oxidation operation with Fe-based carriers. The three cases specifically are i) $FeO \Leftrightarrow Fe$ for partial oxidation, ii) $Fe_2O_3 \Leftrightarrow Fe_3O_4$ for total oxidation and iii) $Fe_2O_3 \Leftrightarrow Fe$ for total oxidation. Here, we utilize Eq. (11) to compare the fixed-bed temperature rise for the abovementioned cases, where oxygen available for oxidation of one mole of methane is supplied via the transition between different oxidation states of iron. Redox reactions, gas/solid ratio and heat of reactions for the three cases considered in this analysis are summarized in Table 7.

Table 7. Table summarizing redox reactions, gas/solid ratio and heat of reaction for the three different cases considered for comparison in pseudohomogeneous model to compute the maximum temperature excursion in fixed-ned reactor. (Where, P.O.: Partial oxidation of methane, T.O.: Total oxidation of methane)

Case	Reaction	Gas/solid ratio	Heat of reaction (kJ/mol, at 900^{o}C)
$FeO \Leftrightarrow Fe$ (P.O.)	$Fe + \frac{1}{2} O_2 \rightarrow FeO$	0.5	-270.5
	$FeO + CH_4 \rightarrow Fe + 2 H_2 + CO$	1	248.6
$Fe_2O_3 \Leftrightarrow Fe_3O_4$ (T.O.)	$8 Fe_3O_4 + 2 O_2 \rightarrow 12 Fe_2O_3$	0.25	-950.6
	$12 Fe_2O_3 + CH_4 \rightarrow 8 Fe_3O_4 + 2 H_2O + CO_2$	0.083	-149.1
$Fe_2O_3 \Leftrightarrow Fe$ (T.O.)	$8/3 Fe + 2 O_2 \rightarrow 4/3 Fe_2O_3$	0.75	-1079.6
	$4/3 Fe_2O_3 + CH_4 \rightarrow 2 H_2O + CO_2 + 8/3 Fe$	0.75	278.1

Figure 43a shows that the expected temperature rise for partial oxidation is much less than that of total oxidation using $Fe_2O_3 \Leftrightarrow Fe$. This can be explained by the mild exothermicity of the partial oxidation reaction compared to total oxidation along with the relatively smaller gas/solid ratio in the case of total oxidation ($Fe_2O_3 \Leftrightarrow Fe$). Since the temperature rise in FBR is a strong function of heat capacity of bed material, gas/solid ratio (determined by stoichiometry), as well as the heat of reaction, the relatively lesser amount of solids inventory in the bed coupled with the large heat of reaction would mean high bed temperatures when using Fe_2O_3 ⇔ Fe for total oxidation of methane. On the other hand, the mildly exothermic partial oxidation would require comparatively large amounts of solids in FBR which can act as a heat sink in adiabatic operation. Figure 43b shows the overall temperature rise in an ideal scenario of 100% heat integration between endothermic reducer and exothermic oxidizer. It can be seen that FBR operation of the mildly exothermic partial oxidation would not be able to sustain the bed temperature in autothermal operation with less than ~33 wt.% active metal (i.e. Fe) in the oxygen carriers. Moreover, it would be necessary to limit the amount of active metal to 40 – 45% in order to avoid large hot-spots when operating CLPOM in FBR. This observation supports our decision to limit the metal content to 40 wt.% in the present study.

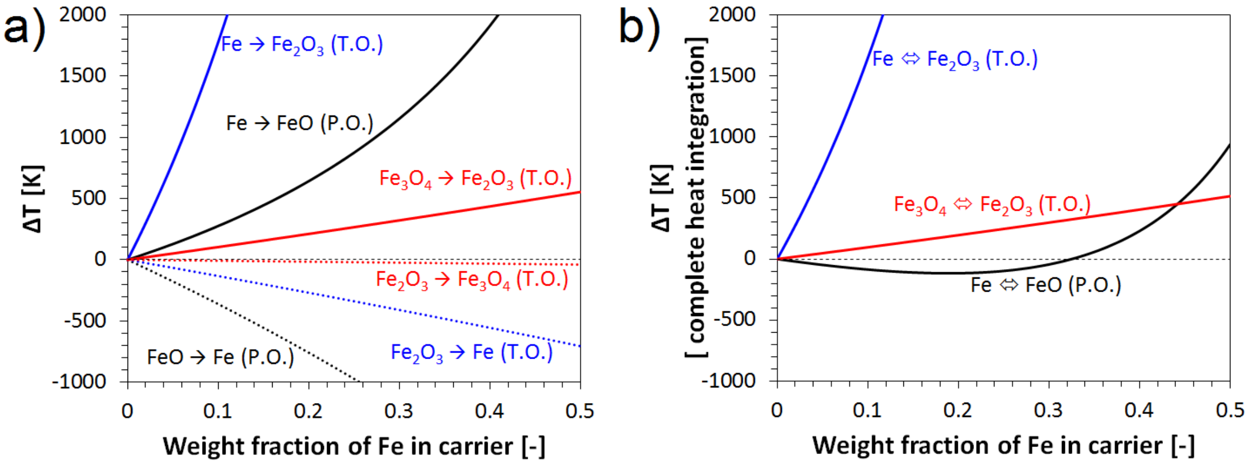

Figure 43. a) Maximum temperature difference during reduction with methane and re-oxidation with air as and b) maximum temperature rise with 100% heat integration between reducer and oxidizer a function of iron loading in the fixed-bed reactor (where P.O.: Partial oxidation and T.O.: Total oxidation of methane).

Upon comparing both the total oxidation cases, it is interesting to note that these strong differences are not due to the heat of oxidation for the two cases; while there is less than a 15% difference in heats of oxidation, the maximum temperatures vary by an order of magnitude.

Rather than heats of oxidation, it is in fact the gas/solid ratio in the system that determines the maximum temperature. This is because the heat balance in the system is strongly determined by the heat capacity of the solid and the difference in the oxygen carrying capacity (based on the transitions between different oxidation states), which results in a strong difference in gas/solid ratio (see Table 7). For example, in the case of $Fe_2O_3 \rightarrow Fe$, much less (9-times less, to be precise) oxygen carrier is required to combust one mole of methane than for the $Fe_2O_3 \rightarrow Fe_3O_4$ case. The presence of a large amount of solid in the latter case results in the retention of a large portion of this heat since temperature increase in the fixed-bed is a strong function of heat capacity of solids, i.e. the solid effectively buffers against an excessive temperature excursion. Thus, operating CLC in a fixed-bed reactor mode is recommended to be limited to the transition between $Fe_2O_3 \Leftrightarrow Fe_3O_4$ in order to control maximum temperatures. Interestingly, this observation correlated well with the literature data which reports the transition from $Fe_2O_3 \rightarrow Fe_3O_4$ being the most favorable for CLC from point-of view of reactivity and CO_2 selectivity[29, 39].

Finally, it should be noted here that the "heat buffering" observed for both partial and total oxidation cases can also be expected to be highly beneficial for an efficient heat integration between the two half cycles in a fixed-bed process. Thus, our simplified thermal analysis demonstrates that fixed-bed operation of CLPOM with CH_4 is a viable option, where severe heat spots can be avoided by controlling the active metal content and oxygen utilization in the carriers.

5.3 SUMMARY

The present study focuses on using the chemical looping principle for syngas production. An abundant supply of natural gas and the possibility of converting methane into valuable chemicals is the primary motivation behind this work. For applying chemical looping for syngas generation, we take a two-pronged approach: We aim to tailor the oxygen carriers by combining the high reactivity of nickel with the selective but less reactive iron oxides. Furthermore, process operation was modified to limit the formation of total oxidation or methane pyrolysis products. To that effect, we reduced the carriers incompletely to avoid the coke formation associated with deeper reduction of metal oxides with methane, and subsequent re-oxidation was cut short to limit the amount of oxygen available for over-oxidation of methane.

Various mixed oxides of Ni_xFe_{1-x}-CeO_2 were synthesized and tested in extended reduction with methane to determine their reactivity and selectivity for partial oxidation. To objectively compare the effect of Ni-doping, iron oxides were taken as reference, and a carrier reduction window was determined (30 – 75 % carrier reduction), which was pre-dominantly selective for syngas generation with H_2:CO ratio ~2. All the Ni_xFe_{1-x}-CeO_2 carriers were compared for overall methane conversion and selectivity for partial oxidation in the above-mentioned reduction zone. Based on the analysis, it was found that the amount of nickel-doping has a significant effect on the carriers' selectivity for partial oxidation. Carriers with nickel in dispersed form were found to be highly active for syngas generation, which we believe is due to the catalytic activity of nickel to effectively activate the methane. However, with increasing amounts of nickel, lattice oxygen associated with it causes the over-oxidation.

From the above analysis, $Ni_{0.12}Fe_{0.88}$-CeO_2 was determined to be the most effective carrier material and was subsequently tested in a periodically operated fixed-bed reactor for syngas generation. Herein, carriers were only partially reduced and re-oxidized to mimic the operation in the carrier reduction window selective for syngas generation. Upon redox cycling, carriers showed stable operation with 78% methane conversion and 74% CO selectivity with syngas ratio ~2. Avoiding deeper carrier reduction helped in minimizing coke formation (limited to 3% of methane fed).

Finally, a reactor model previously developed by Kuipers and coworkers and later modified by our group was used to examine the feasibility of conducting partial oxidation with Fe-based carriers in FBR without issues of excessive temperature excursion. Analysis confirmed that hot spot formation could be potentially avoided by limiting the active metal component, i.e., metal in carrier material and carrier utilization.

Overall, the present study demonstrates that appropriate carrier selection and limiting carrier reduction/oxidation can be combined to form syngas using chemical looping in fixed-bed reactors (without the aid of steam co-feed to suppress carbon deposition). Although issues like eliminating unconverted methane and total oxidation warrant further investigation, chemical looping partial oxidation of methane is a safe and viable alternative to its catalytic counterpart, and CLPOM does not require an expensive noble metal catalyst and/or air separation.

6.0 CHEMICAL LOOPING DRY REFORMING AS NOVEL AND INTENSIFIED PROCESS FOR CARBON DIOXIDE ACTIVATION

The CLC principle can generally be applied to any combination of fuel and oxidizer (provided that the carrier shows sufficient reactivity towards both), opening the way for various intensified processes relevant to clean energy technology. For example, by replacing air with steam as oxidant, the process results in the production of ultra-pure H_2 in the oxidizer effluent, avoiding the need for additional gas separation and purification steps[73, 75, 141]. Similarly, this concept can be extended to CO_2 utilization by replacing air with CO_2 as the oxidant and reducing the carrier either by concentrated solar energy or by a conventional chemical fuel[84, 87, 142]. In the latter case, the reduction reaction remains unchanged when compared to "conventional" CLC, but by using CO_2 as oxidant concentrated CO streams are produced in the oxidizer, thus activating CO_2 and overcoming the main barrier for CO_2 utilization. Along the same lines, using mixed feed of steam and CO_2 as oxidizing gases would result in formation of syngas in oxidizer effluent.

Although CLDR is an attractive, intensified, and fuel-flexible alternative to conventional dry reforming, challenges are expected with regard to the stability of oxygen carriers at extended high-temperature cyclic operation, mechanical stability against attrition during solids circulation in the circulating fluidized bed configuration (typically envisioned for CL processes), and the possibility of carbon formation during oxidation with CO_2. Additionally, in comparison to the CLC process, slower oxidation kinetics using CO_2 in place of oxygen (air) need to be overcome.

Previous work in our laboratory have identified iron as the most suitable metal for chemical looping reforming processes[75, 84]. Specifically for CLDR, an optimal temperature window of ~600–800^{o}C, which allows suppression of coke formation (thermodynamically favored at lower temperatures) while utilizing the oxidation potential of Fe_3O_4 (which becomes unstable at higher temperatures). In the present study, we compared two different Fe-based carriers for CLDR: Alumina and silica-based nanostructured oxygen carriers were synthesized and their activity and stability was evaluated in thermogravimetric analysis (TGA) and fixed bed reactor studies. Finally, a CLDR process scheme with a two-step oxidation is proposed which addresses carrier deactivation for silica-based carriers while, more importantly, resulting in a net exothermic CLDR process.

6.1 EXPERIMENTAL

6.1.1 Carrier synthesis and characterization

Due to the expected slower oxidation kinetics with CO_2 instead of air as oxidant, we aimed to maximize the reactivity of the carrier through the use of nano-sized Fe particles. While smaller particles can be expected to be more reactive due to minimization of solid state diffusion limitations during formation of dense oxide over-layers during carrier oxidation[143], nano-scale particles also require efficient particle stabilization for high-temperature operation[144]. For this purpose, we synthesized and compared two different carriers, in which particle stabilization was targeted in two different ways: As a first carrier type, Fe nanoparticles were embedded in a porous, high-temperature stabilized alumina matrix (BHA = Barium Hexaaluminate) to form Fe-

BHA nanocomposite carriers, and as second carrier Fe@SiO_2 core-shell materials were prepared via encapsulation of Fe nanoparticles in porous silica shells. Synthesis and characterization of these carriers is briefly described below.

6.1.1.1 Fe-BHA

Fe-BHA is synthesized in a simple, one-pot reverse-microemulsion templated sol-gel synthesis, previously developed in our laboratory[145-146]. Briefly, a reverse microemulsion is prepared by mixing an aqueous solution of $Fe(NO_3)_3$ with iso-octane and a surfactant (poly(ethylene oxide) – poly(propylene oxide) block copolymer with 1-pentanol as co-surfactant). Aluminum and barium isopropoxides are dissolved in isopropanol at a stoichiometric ratio (1:12) for formation of barium hexaaluminate[147-148], and added to the oil phase of the microemulsion, where they diffuse into the aqueous phase (micelles) and undergo hydrolysis and condensation. In parallel, the iron salt is reduced to metal nanoparticles, which are embedded in the oxide matrix[145]. After aging and phase separation, products are washed several times with acetone, freeze-dried, and calcined at 500°C for 2 h in air flow to obtain the final powder form of the carrier. Refer Table 8 in appendix for synthesis details.

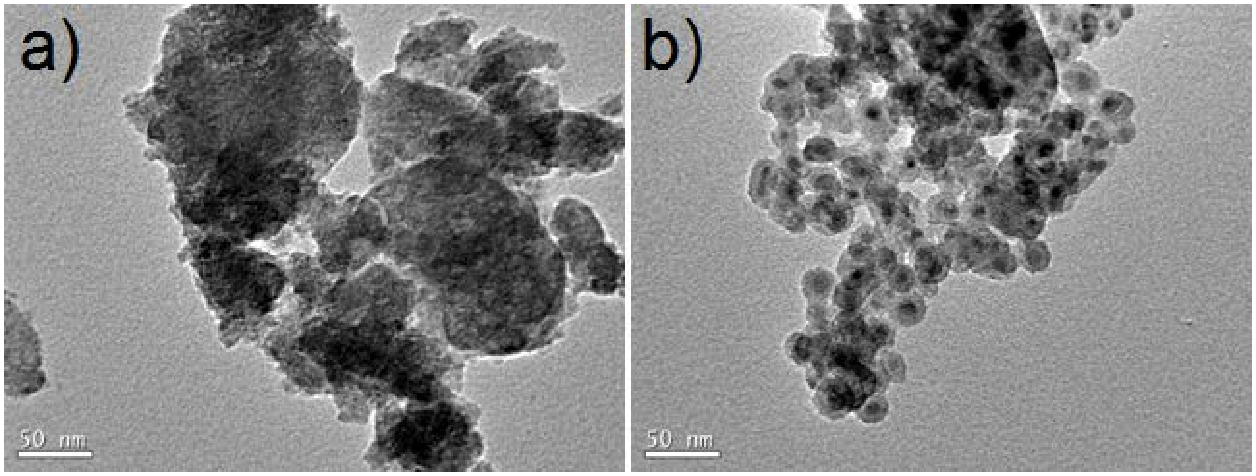

Figure 44. Typical TEM image of oxygen carriers calcined at 500°C: (a) Fe-BHA, (b) Fe@SiO_2.

The as-obtained nanocomposite material is characterized using XRD, BET (Micromeritics ASAP 2020), and TEM (JEOL 200). A typical TEM image is shown in the Figure 44a, where the gray matrix represents the BHA support matrix and iron is shown in black, found in cluster form. The BET surface area after calcination at 500^{o}C is ~225 m^2/g, with highly interconnected pores with average pore sizes around ~8 nm allowing facile access of reactant gases to the embedded nanoparticles. The weight loading of the Fe-BHA is determined to be ~37 wt.% Fe by monitoring the weight loss and gain upon reduction (H_2) and oxidation (air) in CLC cycles at 800^{o}C, is in good agreement with the nominal 40 wt.% Fe loading targeted in the synthesis.

6.1.1.2 Fe@SiO$_2$

As alternate way to suppress high-temperature agglomeration of Fe nanoparticles, a Fe@SiO$_2$ core-shell configuration was synthesized[144, 149]. The synthesis is also based on a reverse-microemulsion in which Fe nanoparticles are first formed and then coated with silica in a second step. Briefly, the microemulsion is prepared from an aqueous solution of $Fe(NO_3)_3$, cyclohexane, and Brij58 as surfactant. Hydrazine hydrate is then added as reducing agent to form Fe nanoparticles, the pH is adjusted to ~9 via addition of ammonium hydroxide, before tetraethyl orthosilicate (TEOS) is added as silica precursor. TEOS is catalytically hydrolyzed to form a porous silica over-layer via a modified Stöber method[150]. After aging, phase separation, and several isopropanol wash, the powder is dried in air overnight and calcined at 500^{o}C in air flow for 2 h to obtain the final form of the carrier.

The calcined Fe@SiO$_2$ is similarly characterized by XRD, BET, and TEM. Figure 44b shows a typical TEM image of the material after calcination, where the Fe nanoparticle cores are dark and the silica shell appears as grey over-layer. The specific surface area of Fe@SiO$_2$ is

~133 m^2/g, with silica pore size of ~0.7 nm. Exposing the material to H_2 at 500°C for 1 h shows the formation of metallic Fe cores in XRD and thus confirms the accessibility of the cores to reactive gases. The weight loading of the sample is determined by EDAX (Philips XL 30) analysis to be ~ 27 wt.% Fe.

6.1.2 Reactive tests

In the present studies, which are focused on understanding the behavior of the carriers in the oxidation half cycle with CO_2, H_2 is used as model fuel to avoid complications of competitive partial versus total oxidation of CH_4 or other hydrocarbon fuels. Thus, the overall net reaction yields the reverse water gas shift reaction ($CO_2 + H_2 = CO + H_2O$). Oxidation and reduction of the carrier is monitored first in TGA, followed by reactivity and stability tests in a fixed-bed reactor configuration.

The carriers were tested in TGA (Perkin Elmer TGA7) experiments with regard to carrier utilization, i.e. the oxidation states of the carriers attained during oxidation and reduction, which can be inferred in a straightforward way from the observable weight changes. 4-7 mg of the respective carriers were reduced in H_2 (20 sccm, grade 5.0) and re-oxidized in CO_2 (20 sccm, 99.999%**)** with a N_2 (20 sccm, grade 5.0) purge separating the two phases. (Due to changes in the gas flow rates during the oxidation, reduction, and purge phases, the time traces show small off-sets during switching of the gases.)

Fixed-bed reactor studies were conducted to investigate carrier conversion, temperature dependence of the kinetics, and the stability of the carriers in multiple redox cycles. For this purpose, 50 mg of Fe-BHA or 74 mg Fe@SiO_2, respectively, were placed inside an externally heated quartz-glass tube (1/4” I. D.) resulting in identical amounts of metallic Fe, i.e. active carrier component for both cases. The assembly was first heated in an inert gas stream (Ar, grade 5.0) to the desired reaction temperature, and then H_2 (5 vol. % in Ar, 5 sccm) and CO_2 (20 vol. % in Ar, 20 sccm) were flown alternating to simulate the periodic redox operation characteristic for CLDR. In experiments, the reactor was purged with Ar between the oxidation and reduction half cycles. While this is not necessary in CLDR (unlike for CLC, where the purge phase is required to avoid the formation of potentially explosive gas mixtures during gas switching), this purge allows a clear differentiation between the products of oxidation and reduction phases and hence facilitates evaluation of the experiment. The duration of the reduction and oxidation half cycles was 10 min. in all experiments, with a 15 min. purge phase. These times were chosen based on break-through curves during reduction and oxidation, and to assure complete purge of reactive gases between the redox half-cycles, respectively. The product gas concentrations, of reactor effluent, during each half cycle were monitored via mass spectrometry (Pfeiffer Omnistar QMS 200).

6.2 RESULTS AND DISCUSSION

6.2.1 Reactive tests in TGA

Figure 45a shows four redox cycles of Fe-BHA at 600^{o}C, with calculated sample weights for different oxidation states of iron shown by dotted lines. During reduction, complete conversion to metallic Fe is achieved, with a fast reduction from Fe_2O_3 to Fe_3O_4 in the first cycle, followed by a relatively slow reduction to Fe, as reported before for CLC processes[14]. Interestingly, no distinct steps representing the reduction from Fe_3O_4 to FeO and FeO to Fe can be observed in the time traces. During oxidation with CO_2, the sample is very rapidly oxidized within ~2-3 min. to a sample weight in close agreement with the calculated weight for Fe_3O_4 (the ~1-2% deviation from the expected sample weight is well within experimental error). Formation of the Fe_3O_4 phase is confirmed via XRD analysis of the sample after the final oxidation half cycle, with no indication of the presence of other Fe_xO_y phases.

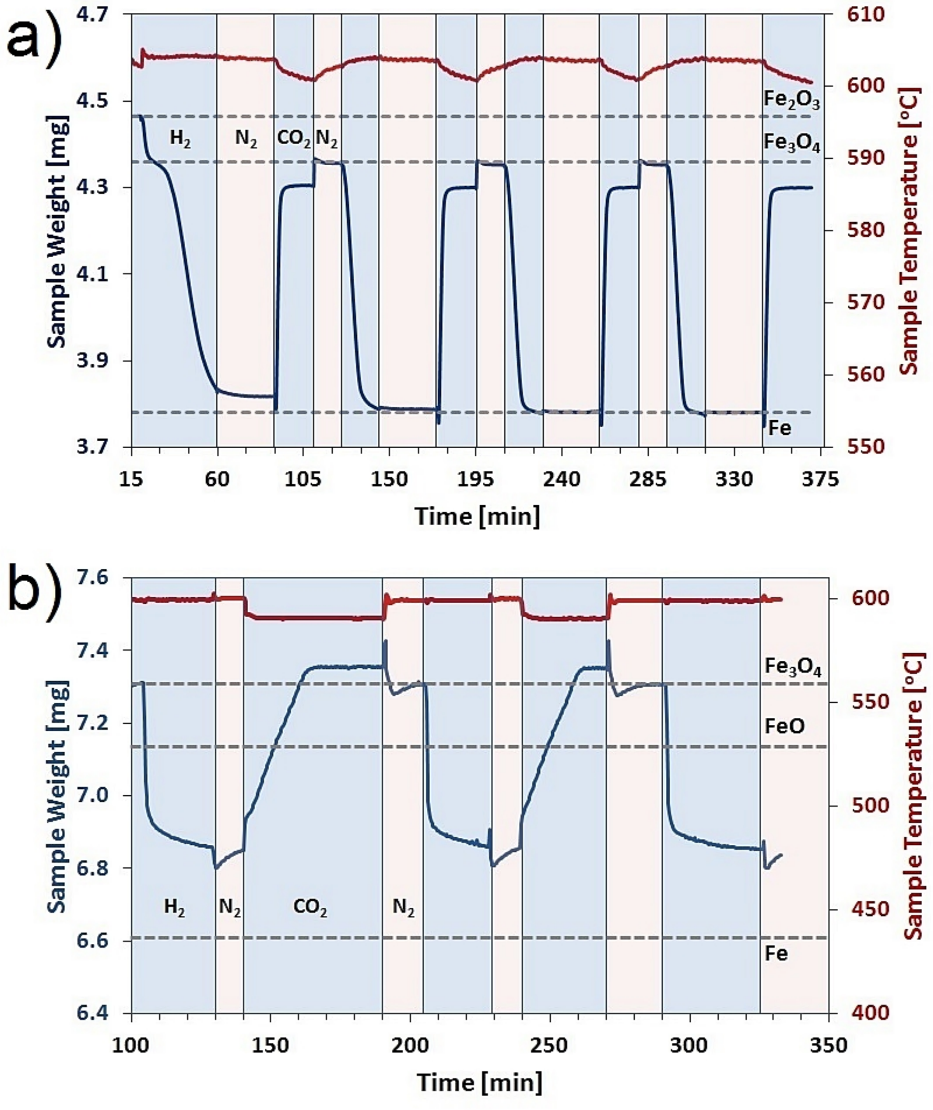

Figure 45. Operation of CLDR in TGA (reduction in H_2, N_2 purge, and oxidation with CO_2) at 600°C with (a) Fe-BHA for four redox cycles, and (b) Fe@SiO_2 for two redox cycles.

Figure 45b shows evaluation of the Fe@SiO_2 carrier in TGA experiments at 600°C, with dotted lines again indicating calculated sample weights for different oxidation states of Fe. A distinctly different behavior of the carrier in comparison to Fe-BHA is observed: The carrier shows fast initial reduction from its initial oxidation state (Fe_3O_4), followed by a very slow reduction process (over ~30 min, after which the TGA is switched to the purge phase). The final reduced weight does not correspond to either pure FeO or Fe, indicating incomplete conversion of the carrier and formation of a Fe/FeO mixture during this step. During oxidation with CO_2, one observes a very slow oxidation process over ~20-25 min, proceeding at a constant rate of oxidation. Again the process is much slower than that observed for Fe-BHA.

The TGA studies thus establish the basic feasibility of a CLDR process, although the limited conversion of the Fe@SiO_2 casts doubt on its suitability for the proposed purpose. However, due to the contacting pattern between gas phase and solid carrier, TGA studies are not well suited to evaluate the conversion of the gas phase reactants. Therefore, both carriers were further evaluated in fixed-bed reactor studies.

6.2.2 Reactive tests in fixed-bed reactor

Figure 46a shows eleven redox cycles for a fixed bed of Fe-BHA at the maximum experimental temperature of 800°C, as determined by thermodynamic prediction[84]. The reproducibility of the alternating patterns of the breakthrough of H_2 during reduction of the carrier and appearance of CO and unconverted CO_2 during oxidation indicates stable operation of the carrier (i.e. there were no significant changes in the height or shape of the concentration traces with time within experimental error). The experiments were reproduced several times and conducted at several different temperatures (300 – 800°C) without changing the carrier bed, and no signs of deactivation were discernible over the entire set of experiments. The fixed-bed reactor studies thus confirm the stability of the Fe-BHA at least over the scale of many hours, including frequent shutdown and start-ups.

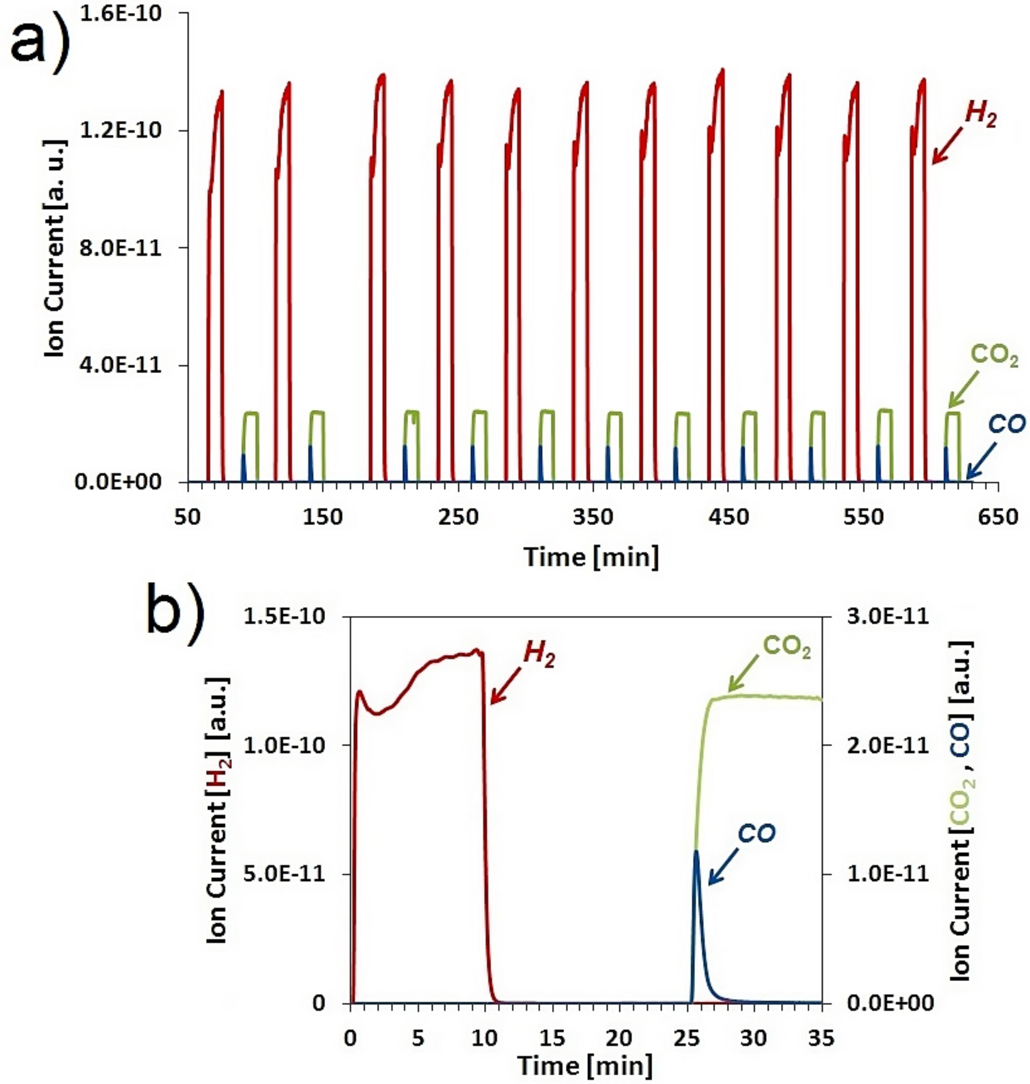

Figure 46. (a) Multiple redox cycles in fixed-bed CLDR operation with Fe-BHA at 800°C, using CO_2 (20% CO_2 in Ar) as oxidant and H_2 (5% H_2 in Ar) as model fuel; (b) Enlarged single cycle.

Figure 46b shows an enlarged view of a single cycle for CLDR operation with Fe-BHA. During the reduction half cycle, H_2 is initially consumed with breakthrough occurring after ~4 minutes (the initial overshoot of H_2 visible in the graph is due to residual backpressure in the H_2 line in the experimental setup). During the oxidation half cycle, a pronounced CO peak is observed as soon as the CO_2 flow is initiated, indicating very fast CO_2 reduction. This strong peak falls off over a few minutes, after which complete CO_2 break-through is observed again. Clearly, complete CO_2 conversion is not achieved—even during the fast initial oxidation—in agreement with predicted thermodynamic limitations for CO_2 conversion[84].

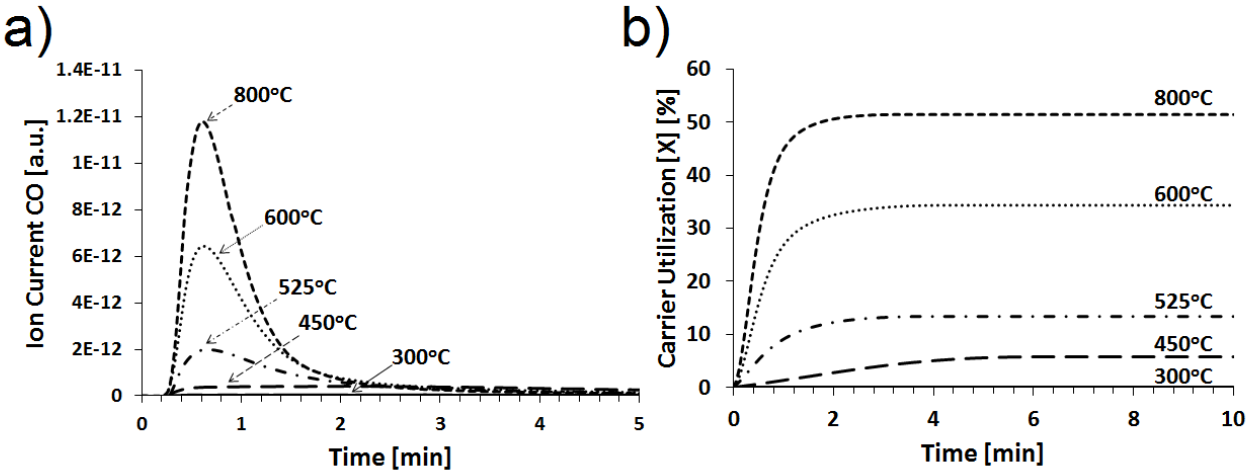

Figure 47. (a) CO generation over one oxidation half cycle at different temperatures using Fe-BHA; (b) Fe-BHA carrier conversion as a function of time over one oxidation half-cycle at different temperatures.

The carrier oxidation kinetics is strongly temperature dependent as shown in Figure 47a where the CO concentration trace is shown as a function of time over a temperature range from 300 to 800°C. CO generation starts at T>450°C, and exhibits a fast initial generation followed by a trailing tail. As expected, the initial kinetics accelerates with increasing temperature (i.e. the leading edge of the peak becomes steeper), reflecting a typical Arrhenius dependence of the carrier oxidation kinetics. Interestingly, in addition to the accelerating kinetics, an increase in the total carrier utilization is also observed with increasing temperature as shown in Figure 47b. Maximum carrier utilization is observed at 800°C (~51%), which reduces with a decrease in the operating temperature (to ~34% and 13% at 600^{o}C and 525^{o}C, respectively). This trend agrees again well with the thermodynamically predicted increase in CO yield with increasing temperature[84]. Finally, it should be noted that no C formation was observed at any temperature, i.e. CO_2 conversion was entirely selective to CO within experimental detection limits.

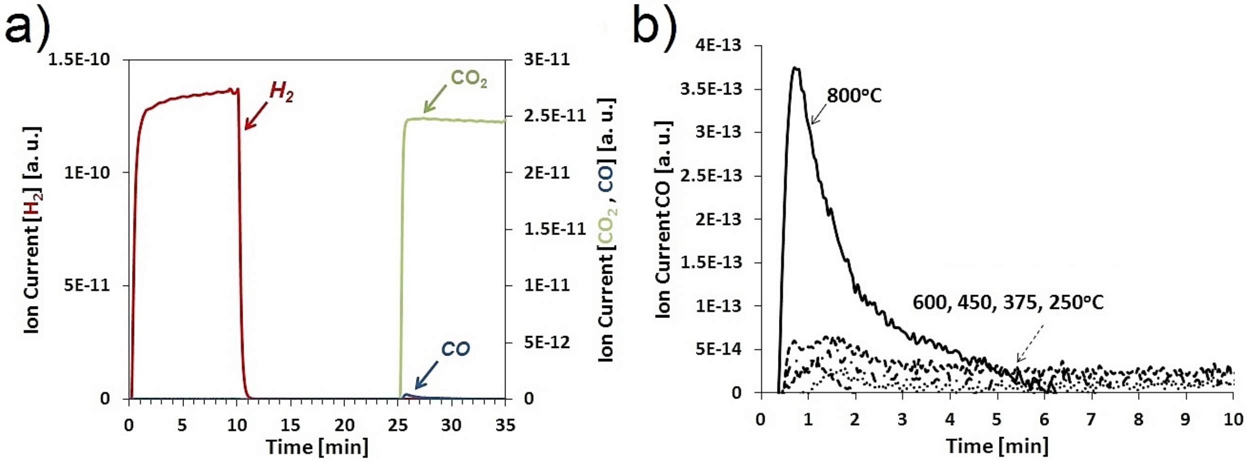

Figure 48. (a) Enlarged single redox cycle in foxed-bed CDLR operation with Fe@SiO_2 at 800^{o}C, using CO_2 (20% CO_2 in Ar) as oxidant and H2 (5% H_2 in Ar) as model fuel. Virtually no CO formation is observed. (b) CO generation in a single oxidation half-cycle at different temperatures using Fe@SiO_2.

Fe@SiO_2 core-shell carriers were tested in the same way as Fe-BHA in fixed-bed reactor experiments. Figure 48a shows an enlarged view of one of multiple redox cycles for Fe@SiO_2 fixed bed operation at 800^{o}C. H_2 breakthrough can be observed within only ~1 min. after initial reduction of the carrier, indicating poor utilization of the carrier. This poor performance is confirmed by the extremely weak CO signal during oxidation and agrees with the limited utilization of the Fe@SiO_2 carrier seen in the TGA studies discussed above. Clearly, Fe@SiO_2 is a poor carrier material, resulting in CO yields which are about two orders of magnitude lower than for Fe-BHA. Not surprisingly, this trend holds also at lower reaction temperature:

Operating a Fe@SiO$_2$ fixed-bed at temperatures below 800°C, essentially no activity for CO$_2$ reduction is observed (refer Figure 48b).

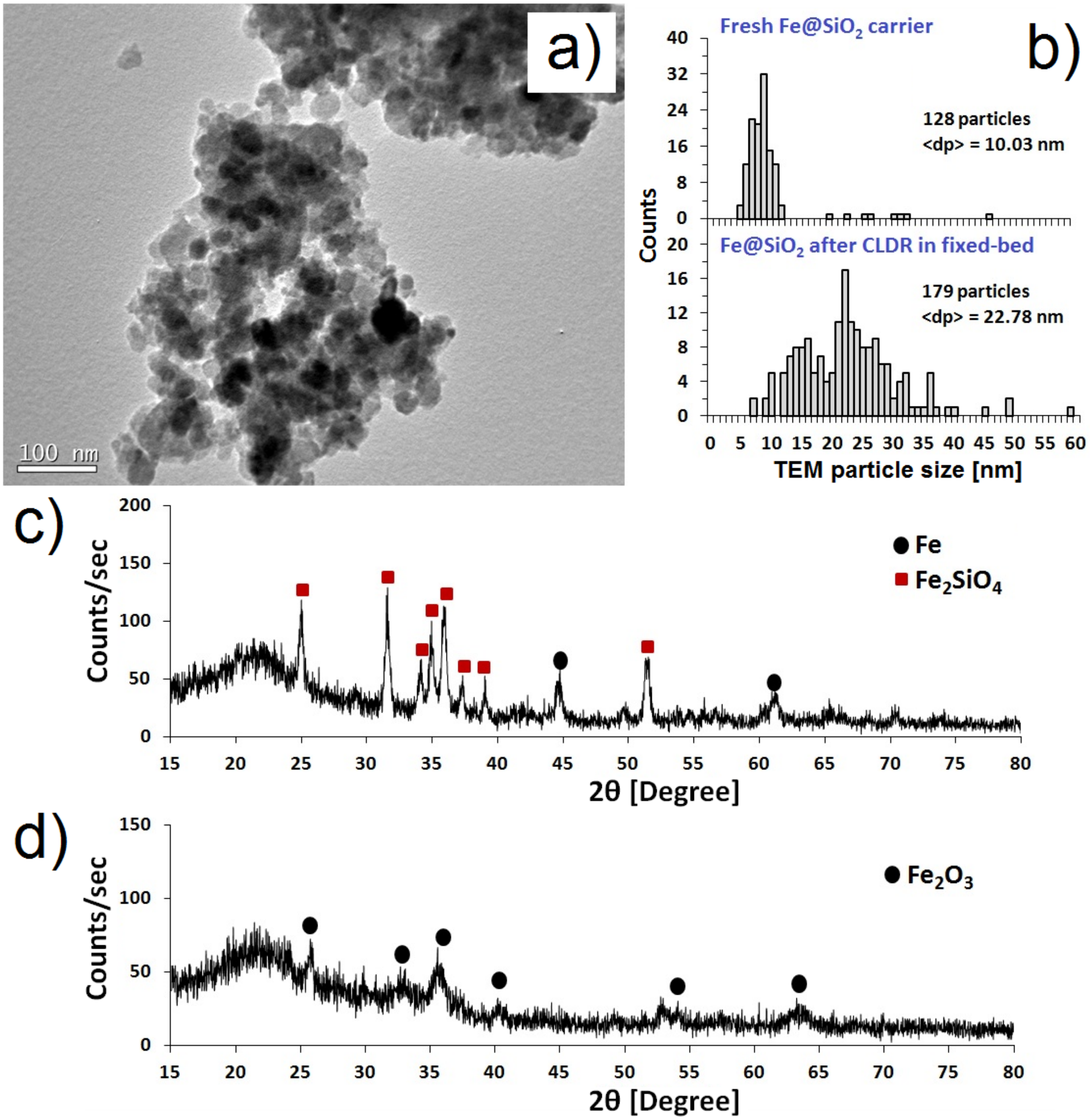

Figure 49. (a) TEM micrograph of a typical Fe@SiO$_2$ after exposure to multiple CLDR cycles; (b) Fe particle size distribution before and after CLDR cycles (calculated from TEM); XRD patterns of (c) a reduced Fe@SiO$_2$ carrier after fixed-bed CLDR operation, (d) the same carrier after oxidation in air at 500°C.

To elucidate the cause for the drastic difference in the performance of the two oxygen carriers, Fe@SiO_2 was characterized in detail after CLDR operation by TEM, BET, and XRD. Figure 49a shows a typical TEM micrograph of Fe@SiO_2 after multiple CLDR cycles at 800°C. The image shows a collapse of the core-shell structure due to insufficient hydrothermal stability of silica at the high temperatures and high steam partial pressures during the reduction half-cycle[151], resulting in an increase in average Fe particle size from ~10 nm to ~21 nm with a significant population of Fe particles with large diameters (see Figure 49b). BET analysis shows a decrease in surface area to ~72 m^2/g and a reduction in pore volume by ~17%, but overall still a highly porous composite material in which the Fe nanoparticles remain at least partially accessible. The collapse of the silica structure alone can therefore not explain the drastic loss of activity. Instead, the formation of iron silicates (Fe_2SiO_4) strongly affects the reduced carrier capacity of Fe@SiO_2: XRD analysis of Fe@SiO_2 after multiple CLDR cycles shows the formation of Fe_2SiO_4 alongside with metallic Fe (Figure 49c). The formation of Fe_2SiO_4 in a reducing environment is well known[66] and results in "trapping" Fe in the highly stable Fe_2SiO_4 spinel phase, rendering it unavailable for the reduction of CO_2 to CO. In agreement with this, XRD analysis of the carrier after re-oxidation with CO_2 showed an unchanged presence of the silicate phase, i.e. the inability to re-oxidize this phase with CO_2.

6.2.3 Two-step oxidation for CLDR

Since the formation of silicates (along with structural instability) results in minimal activity for Fe@SiO_2 in CO_2 activation, an alternate reaction scheme was considered to fully regenerate the Fe content of the Fe@SiO_2 carriers: An additional oxidation step with air was introduced between the (incomplete) oxidation with CO_2 and the subsequent reduction with H_2, since CO_2 is apparently too weak an oxidant to regenerate Fe_2SiO_4 to Fe_xO_y and SiO_2. To evaluate the viability of this scheme, used Fe@SiO_2 was oxidized in air (0.1 SLM) at 500°C for 1 hr and analyzed in XRD. Figure 49d shows that this additional oxidation step removes any evidence of Fe_2SiO_4, i.e. it re-oxidizes the sample completely to Fe_2O_3 as follows:

$$2\ Fe_2SiO_4 + O_2\ (\text{air}) \rightarrow 2\ Fe_2O_3 + 2\ SiO_2 \qquad \ldots(\text{R24})$$

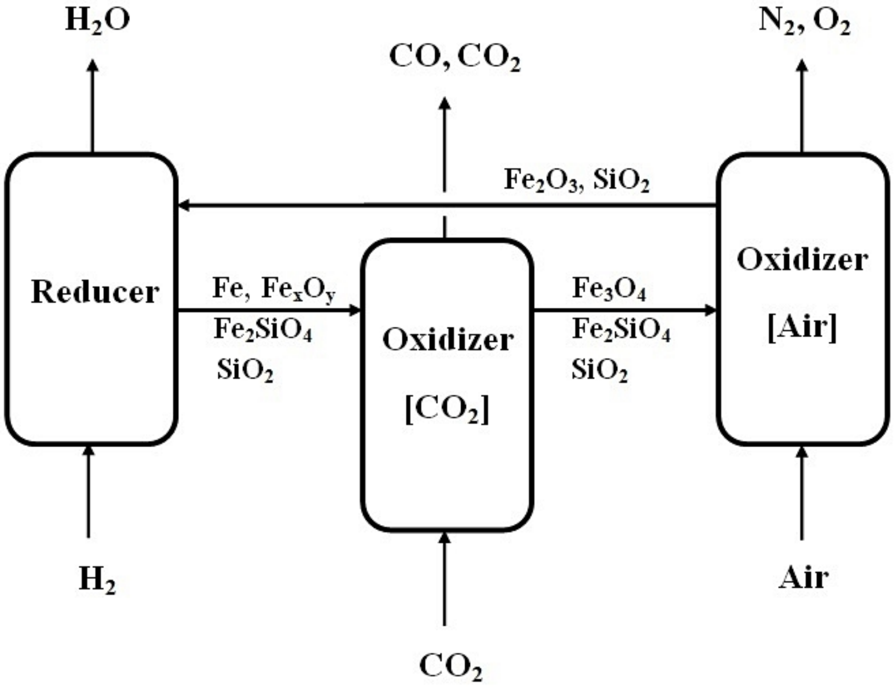

Figure 50. Schematic of the modified CLDR process using a two-step oxidation scheme.

Thus, we propose a two-step oxidation of the Fe@SiO_2 carrier for CLDR operation, as illustrated schematically in Figure 50. The fully oxidized oxygen carrier (Fe_2O_3@SiO_2) is reduced in contact with a fuel (here: H_2), resulting in the formation of metallic Fe and Fe_2SiO_4. This solid stream is sent to a first oxidizer in which the metallic Fe is oxidized to Fe_3O_4 in contact with CO_2, producing CO, followed by a second oxidation stage with air where both Fe_3O_4 and Fe_2SiO_4 are oxidized to Fe_2O_3 (and SiO_2). This fully regenerated oxygen carrier is then finally re-circulated to the reducer reactor.

The viability of this process scheme was further tested in fixed-bed reactor experiments, which were modified from the above experimental set-up by including the described second oxidation step. All other experimental conditions were kept identical to allow for direct comparison of the performance between these two configurations.

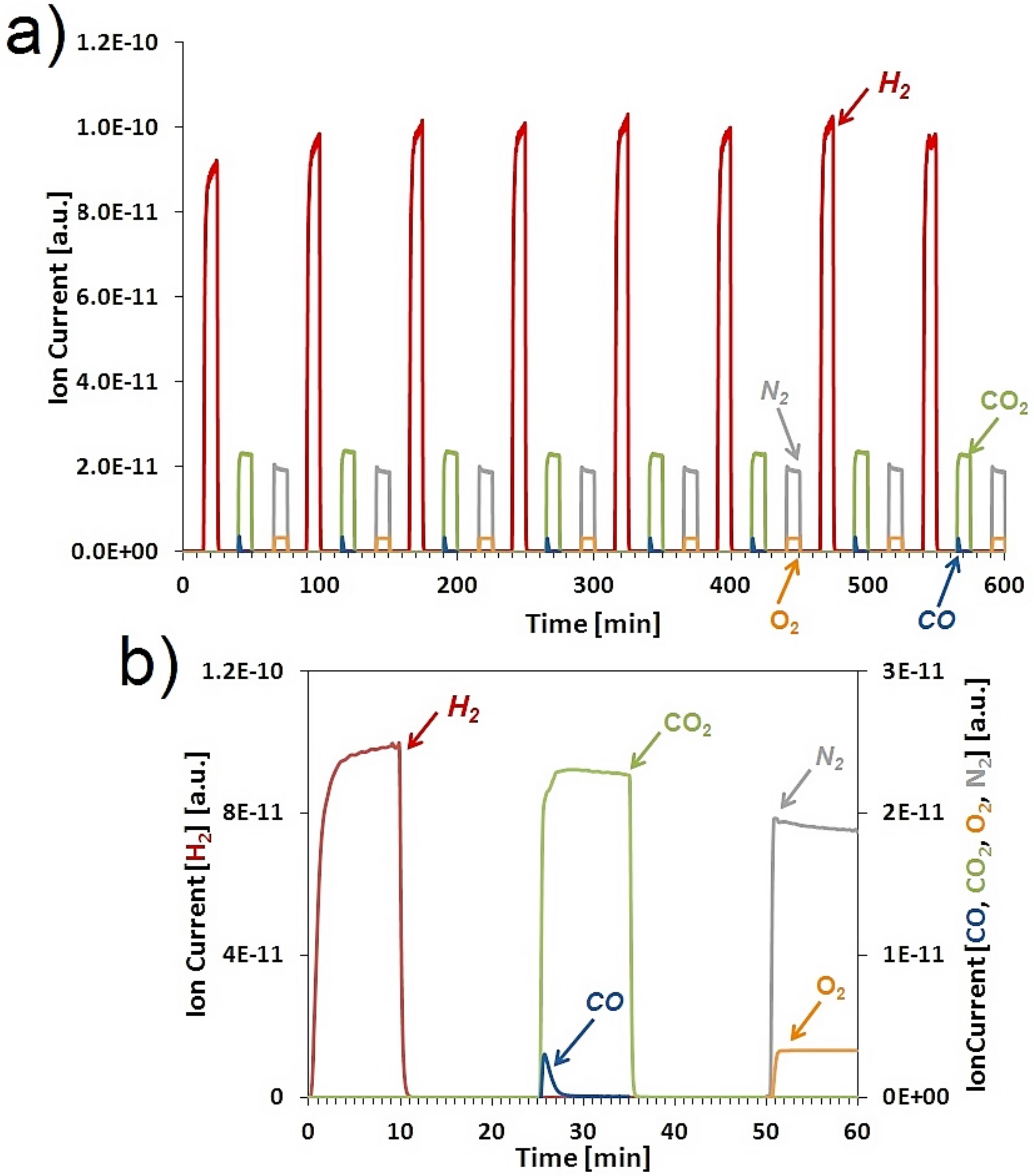

Figure 51. (a) Multiple redox cycles in the modified two-step CLDR scheme with Fe@SiO$_2$ at 800°C, using CO$_2$ (20% CO$_2$ in Ar) as oxidant and H$_2$ (5% H$_2$ in Ar) as model fuel. (b) Enlarged single cycle.

Figure 51a shows eight redox cycles using Fe@SiO$_2$ in the two-stage fixed-bed CLDR process at 800°C. Stable operation of the carrier can be seen as apparent from the unchanged concentration traces over the 10 hrs of operation. Figure 51b shows an enlarged view of a single cycle. During reduction, H_2 is initially consumed and breaks through after about 2-3 minutes. During oxidation with CO_2, a distinct CO peak is observed over the first few minutes, indicating oxidation of the reduced carrier by CO_2. Finally, during oxidation by air, low initial oxygen concentration indicates consumption by carrier oxidation until breakthrough is observed after about 1-2 min., indicating complete carrier oxidation. In comparison to the results with a single oxidation stage (Figure 48a), the increased duration of H_2 consumption before breakthrough and the more pronounced CO peak during oxidation with CO_2 indicate a significant improvement of carrier utilization.

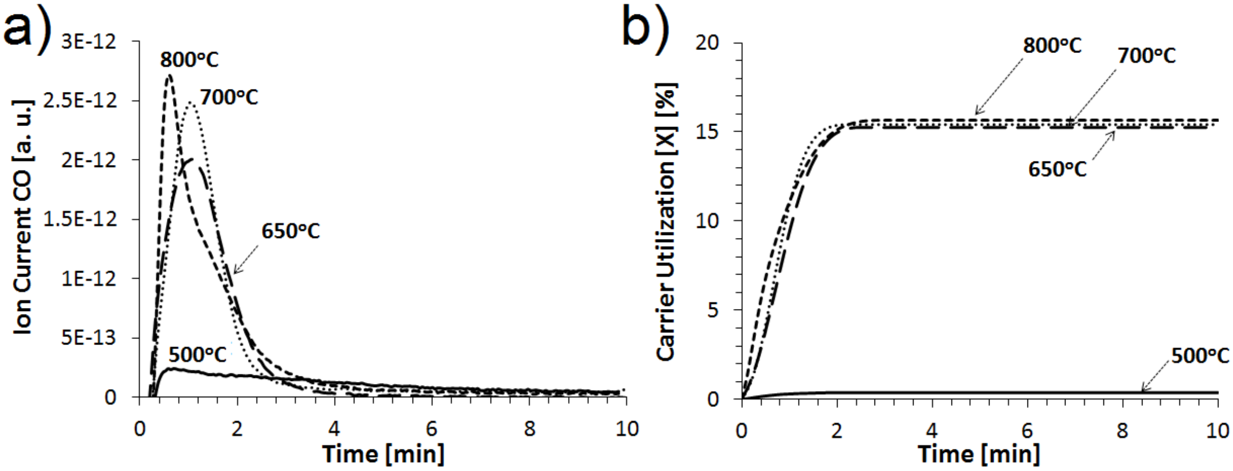

Figure 52. (a) CO generation over one oxidation half-cycle at different temperatures using Fe@SiO$_2$ in the modified two-step CLDR scheme; (b) Fe@SiO$_2$ oxygen carrier conversion (%) as a function of time at different temperatures.

This is further confirmed in experiments over a broader temperature range: Figure 52a shows the CO concentrations during the first oxidation stage of the two-step CLDR process for temperatures between 500 and 800°C. Unlike for the single-stage oxidation process, where CO production had virtually stopped at 600^{o}C, minimal change occurs in CO formation for the two-step process when reducing the temperature from 800^{o}C to 650^{o}C, as shown in Figure 52b. However, while carrier utilization is strongly improved compared to the one-step process with Fe@SiO$_2$, carrier conversion is still limited to ~15%. This is most likely due to limited accessibility of Fe, some of which might become entirely occluded below a non-porous (collapsed) silica layer, as well as the increase in particle size of the now insufficiently stabilized Fe nanoparticles.

Overall, the proposed two-step CLDR process is hence reasonably effective in CO generation even with Fe@SiO$_2$ carriers due to a regeneration of the silicate phase. However, the instability of silica at the demanding process conditions and hence the partial collapse of the core-shell structure still result in a significantly lower activity compared to Fe-BHA, indicating that the proper choice of carrier matrix material is critical for CLDR.

6.2.4 Brief insights into process challenges and energetics

We demonstrated here that CLDR can offer a novel and efficient pathway for CO$_2$ activation via reduction to CO. The use of cheap and abundant iron adds to the attractiveness of this process. Stability and activity of the carrier is critical, as indicated by the comparison between the Fe-BHA and Fe@SiO$_2$. While microemulsion-based syntheses might result in increased carrier cost, we have already conducted first steps towards simplifying the synthesis of Fe-BHA by depositing Fe via a standard deposition-precipitation route onto BHA. The resulting carriers were indistinguishable in materials characteristics and chemical looping performance, indicating that stable and active carriers can be produced via cheap and proven synthesis techniques.

However, several aspects of this process need further consideration and better understanding to develop this process towards technical feasibility. In particular the CO_2 source, the overall energy balance of the process, and the specific fuel used in the process require further discussion.

First, the supply of CO_2 for the CLDR process could either come in the form of a conventional power plant effluent stream, or as a concentrated or even pure CO_2 stream from the effluent of a CLC process (thus coupling CLC and CLDR), or from a CO_2 separation step such as a calcium looping process[152]. For the first case, the interactions of the carrier with other flue gas constituents needs to be evaluated, ranging from CO to H_2O and minor contaminants, such as sulfur compounds. We have previously shown that sulfur contaminants do not necessarily negatively impact carrier operation in CLC and can even lead to significant increases in oxygen carrying capacities, but the impact of such contaminants on operation with CO_2 is unknown[153-154].

For high concentration CO_2 feed streams in particular the incomplete conversion of CO_2 in the process poses another challenge. While separation of CO and CO_2 is feasible with current technology, it adds another process step which would contribute further a cost and energy penalty onto the overall CO_2 utilization scheme. Improvements in CO_2 conversion are hence needed to improve the economics of the proposed process. An extension of the carrier bed length could offer one path towards such improvements.

Possibly the most critical factor in any CO_2 abatement technology is the energy requirement for the process. While the proposed CLDR technology has several advantages over conventional catalytic dry reforming processes which make it a highly intensified process, including the use of cheap iron-based materials, optimization of the process towards production of CO rather than H_2, and the inherent separation of the CO/CO_2 stream from H_2/H_2O (greatly facilitating a potential down-stream CO/CO_2 separation), it also yields a net process which is even more endothermic than catalytic dry. Clearly, the delivery of clean and cheap energy is hence critical for CLDR.

One possibility to address this is the use of concentrated solar-thermal energy. Major efforts are currently focused on the design of efficient reactor systems and materials for capturing solar energy and concentrating it for thermal decomposition of oxides[87, 155-156], essentially offering a "fuel-free" alternative to the proposed CLDR process. However, one of the major issues with solar-thermal processes is the extremely high process temperatures, typically in excess of ~1200^oC, required to thermally decompose suitable oxygen carriers. A hybrid between these purely solar-thermal processes and the presently proposed chemical fuel-based CLDR process would allow to lower this temperature to as low as ~600^oC (as demonstrated in the present results), drastically reducing the demand on solar radiation intensity and effectively avoiding materials issues.

A second, highly promising alternative arises from the alternate two-step oxidation process, proposed here for the utilization of Fe/silica-based carriers, but applicable to any carrier. The enthalpy balance for this reaction scheme, at 800^oC, is shown below:

Reducer: $^3/_2Fe_2O_3 + {}^3/_8CH_4 = 3FeO + {}^3/_4H_2O + {}^3/_8CO_2$ $\Delta H_R = 103.2$ kJ/mol…(R25)

1st Oxidation: $3FeO + CO_2 = Fe_3O_4 + CO$ $\Delta H_R = -2.125$ kJ/mol…(R26)

2nd Oxidation: $Fe_3O_4 + ¼\, O_2 = {}^3/_2\, Fe_2O_3$ $\Delta H_R = -119.0$ kJ/mol…(R27)

Net reaction: $^3/_8CH_4 + {}^5/_8CO_2 + ¼O_2 = CO + ¾H_2O$ $\Delta H_R = -17.96$ *kJ/mol*…(R28)

As seen from this scheme, by adding the second, highly exothermic air-fed oxidation step, the overall process becomes *exothermic*. Hence, through this modified process scheme, CLDR can be operated without the addition of an external energy source, i.e. it becomes an intensified autothermal dry reforming process. The required energy is instead supplied via an additional fuel feed in order to reduce the carrier from its higher oxidation state. For CH_4 as fuel, this result in a 50% increase in fuel requirement per mole CO produced. This is likely to be an acceptable cost, in particular since the CLDR process allows the same highly efficient capture of CO_2 emissions from the fuel conversion step as conventional CLC. However, a full economic analysis is required to assess the added cost and increased complexity of this process scheme. A fixed-bed reactor configuration, as proposed by us earlier, would likely reduce this cost and complexity by replacing the moving solid phase in multiple reactors with periodically alternating gas feed to a single reactor[84].

Finally, the present work has been entirely focused on the oxidation side of the process, i.e. on the reduction of CO_2 to CO. However, fuel conversion is as critical as CO_2 conversion. The most likely fuel for a CLDR process is natural gas, in particular considering the dramatic increase in proven natural gas reserves in recent years due to advances in drilling technology which have rendered vast shale gas reserves economically accessible[157]. However, complete conversion of CH4 (and minor components of natural gas, such as ethane) needs to be verified, although existing studies on methane combustion with Fe-based carriers in CLC have shown encouraging results[14, 32].

6.2.5 Chemical looping reforming for syngas generation

Previous work from our laboratory on chemical looping steam reforming (CLSR) have shown that, steam can be successfully used as oxidizing agent for simultaneous generation of ultra-pure H_2 with CO_2 capture at reducer exhaust[75]. Based on the prior knowledge of CLSR (section 1.2.2) and above discussed results of CLDR, and on the fact that both processes give optimal results using Fe-based carriers, it seems logical to attempt a combination of the two reactions to yield a direct syngas production process from H_2O and CO_2. The resulting process is analogous to the production of solar fuels using similar metal oxide cycles, but replacing the solar-thermal reduction of the metal with a more conventional reduction using a fuel[86, 158]. The process could be seen as a possible bridge technology in a transition from fossil-fuel based generation of energy and fuels to solar-energy based technologies. In this reaction scheme, the carrier oxidation side is essentially “running combustion in reverse”, while the carrier reduction could be conducted in a fuel flexible way, i.e. one could imagine using any fuel, including renewables, as long as the fuel shows sufficient reactivity with the oxygen carrier. The reactions are shown here for methane as fuel and the transition between FeO and Fe_3O_4 as lowest and highest oxidation state of the carrier, and for a flexible H_2O:CO_2 ratio in the oxidizer feed. One can see that this process would result in a highly flexible scheme for the production of synthesis gas with widely adjustable H_2:CO ratio:

Oxidizer: $12\ FeO + (4 - x)\ CO_2 + x\ H_2O = 4\ Fe_3O_4 + (4 - x)\ CO + x\ H_2$ …(R29)

Reducer: $CH_4 + 4\ Fe_3O_4 = 12\ FeO + CO_2 + 2\ H_2O$ …(R30)

Net reaction: $CH_4 + (3 - x)\ CO_2 + (x - 2)\ H_2O = 4\ Fe_3O_4 + (4 - x)\ CO + x\ H_2$ …(R31)

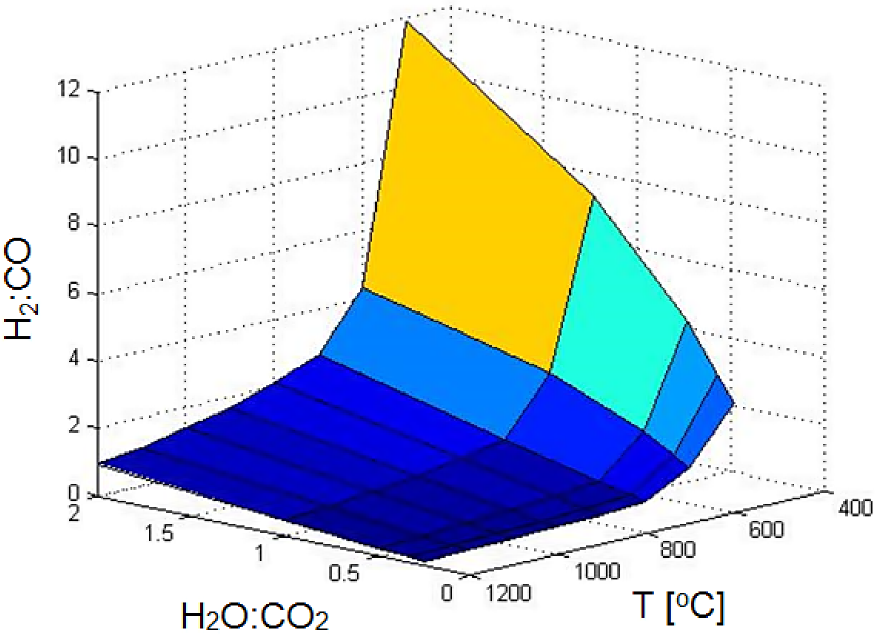

Figure 53. Thermodynamic calculations for the production of syngas from (CO_2, H_2O) – mixtures using Fe-based carrier, shown as a function of temperature and H_2O:CO_2 ratio in the feed. Conceptually, such a process would allow the generation of syngas with a wide range of syngas ratios.

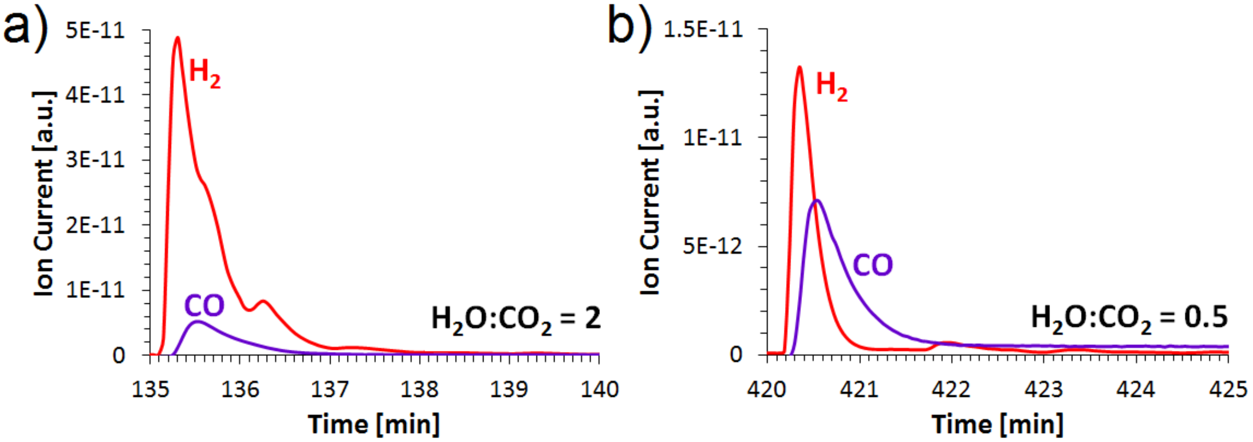

Figure 54. Syngas (H_2 and CO) production at 800°C during oxidation of 100 mg Fe-BHA (40 wt.% Fe) carrier in a fixed-bed reactor configuration with a (H_2O:CO_2) – mixtures (a) H_2O:CO_2 = 2 and (b) H_2O:CO_2 = 0.5. Oxidizer feed conditions: 3.8 cc/hr $H_2O_{(l)}$, 45 cc CO_2 for H_2O:CO_2 = 2 and 2 cc/hr $H_2O_{(l)}$, 95 cc CO_2 for H_2O:CO_2 = 0.5. The low reactivity of CO_2 compared to steam results in much more efficient conversion of H_2O.

Thermodynamic calculations confirm that it should indeed be possible to achieve a wide range of H_2:CO product ratios (refer Figure 53). However, experiments confirm the feasibility of such a reaction scheme, the strongly different reactivity of H_2O and CO_2 results in a significant challenge for carrier design: Utilizing again an Fe-BHA carrier, we find a much higher conversions for steam than for CO_2, i.e. a very H_2-rich syngas is obtained even for CO_2-rich feed streams (refer Figure 54). Clearly the different reactivity of the two oxidants and the strong interdependence of thermodynamics and kinetics of the two reduction reactions as a function of temperature and feed composition pose a formidable process design and optimization problem with very high sensitivity to fluctuations in feed and process conditions. Therefore, compared to CLMR (inherently endothermic in nature), previously discussed chemical looping partial oxidation process (see chapter 5.0) is a more attractive yet pragmatic approach for syngas generation with higher reaction rates and conversion with potential for autothermal operation.

6.3 SUMMARY

Chemical looping dry reforming (CLDR) is a novel and efficient route for CO_2 activation which offers a novel and intensified alternative to dry reforming. In the present report, we evaluated the performance of two Fe-based oxygen carriers for CLDR. In one case, Fe nanoparticles were embedded into a high-temperature stabilized alumina matrix (Fe-BHA). In the other carrier Fe nanoparticles were encapsulated into porous silica shells. Both carriers were evaluated with regard to activity and stability in thermogravimetric and fixed-bed reactor studies. Fe-BHA was found to show fast redox kinetics and stable operation over multiple cycles in CLDR at temperatures as high as 800^{o}C, whereas Fe@SiO_2 showed very poor activity for CO generation due to a partial loss of the core–shell structure and Fe_2SiO_4 formation. Even after regeneration of the silicate-bound Fe via a two-step oxidation scheme, which resulted in improvements for the Fe@SiO_2 carrier, the carrier utilization of the Fe-BHA carrier (~51% at 800^oC) was superior to Fe@SiO_2 (~15% at 800^oC). Interestingly, however, this novel two-step oxidation scheme is highly beneficial for the overall energy balance of the process, turning the net endothermic CLDR process into a net exothermic process (at the expense of higher fuel consumption and increased process complexity).

As a last step, we extended the chemical looping reforming concept by using mixed feed of steam and CO_2 as oxidants to investigate for syngas generation. Although it is thermodynamically feasible to produce syngas with tunable syngas ratio by changing the feed concentrations of steam and CO_2, low reactivity of CO_2 compared to steam pose a challenge in generating syngas with widely tunable H_2:CO ratio.

Overall, we think that the two-step oxidation configuration proposed in this study can be applied to all chemical looping reforming variants to transform these typically endothermic reforming reactions into a net exothermic process which warrants further investigation.

7.0 SUMMARY AND OUTLOOK

7.1 SUMMARY

Previous work in our laboratory has shown that use of high temperature stable supports like barium hexaaluminates provides the required thermal stability to metal oxides in engineered/synthetic oxygen carriers. However, conventionally used non-reducible oxide-based supports do not contribute towards oxygen carrying capacity or facilitate the reduction of metal oxides, therefore extra energy has to be spent in handling of such inert support materials. In the present thesis, we focused our efforts on using reducible oxides like ceria as supports in Chemical Looping Combustion (CLC). Although a novel idea in CLC community, ceria is known to be “active” in oxygen transport for variety of oxidative catalytic systems. In CLC, it was found that independent of the type of metal/s used, ceria facilitates good thermal stability of metal/alloys and substantially augments carrier reactivity and utilization of oxygen in place.

Subsequent studies were conducted with the aim to improve the carrier reactivity by systematically tailoring the metal phase (Ni_xFe_{1-x}-CeO_2 and Mn_xFe_{1-x}-CeO_2). In case of Ni_xFe_{1-x}-CeO_2, it was found that increasing the concentration of reactive nickel species in low reactive iron leads to improved carrier performance, while reactivity-composition correlations were not so straight forward in case of Mn_xFe_{1-x}-CeO_2. Pure manganese was effectively stabilized by ceria, but doping iron into manganese strongly enhanced carrier reactivity.

Furthermore, the idea of tailoring the metal phase coupled with modifying fuel reactor operation was used to produce syngas via partial oxidation of methane. Avoiding direct contact of methane and oxygen makes chemical looping partial oxidation an inherently safe process, but it also eliminates the need for expensive air separation and uses cheap transition metal based metals. On the other hand, by changing the oxidizer feed gas to steam, CO_2 or mixtures of H_2O/CO_2, the flexibility of chemical looping can be effectively used for ultra-pure H_2 and syngas generation or CO_2 reduction. Although the reforming reactions result in a net endothermic system, the reaction scheme can be engineered to yield a net exothermic process by employing a second oxidizer using air as oxidant.

Overall, the present work demonstrates the flexibility offered by looping processes in targeting clean combustion, partial oxidation, and CO_2 activation; however optimizing the carrier materials actually enables the processes and makes them practically viable.

7.2 OUTLOOK

7.2.1 Oxygen transport mechanism in cerium oxides

The initial work in this thesis is primarily based on demonstrating the idea of using reducible oxides as supports in CLC to tackle the problem of inert circulation in synthetic or engineered oxygen carriers. We have successfully showed that ceria-based oxygen carriers can not only stabilize the metal/s phases but also significantly accelerate the redox kinetics with overall increase in their oxygen carrier utilization. The idea of using reducible oxides is not limited to specific metals, e.g. Ni, but can be broadly applied to various transition metals used in CLC.

Although use of reducible oxides result in much improved performance of oxygen carriers, there is insufficient understanding of the underlying redox mechanism – essential to further optimize the oxygen carriers in chemical looping. Typically in gas-solid reactions, deeper reduction and re-oxidation of metal is hindered by diffusion limitations. The rate of oxygen transport from metal oxides can directly affect the product selectivities in oxidation of carbon-based fuels. In contrast, ceria supported metals show sustained rate of oxygen transport with high selectivities for total oxidation of methane. Therefore, we proposed a possible oxygen transport mechanism (refer Figure 17) in which the metal-support interface plays a critical role in sustaining high rate of oxygen transport from supported metals. However, use of experimental techniques to investigate such complex interactions is a non-trivial problem, therefore one can leverage computational modelling for model validation Advances in computational material science and density function theory calculations over recent decades have had profound impact on our ability to computationally test/predict material properties and possible reaction pathways[159-163]. Such tools can be used in accessing the viability of the proposed oxygen transport model and accurately predict the possible reaction pathways to further our understanding of ceria-based oxygen carriers.

Apart from computational modelling, synchrotron facilities housing experimental tools like *operando* XRD, XPS and XANES can be immensely helpful in determining the oxidation states of various metals during carrier reduction under experimental conditions. This type of dynamic information could shed light on the oxygen transport mechanism. For example, does reduction of metal and support occur simultaneously or sequentially? How does it depend on the gas phase compositions (H_2 vs CH_4)? Does metal nanoparticle structure and size play a critical role in oxygen transport? Answers to such questions can potentially allow us to more accurately correlate structure and reactivity, but can also aid in deciding the synthetic techniques and optimal metal loadings to maximize this beneficial effect seen with ceria-based oxygen carriers.

7.2.2 Tailoring reducible supports to increase oxygen mobility

Broad applicability of reducible supports like ceria with nickel, iron, manganese and their mixed-oxide systems suggests that oxygen mobility in the support is responsible for the observed beneficial effects. Therefore, tailoring the structure/composition of ceria to enhance the oxygen mobility in support is a logical next step. Oxygen defect concentration in ceria is critical for its oxygen mobility which can be further enhanced through doping. Previous work from our laboratory[106, 164] on water gas shift catalyst design showed that reducibility of cerium oxide (Ce^{4+}) can be increased by aliovalent dopants like lanthana (La^{3+}), which upon doping ceria inherently creates oxygen defect sites and increases its reducibility. Temperature programmed reduction and oxidation results showed that nominal doping concentration results in enhanced reducibility while large concentration of La-doping quantitatively reduced the fraction of available ceria for reduction defeating the purpose of La-doping in the first place. As a result, limiting the La concentration in solid solutions of Ce-La is important to balance the two effects.

We have already taken initial steps and have synthesized and characterized various solid solutions of lanthana and ceria ($La_xCe_{1-x}O_{2-x/2}$). As discussed in above paragraph, we limit the lanthana concentration to 30% ($x > 0.3$). We deposit iron onto these supports and carriers are calcined at 900°C. Iron was chosen as metal of interest to concentrate our efforts on improving performance of low-cost and benign metals. Currently we are in process of testing these materials for CLC. Figure 55a shows the XRD spectra and average lattice parameters calculated from the XRD measurements. It can be seen that, upon doping lanthana into ceria no separate peaks of lanthana containing oxides or carbonates are observed, however increasing concentration of lanthana doping shifts the peaks to a lower diffraction angle. This change in d-spacing or peak shift can be used to calculate lattice spacing for the $La_xCe_{1-x}O_{2-x/2}$ oxides (see Figure 55b). It can be see that increasing the concentration of lanthana in the solid solution results in an increase in the lattice spacing, explained by the larger ionic radii of La^{3+} compared to Ce^{4+} in the $La_xCe_{1-x}O_{2-x/2}$ crystal. All the above observations confirm formation of a homogeneous solid solution and successful tailoring of reducible support.

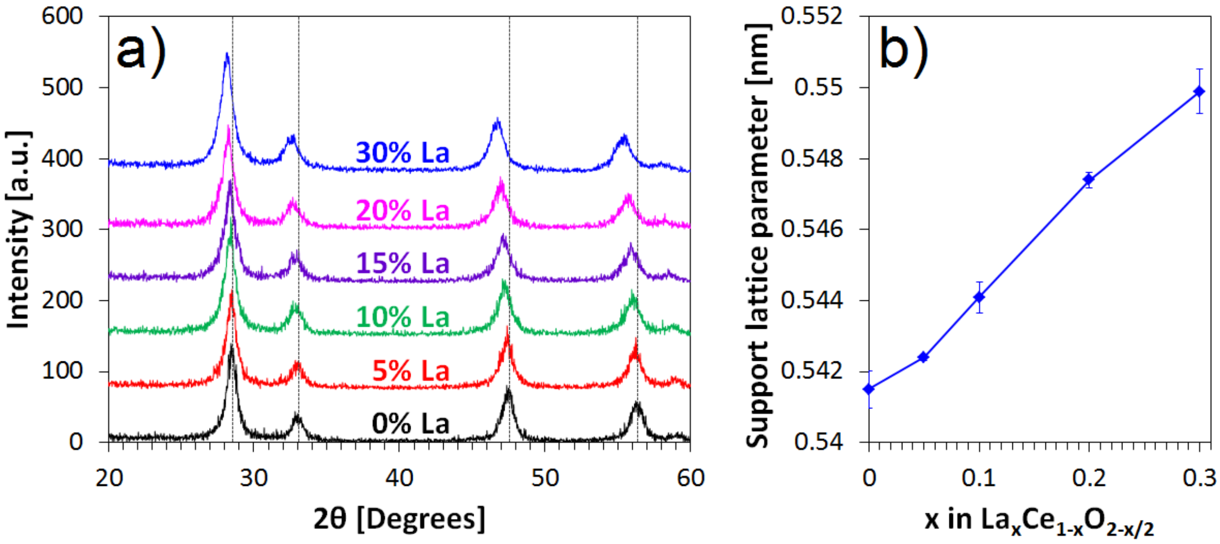

Figure 55. a) X-ray diffraction and b) average lattice spacing (calculated from XRD) of $La_xCe_{1-x}O_{2-x/2}$ oxides calcined at 450°C. No peaks of free lanthana phase, shift of XRD peaks to lower diffraction angle and increase in the lattice spacing confirm the formation of homogenous solid solution.

These Fe-$La_xCe_{1-x}O_{2-x/2}$ carriers are then subjected to redox cycling at 600°C in a TGA. A relatively low temperature (600°C) was chosen to slow down the redox kinetics to be able to clearly elucidate the effect of support reducibility on redox kinetics. Figure 56 shows the effect of lanthana doping on redox kinetics using H_2 as model fuel. It can be seen that increasing lanthana concentration does not significantly increase the amount of available oxygen for reduction, but small amount of lanthana doping (up to 10%) strongly accelerates the reduction kinetics (Figure 56a). Further increase in the amount of lanthana in support solid solution does not result in improved reduction kinetics, but adversely affects the amount of available oxygen for reduction. The observation can be understood by i) poor reducibility of lanthana compared to ceria (see Figure 5, Figure 6) and ii) formation of $LaFeO_3$ which is difficult to reduce at low temperatures. Similarly, concentration of lanthana doping shows a direct correlation with re-oxidation rate (Figure 56b) and strongly accelerates the re-oxidation process.

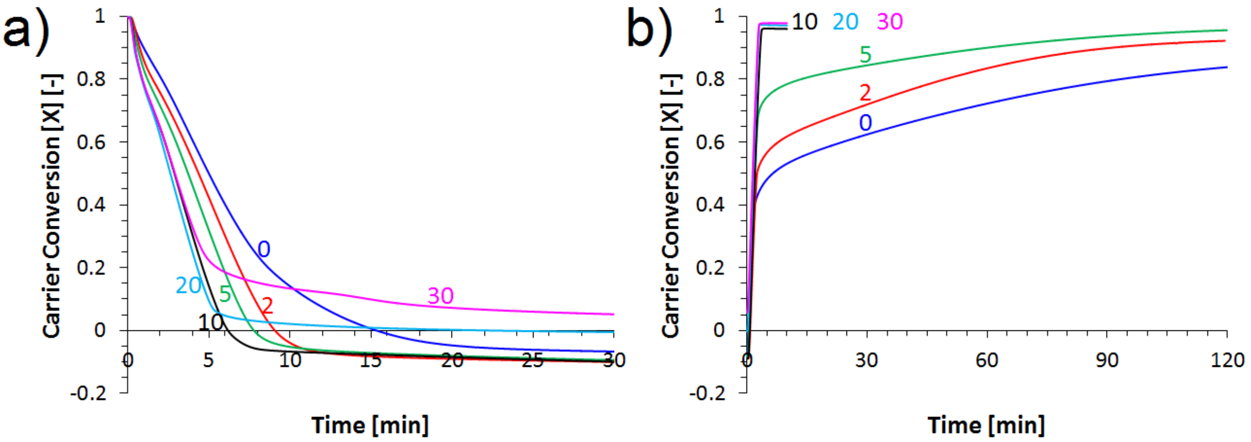

Figure 56. Comparison of carrier conversion profiles obtained from CLC operation in TGA during a) reduction in hydrogen (model fuel, 20 sccm) and b) re-oxidation in air (20 sccm) at 600°C demonstrating the effect of % lanthana doping in Fe-$La_xCe_{1-x}O_{2-x/2}$ carriers.

The preliminary tests are very encouraging and show that optimal concentration of lanthana doping in ceria supports allows maximizing the carrier conversion and redox kinetics. However, the tests are conducted with H_2 as a model fuel. Therefore, it is important to extend this work onto methane as fuel to understand how it impacts the redox kinetics of the carriers and their ability to selectively convert methane into CO_2 and steam.

The preliminary characterization work indicates that at high lanthana doping (>10%), iron has tendency to react with lanthana resulting in formation of $LaFeO_3$ (not shown). $LaFeO_3$ is found to be reducible at high temperature (900^oC) but show poor reduction kinetics (confirmed with use of pure La_2O_3 as support; not shown here). Therefore, it is also important to focus future efforts on stabilizing lanthana into the support matrix over a long multi-cycle CLC operation.

7.2.3 Chemical looping partial oxidation

Our work shows that chemical looping can be used for partial oxidation of methane by i) limiting the oxygen carrier supply (or their oxidation states) by means of reactor operation and ii) tailoring the metal phase to increase their reactivity and selectivity for syngas formation. Apart from material optimization, reactor operation is critical to minimize the formation of coke or CO_2. Due to sequential reduction of iron oxides as $Fe_2O_3 \rightarrow Fe_3O_4 \rightarrow FeO \rightarrow Fe$, eliminating carbon formation on partially reduced carriers is relatively easy because methane pyrolysis predominantly occurs on metallic iron. However, re-oxidation of metallic iron is not a set of steps in sequence, but they occur concomitantly[122], which also results in formation of Fe_2O_3. Since reduction of Fe_2O_3 to Fe_3O_4 is strongly selective for total oxidation of methane[39, 122], it reduces the selectivity towards desired products, i.e, CO and H_2. Therefore presence of Fe_2O_3 is detrimental for chemical looping partial oxidation process, and limiting the re-oxidation of Fe-based carriers beyond Fe_3O_4 is important.

Although steam and CO_2 are weaker oxidants than air, CLSR and CLDR studies show that re-oxidation with these oxidizing gases is thermodynamically limited to Fe_3O_4. Hence combining chemical looping partial oxidation with chemical reforming process can be a potential solution to further improve the selectivity of syngas in the reducer. However, analysis of process energetics would be required to limit the external heating requirements due to endothermic nature of the oxidizer reactions. Previous thermodynamic analysis from our laboratory demonstrates that nickel is difficult to oxidize with H_2O or CO_2. This can be beneficial in case of Ni_xFe_{1-x}-CeO_2 carriers for CLPOM. If nickel can be maintained in reduced state, it can possibly assist in methane activation[123] while bulk iron oxides can be used as a source of oxygen. However, it is important to note that thermodynamic and kinetic properties of nickel could potentially change due to alloying with iron.

7.2.4 Iron manganese mixed oxides

We observed that mixed-oxides of iron and manganese (Mn_xFe_{1-x}-CeO_2) are very promising due to low-cost and benign nature of both the metals. Overall, these mixed oxide carriers are difficult to characterize by XRD – a technique that differentiates between elements based on their atomic number or electron density. Unfortunately both iron and manganese oxides show same crystal structures and are placed next to each other in periodic table, making it impossible to use XRD as a tool to unambiguously confirm various phases of iron and manganese present in the sample. Therefore, in our work, we take aid of indirect techniques like EELS, effect of calcination temperature and Rietveld analysis to confirm formation of bimetallic phase.

However, unlike conventional XRD, neutron diffraction can be used to clearly characterize these oxides with high level of confidence; because in neutron diffraction technique, neutrons interact with nucleus of an atom and different metals show different neutron scattering length which is independent of electron density. Typically, neutron diffraction provides information which complements XRD, and it is effective in differentiating neighboring elements in the periodic table. Such high resolution powder diffraction experiments of polycrystalline samples can be conducted on POWGEN powder diffractometer (beamline HB-2A) at Oak Ridge National Laboratory. When compared to synchrotron X-ray radiations, Spallation Neutron Sources (SNS) produce relatively low strength beams, thus one requires relatively large amount of sample for neutron diffraction compared to conventional XRD. However, different neutron scattering lengths of iron and manganese (Fe: ~ 0.9×10^{-12} vs Mn: ~ -0.4×10^{-12} cm^2) can be effectively used to test for presence of various pure Fe-, Mn-oxides in Mn_xFe_{1-x}-CeO_2 mixed oxide samples.

Moreover, we observed that all Fe-Mn mixed-oxides except Mn-rich carriers (e.g. $Mn_{0.8}Fe_{0.2}$-CeO_2) de-alloyed in reduction process, thus eliminating any beneficial effect of combining both the metals. Although Mn-rich carriers improved on the reactivity of pure Mn- or Fe-based carriers, currently there is limited mechanistic understanding of reduction of such carriers. Therefore *in-situ* neutron diffraction experiments can be helpful in providing some insights into oxygen release from the material e.g. determining the relative rates of reduction of both the metals in the alloy. POWGEN Powder Diffractometer equipped with a gas atmosphere furnace ($T_{max} = 850^oC$) on beamline HB-2A can be used for such experiments. Finally, present work on Fe-Mn mixed oxides shows that systematic tailoring of metal phase can result in carriers which are more active, but in-depth analysis of these materials is important to design more efficient oxygen carriers with proper knowledge of structure-activity relationships.

APPENDIX A

NANOCOMPOSITE FE-BHA SYNTHESIS

Table 8. A typical recipe for Fe-BHA (40.04 wt.% Fe) synthesis

		MW	moles	Mass (g)	Vol (ml)
Microemulsion	PEPP (surfactant)	2000	0.0050	10.0	--
	Pentanol (co-surfactant)	88.15	1.3213	116.5	142.9
	Iso-octane (oil phase)	114.23	0.2621	29.9	43.4
	H_2O (aqueous phase)	18.02	0.4732	8.5	--
	$Fe(NO_3)_3.9H_2O$ (aqueous phase)	404.0	0.0163	6.587	--
Metal alkoxide	Al-isopropoxide	204.24	0.0213	4.3572	--
	Ba-isopropoxide	255.51	0.0018	0.4599	--
	Isopropanol	60.10	1.0885	65.42	83

BIBLIOGRAPHY

(1) *IEA, World Energy Outlook, 2013*; IEA: Paris, France, **2013**.

(2) Hallman, M., Steinberg, M., Greenhouse Gas Carbon Dioxide Mitigation: Science and Technology. Lewis Publishers: Boca Raton, FL, USA, 2000.

(3) Kanniche, M.; Gros-Bonnivard, R.; Jaud, P.; Valle-Marcos, J.; Amann, J. M.; Bouallou, C. Pre-combustion, post-combustion and oxy-combustion in thermal power plant for CO_2 capture. *Appl. Therm. Eng.* **2010,** *30*, 53-62.

(4) Kothandaraman, A.; Nord, L.; Bolland, O.; Herzog, H. J.; McRae, G. J. Comparison of solvents for post-combustion capture of CO_2 by chemical absorption. *Energy Procedia* **2009,** *1*, 1373-1380.

(5) Rhee, C. H.; Kim, J. Y.; Han, K.; Ahn, C. K.; Chun, H. D. Process analysis for ammonia-based CO_2 capture in ironmaking industry. **2011,** *4*, 1486-1493.

(6) Perry, K. A.; Eisman, G. A.; Benicewicz, B. C. Electrochemical hydrogen pumping using a high-temperature polybenzimidazole (PBI) membrane. *J. Power Sources* **2008,** *177*, 478-484.

(7) Bara, J. E.; Carlisle, T. K.; Gabriel, C. J.; Camper, D.; Finotello, A.; Gin, D. L.; Noble, R. D. Guide to CO_2 Separations in Imidazolium-Based Room-Temperature Ionic Liquids. *Industrial & Engineering Chemistry Research* **2009,** *48*, 2739-2751.

(8) Li, J. R.; Kuppler, R. J.; Zhou, H. C. Selective gas adsorption and separation in metal-organic frameworks. *Chem. Soc. Rev.* **2009,** *38*, 1477-1504.

(9) Trachtenberg, M. C.; Cowan, R. M.; Smith, D. A.; Horazak, D. A.; Jensen, M. D.; Laumb, J. D.; Vucelic, A. P.; Chen, H.; Wang, L.; Wu, X. Membrane-based, enzyme-facilitated, efficient carbon dioxide capture. **2009,** *1*, 353-360.

(10) Audus, H. In *leading options for the capture of CO_2 at power stations*, Fifth Conference on Greenhouse Gas Control Technologies, Cairns, Australia, Cairns, Australia, 2000.

(11) Gottlicher, G.; Pruschek, R. Comparison of CO_2 removal systems for fossil-fueled power plant processes. *Energy Conv. Manag.* **1997,** *38*, S173-S178.

(12) Adanez, J.; Abad, A.; Garcia-Labiano, F.; Gayan, P.; de Diego, L. F. Progress in Chemical-Looping Combustion and Reforming technologies. *Prog. Energy Combust. Sci.* **2012,** *38*, 215-282.

(13) Fan, L. S.; Zeng, L.; Wang, W.; Luo, S. Chemical Looping Processes for CO_2 Capture and Carbonaceous Fuel Conversion–Prospect and Opportunity. *Energy Environ. Sci.* **2012,** *5*, 7254 - 7280.

(14) Hossain, M. M.; de Lasa, H. I. Chemical-looping combustion (CLC) for inherent CO_2 separations-a review. *Chem. Eng. Sci.* **2008,** *63*, 4433-4451.

(15) Hurst, S. Production of hydrogen by the steam-iron method. *Oil Soap* **1939,** *16*, 29-35.

(16) Messerschmidt, W. Verfahren zur Erzeugung von Wasserstoff durch abwechselnde Oxidation und Reduktion von Eisen in von außen beheizten, in den Heizräumen angeordneten Zersetzern. 1911.

(17) Gilliland, E. R. Production of industrial gas comprising carbon monoxide and hydrogen. 1954.

(18) Lewis, W. K.; Gilliland, E. R. Production of pure carbon dioixde. 1954.

(19) Richter Horst, J.; Knoche Karl, F., Reversibility of Combustion Processes. In *Efficiency and Costing - Second Law Analysis of Processes*, Gaggioli, R. A., Ed. ACS Symposium Series: Washington DC, 1983; Vol. 235, pp 71-85.

(20) Ishida, M.; Zheng, D.; Akehata, T. Evaluation of a Chemical Looping Combustion Power Generation System by Graphic Exergy Analysis. *Energy* **1987,** *12*, 147-154.

(21) Ishida, M.; Jin, H. CO_2 recovery in a power plant with chemical looping combustion. *Energy Conv. Manag.* **1997,** *38*, S187-S192.

(22) Ishida, M.; Jin, H. G. A New Advanced Power Generation System Using Chemical Looping Combustion. *Energy* **1994,** *19*, 415-422.

(23) Adanez, J.; Gayan, P.; Celaya, J.; de Diego, L. F.; Garcia-Labiano, F.; Abad, A. Chemical looping combustion in a 10 kW_{th} prototype using a CuO/Al_2O_3 oxygen carrier: Effect of operating conditions on methane combustion. *Industrial & Engineering Chemistry Research* **2006,** *45*, 6075-6080.

(24) Linderholm, C.; Mattisson, T.; Lyngfelt, A. Long-term integrity testing of spray-dried particles in a 10-kW chemical-looping combustor using natural gas as fuel. *Fuel* **2009,** - *88*, - 2096.

(25) Lyngfelt, A. Oxygen Carriers for Chemical Looping Combustion - 4000 h of Operational Experience. *Oil & gas science and technology* **2011,** *66*, 161-172.

(26) Pröll, T.; Mayer, K.; Bolhàr-Nordenkampf, J.; Kolbitsch, P.; Mattisson, T.; Lyngfelt, A.; Hofbauer, H. Natural minerals as oxygen carriers for chemical looping combustion in a dual circulating fluidized bed system. *Energy Procedia* **2009,** *1*, 27-34.

(27) Rifflart, S.; Hoteit, A.; Yazdanpanah, M. M.; Pelletant, W.; Surla, K. Construction and operation of a 10 kW CLC unit with circulation configuration enabling independent solid flow control. *Energy Procedia* **2011,** *4*, 333-340.

(28) Shen, L. H.; Wu, J. H.; Xiao, J.; Song, Q. L.; Xiao, R. Chemical-Looping Combustion of Biomass in a 10 kW_{th} Reactor with Iron Oxide As an Oxygen Carrier. *Energy & Fuels* **2009,** *23*, 2498-2505.

(29) Cho, P.; Mattisson, T.; Lyngfelt, A. Comparison of iron-, nickel-, copper- and manganese-based oxygen carriers for chemical-looping combustion. *Fuel* **2004,** *83*, 1215-1225.

(30) Garcia-Labiano, F.; Adanez, J.; de Diego, L. F.; Gayan, P.; Abad, A. Effect of pressure on the behavior of copper-, iron-, and nickel-based oxygen carriers for chemical-looping combustion. *Energy & Fuels* **2006,** *20*, 26-33.

(31) Jerndal, E.; Mattisson, T.; Lyngfelt, A. Thermal analysis of chemical-looping combustion. *Chem. Eng. Res. Des.* **2006,** *84*, 795-806.

(32) Mattisson, T.; Lyngfelt, A.; Cho, P. The use of iron oxide as an oxygen carrier in chemical-looping combustion of methane with inherent separation of CO_2. *Fuel* **2001,** *80*, 1953-1962.

(33) Adanez, J.; de Diego, L. F.; Garcia-Labiano, F.; Gayan, P.; Abad, A.; Palacios, J. M. Selection of oxygen carriers for chemical-looping combustion. *Energy & Fuels* **2004,** *18*, 371-377.

(34) Jin, H. G.; Okamoto, T.; Ishida, M. Development of a novel chemical-looping combustion: Synthesis of a solid looping material of $NiO/NiAl_2O_4$. *Industrial & Engineering Chemistry Research* **1999,** *38*, 126-132.

(35) Mattisson, T.; Johansson, M.; Lyngfelt, A. The use of NiO as an oxygen carrier in chemical-looping combustion. *Fuel* **2006,** *85*, 736-747.

(36) Sedor, K. E.; Hossain, M. M.; de Lasa, H. I. Reactivity and stability of Ni/Al_2O_3 oxygen carrier for chemical-looping combustion (CLC). *Chem. Eng. Sci.* **2008,** *63*, 2994-3007.

(37) Zafar, Q.; Mattisson, T.; Gevert, B. Redox investigation of some oxides of transition-state metals Ni, Cu, Fe, and Mn supported on SiO_2 and $MgAl_2O_4$. *Energy & Fuels* **2006,** *20*, 34-44.

(38) Mattisson, T.; Johansson, M.; Lyngfelt, A. Multicycle reduction and oxidation of different types of iron oxide particles - Application to chemical-looping combustion. *Energy & Fuels* **2004,** *18*, 628-637.

(39) Bhavsar, S.; Veser, G. Bimetallic Fe–Ni Oxygen Carriers for Chemical Looping Combustion. *Industrial & Engineering Chemistry Research* **2013,** *52*, 15342 - 15352.

(40) Kolbitsch, P.; Bolhàr-Nordenkampf, J.; Pröll, T.; Hofbauer, H. Comparison of Two Ni-Based Oxygen Carriers for Chemical Looping Combustion of Natural Gas in 140 kW Continuous Looping Operation. *Ind. Eng. Chem. Res.* **2009,** *48*, 5542 - 5547.

(41) Shulman, A.; Linderholm, C.; Mattisson, T.; Lyngfelt, A. High Reactivity and Mechanical Durability of $NiO/NiAl_2O_4$ and $NiO/NiAl_2O_4/MgAl_2O_4$ Oxygen Carrier Particles Used for more than 1000 h in a 10 kW CLC Reactor. *Industrial & Engineering Chemistry Research* **2009,** *48*, 7400-7405.

(42) Bhavsar, S.; Veser, G. Reducible Supports for Ni-based Oxygen Carriers in Chemical Looping Combustion. *Energy & Fuels* **2013,** *27*, 2073-2084.

(43) Gayán, P.; Forero, C. R.; Abad, A.; de Diego, L. F.; García-Labiano, F.; Adánez, J. Effect of Support on the Behavior of Cu-Based Oxygen Carriers during Long-Term CLC Operation at Temperatures above 1073 K. *Energy & Fuels* **2011,** *25*, 1316-1326.

(44) Forero, C. R.; Gayán, P.; de Diego, L. F.; Abad, A.; García-Labiano, F.; Adánez, J. Syngas combustion in a $500W_{th}$ Chemical-Looping Combustion system using an impregnated Cu-based oxygen carrier. *Fuel Processing Technology* **2009,** *90*, 1471 - 1479.

(45) Mattisson, T.; Jardnas, A.; Lyngfelt, A. Reactivity of some metal oxides supported on alumina with alternating methane and oxygen-application for chemical-looping combustion. *Energy & Fuels* **2003,** *17*, 643-651.

(46) de Diego, L. F.; Gayan, P.; Garcia-Labiano, F.; Celaya, J.; Abad, M.; Adanez, J. Impregnated CuO/Al_2O_3 oxygen carriers for chemical-looping combustion: Avoiding fluidized bed agglomeration. *Energy & Fuels* **2005,** *19*, 1850-1856.

(47) Jin, H.; Okamoto, T.; Ishida, M. Development of a novel chemical-looping combustion: Synthesis of a looping material with a double metal oxide of CoO-NiO. *Energy & Fuels* **1998,** *12*, 1272-1277.

(48) Adanez, J.; Garcia-Labiano, F.; de Diego, L. F.; Gayan, P.; Celaya, J.; Abad, A. Nickel-copper oxygen carriers to reach zero CO and H2 emissions in chemical-looping combustion. *Ind. Eng. Chem. Res.* **2006,** *45*, 2617-2625.

(49) Ekström, C.; Schwendig, F.; Biede, O.; Franco, F.; Haupt, G.; de Koeijer, G.; Papapavlou, C.; Røkke, P. E. Techno-Economic Evaluations and Benchmarking of Pre-combustion CO_2 Capture and Oxy-fuel Processes Developed in the European ENCAP Project. *Energy Procedia* **2009,** *1*, 4233-4240.

(50) Kerr, H. R., Capture and separation technology gaps and priority research needs. In *Carbon dioxide capture for storage in deep geologic formations - results from the CO_2 capture project*, Thomas, D. C.; Benson, S. M., Eds. Elsevier: Oxford, UK, 2005; Vol. 1.

(51) Thambimuthu, K.; Soltanieh, M.; Abanades, J. C., Capture of CO_2. In *IPCC special report on carbon dioxide capture and storage*, Metz, B.; Davidson, O.; de Coninck, H. C.; Loos, M.; Meyer, L. A., Eds. Cambridge University Press: Cambridge, UK, 2005.

(52) Anheden, M.; Svedberg, G. Exergy analysis of chemical-looping combustion systems. *Energy Conv. Manag.* **1998,** *39*, 1967-1980.

(53) Naqvi, R.; Bolland, A. Multi-stage chemical looping combustion (CLC) for combined cycles with CO_2 capture. *Int. J. Greenh. Gas Control* **2007,** *1*, 19-30.

(54) Naqvi, R.; Wolf, J.; Bolland, O. Part-load analysis of a chemical looping combustion (CLC) combined cycle with CO_2 capture. *Energy* **2007,** *32*, 360-370.

(55) Wolf, J.; Anheden, M.; Yan, J. Y. Comparison of nickel- and iron-based oxygen carriers in chemical looping combustion for CO_2 capture in power generation. *Fuel* **2005,** *84*, 993-1006.

(56) Brandvoll, O.; Bolland, O. Inherent CO_2 capture using chemical looping combustion in a natural gas fired power cycle. *J. Eng. Gas. Turbines Power-Trans. ASME* **2004,** *126*, 316-321.

(57) Kvamsdal, H. M.; Jordal, K.; Bolland, O. A quantitative comparison of gas turbine cycles with CO_2 capture. *Energy* **2007,** *32*, 10-24.

(58) Consonni, S.; Lozza, G.; Pelliccia, G.; Rossini, S.; Saviano, F. Chemical-looping combustion for combined cycles with CO_2 capture. *J. Eng. Gas. Turbines Power-Trans. ASME* **2006,** *128*, 525-534.

(59) Bhavsar, S.; Najera, M.; Solunke, R.; Veser, G. Chemical Looping: To Combustion and Beyond. *Catal. Today* **2013**, Accepted.

(60) *US Energy Information Administration (EIA) Annual Energy Outlook*; 2012.

(61) Tsang, S. C.; Claridge, J. B.; Green, M. L. H. Recent advances in the conversion of methane to synthesis gas. *Catal. Today* **1995,** *23*, 3-15.

(62) Hickman, D. A.; Schmidt, L. D. Production of syngas by direct catalytic oxidation of methane. *Science* **1993,** *259*, 343-346.

(63) Ryden, M.; Lyngfelt, A.; Mattisson, T. Synthesis gas generation by chemical-looping reforming in a continuously operating laboratory reactor. *Fuel* **2006,** *85*, 1631-1641.

(64) de Diego, L. F.; Ortiz, M.; Adanez, J.; Garcia-Labiano, F.; Abad, A.; Gayan, P. Synthesis gas generation by chemical-looping reforming in a batch fluidized bed reactor using Ni-based oxygen carriers. *Chemical Engineering Journal* **2008,** *144*, 289-298.

(65) de Diego, L. F.; Ortiz, M.; Garcia-Labiano, F.; Adanez, J.; Abad, A.; Gayan, P. Hydrogen production by chemical-looping reforming in a circulating fluidized bed reactor using Ni-based oxygen carriers. *J. Power Sources* **2009,** *192*, 27-34.

(66) Zafar, Q.; Mattisson, T.; Gevert, B. Integrated hydrogen and power production with CO_2 capture using chemical-looping reforming-redox reactivity of particles of CuO, Mn_2O_3, NiO, and Fe_2O_3 using SiO_2 as a support. *Ind. Eng. Chem. Res.* **2005,** *44*, 3485-3496.

(67) Proll, T.; Bolhar-Nordenkampf, J.; Kolbitsch, P.; Hofbauer, H. Syngas and a separate nitrogen/argon stream via chemical looping reforming - A 140 kW pilot plant study. *Fuel* **2010,** *89*, 1249-1256.

(68) Li, K.; Wang, H.; Wei, Y.; Yan, D. Syngas production from methane and air via a redox process using Ce–Fe mixed oxides as oxygen carriers. *Applied Catalysis B: Environmental* **2010,** *97*, 361-372.

(69) Li, K.; Wang, H.; Wei, Y.; Yan, D. Transformation of methane into synthesis gas using the redox property of Ce–Fe mixed oxides: Effect of calcination temperature. *International Journal of Hydrogen Energy* **2011,** *36*, 3471-3482.

(70) Li, K. Z.; Wang, H.; Wei, Y. G. Syngas Generation from Methane Using a Chemical-Looping Concept: A Review of Oxygen Carriers. *Journal of Chemistry* **2013**.

(71) Zhu, X.; Wang, H.; Wei, Y. G.; Li, K. Z.; Cheng, X. M. Hydrogen and syngas production from two-step steam reforming of methane over CeO_2-Fe_2O_3 oxygen carrier. *Journal of Rare Earths* **2010,** *28*, 907-913.

(72) Galvita, V.; Schröder, T.; Munder, B.; Sundmacher, K. Production of hydrogen with low COx-content for PEM fuel cells by cyclic water gas shift reactor. *International Journal of Hydrogen Energy* **2008,** *33*, 1354-1360.

(73) Gupta, P.; Velazquez-Vargas, L. G.; Fan, L.-S. Syngas redox (SGR) process to produce hydrogen from coal derived syngas. *Energy Fuels* **2007,** *21*, 2900-2908.

(74) Otsuka, K.; Yamada, C.; Kaburagi, T.; Takenaka, S. Hydrogen storage and production by redox of iron oxide for polymer electrolyte fuel cell vehicles. *International Journal of Hydrogen Energy* **2003,** *28*, 335-342.

(75) Solunke, R. D.; Veser, G. Hydrogen Production via Chemical Looping Steam Reforming in a Periodically Operated Fixed-Bed Reactor. *Ind. Eng. Chem. Res.* **2010,** *49*, 11037-11044.

(76) Go, K. S.; Son, S. R.; Kim, S. D.; Kang, K. S.; Park, C. S. Hydrogen production from two-step steam methane reforming in a fluidized bed reactor. *International Journal of Hydrogen Energy* **2009,** *34*, 1301-1309.

(77) Rydén, M.; Arjmand, M. Continuous hydrogen production via the steam–iron reaction by chemical looping in a circulating fluidized-bed reactor. *International Journal of Hydrogen Energy* **2012,** *37*, 4843-4854.

(78) Chiesa, P.; Lozza, G.; Malandrino, A.; Romano, M.; Piccolo, V. Three-reactors chemical looping process for hydrogen production. *International Journal of Hydrogen Energy* **2008,** *33*, 2233-2245.

(79) Centi, G.; Perathoner, S. Opportunities and prospects in the chemical recycling of carbon dioxide to fuels. *Catal. Today* **2009,** *148*, 191-205.

(80) Ma, J.; Sun, N. N.; Zhang, X. L.; Zhao, N.; Mao, F. K.; Wei, W.; Sun, Y. H. A short review of catalysis for CO_2 conversion. *Catal. Today* **2009,** *148*, 221-231.

(81) Song, C. S. Global challenges and strategies for control, conversion and utilization of CO_2 for sustainable development involving energy, catalysis, adsorption and chemical processing. *Catal. Today* **2006,** *115*, 2-32.

(82) Halman, M. M.; Steinberg, M., *Greehhouse Gas Carbon Dioxide Mitigation*. CRC Press LLC: Boca Raton, 1999; p 568.

(83) Teuner, S. Make CO from CO2. *Hydrocarb. Process.* **1985,** *64*, 106-107.

(84) Najera, M.; Solunke, R.; Gardner, T.; Veser, G. Carbon capture and utilization via chemical looping dry reforming. *Chem. Eng. Res. Des.* **2011,** *89*, 1533-1543.

(85) Bhavsar, S.; Najera, M.; Veser, G. Chemical Looping Dry Reforming as Novel, Intensified Process for CO_2 Activation. *Chem. Eng. Technol.* **2012,** *35*, 1281-1290.

(86) Furler, P.; Scheffe, J. R.; Steinfeld, A. Syngas production by simultaneous splitting of H_2O and CO_2 via ceria redox reactions in a high-temperature solar reactor. *Energy Environ. Sci.* **2012,** *5*, 6098-6103.

(87) Chueh, W. C.; Falter, C.; Abbott, M.; Scipio, D.; Furler, P.; Haile, S. M.; Steinfeld, A. High-Flux Solar-Driven Thermochemical Dissociation of CO_2 and H_2O Using Nonstoichiometric Ceria. *Science* **2010,** *330*, 1797-1801.

(88) Corbella, B. M.; Palacios, J. M. Titania-supported iron oxide as oxygen carrier for chemical-looping combustion of methane. *Fuel* **2007,** *86*, 113-122.

(89) Garcia-Labiano, F.; de Diego, L. F.; Adanez, J.; Abad, A.; Gayan, P. Reduction and oxidation kinetics of a copper-based oxygen carrier prepared by impregnation for chemical-looping combustion. *Ind. Eng. Chem. Res.* **2004,** *43*, 8168-8177.

(90) Ishida, M.; Jin, H. G.; Okamoto, T. Kinetic behavior of solid particle in chemical-looping combustion: Suppressing carbon deposition in reduction. *Energy & Fuels* **1998,** *12*, 223-229.

(91) Jin, H. G.; Ishida, M. Reactivity study on natural-gas-fueled chemical-looping combustion by a fixed-bed reactor. *Ind. Eng. Chem. Res.* **2002,** *41*, 4004-4007.

(92) Mattisson, T.; Garcia-Labiano, F.; Kronberger, B.; Lyngfelt, A.; Adanez, J.; Hofbauer, H. Chemical-looping combustion using syngas as fuel. *Int. J. Greenh. Gas. Con.* **2007,** *1*, 158-169.

(93) Trovarelli, A. Catalytic properties of ceria and CeO_2-containing materials. *Catal. Rev.-Sci. Eng.* **1996,** *38*, 439-520.

(94) Kaspar, J.; Fornasiero, P.; Hickey, N. Automotive catalytic converters: current status and some perspectives. *Catal. Today* **2003,** *77*, 419-449.

(95) Fu, Q.; Saltsburg, H.; Flytzani-Stephanopoulos, M. Active nonmetallic Au and Pt species on ceria-based water-gas shift catalysts. *Science* **2003,** *301*, 935-938.

(96) Liang, S.; Veser, G. Mixed Lanthana/Ceria Nanorod-Supported Gold Catalysts for Water–Gas-Shift. *Catal. Lett.* **2012,** *142*, 936-945.

(97) Dong, W. S.; Jun, K. W.; Roh, H. S.; Liu, Z. W.; Park, S. E. Comparative study on partial oxidation of methane over Ni/ZrO_2, Ni/CeO_2 and $Ni/Ce-ZrO_2$ catalysts. Catalysis Letters 2002, *78*, 215-222.

(98) Pengpanich, S.; Meeyoo, V.; Rirksomboon, T.; Bunyakiat, K. Catalytic oxidation of methane over CeO_2-ZrO_2 mixed oxide solid solution catalysts prepared via urea hydrolysis. *Appl. Catal. A-Gen.* **2002,** *234*, 221-233.

(99) Zhu, T. L.; Flytzani-Stephanopoulos, M. Catalytic partial oxidation of methane to synthesis gas over Ni-CeO_2. *Appl. Catal. A-Gen.* **2001,** *208*, 403-417.

(100) Wang, J. S. B.; Tai, Y. L.; Dow, W. P.; Huang, T. J. Study of ceria-supported nickel catalyst and effect of yttria doping on carbon dioxide reforming of methane. *Appl. Catal. A-Gen.* **2001,** *218*, 69-79.

(101) Shan, W. J.; Luo, M. F.; Ying, P. L.; Shen, W. J.; Li, C. Reduction property and catalytic activity of $Ce_{1-x}Ni_xO_2$ mixed oxide catalysts for CH4 oxidation. *Appl. Cat. A-Gen.* **2003,** *246*, 1-9.

(102) Moghtaderi, B. Review of the Recent Chemical Looping Process Developments for Novel Energy and Fuel Applications. *Energy & Fuels* **2012,** *26*, 15-40.

(103) Li, K. Z.; Wang, H.; Wei, Y. G.; Yan, D. X. Syngas production from methane and air via a redox process using Ce-Fe mixed oxides as oxygen carriers. *Appl. Catal. B-Environ.* **2010,** *97*, 361-372.

(104) He, F.; Wei, Y. G.; Li, H. B.; Wang, H. Synthesis Gas Generation by Chemical-Looping Reforming Using Ce-Based Oxygen Carriers Modified with Fe, Cu, and Mn Oxides. *Energy & Fuels* **2009,** *23*, 2095-2102.

(105) Kang, K. S.; Kim, C. H.; Bae, K. K.; Cho, W. C.; Kim, W. J.; Kim, Y. H.; Kim, S. H.; Park, C. S. Redox cycling of $CuFe_2O_4$ supported on ZrO_2 and CeO_2 for two-step methane reforming/water splitting. *Int. J. Hydrog. Energy* **2010,** *35*, 568-576.

(106) Liang, S. A.; Broitman, E.; Wang, Y. N.; Cao, A. M.; Veser, G. Highly stable, mesoporous mixed lanthanum-cerium oxides with tailored structure and reducibility. *J. Mater. Sci.* **2011,** *46*, 2928-2937.

(107) Fleming, P.; Farrell, R.; Holmes, J.; Morris, M. The Rapid Formation of $La(OH)_3$ from La_2O_3 Powders on Exposure to Water Vapor. *J. Am. Ceram. Soc.* **2010,** *93*, 1187-1194.

(108) Liu, T.; Snyder, C.; Veser, G. Catalytic partial oxidation of methane: Is a distinction between direct and indirect pathways meaningful? *Ind. Eng. Chem. Res.* **2007,** *46*, 9045-9052.

(109) Fornasiero, P.; Balducci, G.; Di Monte, R.; Kaspar, J.; Sergo, V.; Gubitosa, G.; Ferrero, A.; Graziani, M. Modification of the Redox Behaviour of CeO_2 Induced by Structural Doping with ZrO_2. *Journal of Catalysis* **1996,** *164*, 173-183.

(110) Mamontov, E.; Egami, T.; Brezny, R.; Koranne, M.; Tyagi, S. Lattice defects and oxygen storage capacity of nanocrystalline ceria and ceria-zirconia. *J. Phys. Chem. B* **2000,** *104*, 11110-11116.

(111) Wang, X. Q.; Shen, M. Q.; Wang, J.; Fabris, S. Enhanced Oxygen Buffering by Substitutional and Interstitial Ni Point Defects in Ceria: A First-Principles DFT plus U Study. *J. Phys. Chem. C* **2010,** *114*, 10221-10228.

(112) Vayssilov, G. N.; Lykhach, Y.; Migani, A.; Staudt, T.; Petrova, G. P.; Tsud, N.; Skala, T.; Bruix, A.; Illas, F.; Prince, K. C.; Matolin, V.; Neyman, K. M.; Libuda, J. Support nanostructure boosts oxygen transfer to catalytically active platinum nanoparticles. *Nature Materials* **2011,** *10*, 310-315.

(113) Perrichon, V.; Laachir, A.; Abouarnadasse, S.; Touret, O.; Blanchard, G. Thermal stability of a high surface area ceria under reducting atmosphere. *Appl. Catal. A-Gen.* **1995,** *129*, 69-82.

(114) Balducci, G.; Kaspar, J.; Fornasiero, P.; Graziani, M.; Islam, M. S. Surface and reduction energetics of the CeO_2-ZrO_2 catalysts. *J. Phys. Chem. B* **1998,** *102*, 557-561.

(115) Hossain, M. M.; de Lasa, H. I. Reactivity and stability of Co-Ni/Al_2O_3 oxygen carrier in multicycle CLC. *Aiche J.* **2007,** *53*, 1817-1829.

(116) Hossain, M. M.; Sedor, K. E.; de Lasa, H. I. Co-Ni/Al_2O_3 oxygen carrier for fluidized bed chemical-looping combustion: Desorption kinetics and metal-support interaction. *Chem. Eng. Sci.* **2007,** *62*, 5464-5472.

(117) Johansson, M.; Mattisson, T.; Lyngfelt, A. Creating a synergy effect by using mixed oxides of iron- and nickel oxides in the combustion of methane in a chemical-looping combustion reactor. *Energy & Fuels* **2006,** *20*, 2399-2407.

(118) Son, S. R.; Kim, S. D. Chemical-looping combustion with NiO and Fe_2O_3 in a thermobalance and circulating fluidized bed reactor with double loops. *Industrial & Engineering Chemistry Research* **2006,** *45*, 2689-2696.

(119) Bara, J. J.; Pedziwiatr, A. T.; Stadnik, Z. M.; Szytula, A.; Todorovic, J.; Tomkowicz, Z.; Zarek, W. Investigations of crystal and magnetic-properties of nickel ferrites-aluminates. *Phys. Status Solidi A-Appl. Res.* **1977,** *44*, 325-331.

(120) Sileo, E. E.; Rotelo, R.; Jacobo, S. E. Nickel zinc ferrites prepared by the citrate precursor method. *Physica B* **2002,** *320*, 257-260.

(121) Lee, J. B.; Park, C. S.; Choi, S.; Song, Y. W.; Kim, Y. H.; Yang, H. S. Redox characteristics of various kinds of oxygen carriers for hydrogen fueled chemical-looping combustion. *J. Ind. Eng. Chem.* **2005,** *11*, 96-102.

(122) Gemmi, M.; Merlini, M.; Cornaro, U.; Ghisletti, D.; Artioli, G. In situ simultaneous synchrotron powder diffraction and mass spectrometry study of methane anaerobic combustion on iron-oxide-based oxygen carrier. *J. Appl. Crystallogr.* **2005,** *38*, 353-360.

(123) Dewaele, O.; Froment, G. F. TAP study of the mechanism and kinetics of the adsorption and combustion of methane on Ni/Al_2O_3 and NiO/Al_2O_3. *Journal of Catalysis* **1999,** *184*, 499-513.

(124) Veser, G.; Frauhammer, J. Modelling steady state and ignition during catalytic methane oxidation in a monolith reactor. *Chemical Engineering Science* **2000,** *55*, 2271-2286.

(125) Shih, K.; White, T.; Leckie, J. O. Nickel stabilization efficiency of aluminate and ferrite spinels and their leaching behavior. *Environ. Sci. Technol.* **2006,** *40*, 5520-5526.

(126) Lambert, A.; Delquié, C.; Clémeneçon, I.; Comte, E.; Lefebvre, V.; Rousseau, J.; Durand, B. Synthesis and characterization of bimetallic Fe/Mn oxides for chemical looping combustion. *Energy Procedia* **2009,** *1*, 375-381.

(127) Muan, A.; Somiya, S. The system of iron oxide-manganese oxide in air. *American journal of science (1880)* **1962,** *260*, 230-240.

(128) Azimi, G.; Leion, H.; Rydén, M.; Mattisson, T.; Lyngfelt, A. Investigation of Different Mn–Fe Oxides as Oxygen Carrier for Chemical-Looping with Oxygen Uncoupling (CLOU). *Energy & Fuels* **2012,** *27*, 367-377.

(129) Azimi, G.; Rydén, M.; Leion, H.; Mattisson, T.; Lyngfelt, A. $(Mn_zFe_{1-z})_yO_x$ combined oxides as oxygen carrier for chemical-looping with oxygen uncoupling. *Aiche J.* **2013,** *59*, 582-588.

(130) Shulman, A.; Cleverstam, E.; Mattisson, T.; Lyngfelt, A. Manganese/Iron, Manganese/Nickel, and Manganese/Silicon Oxides Used in Chemical-Looping With Oxygen Uncoupling (CLOU) for Combustion of Methane. *Energy & Fuels* **2009,** *23*, 5269-5275.

(131) de Medeiros, S. N.; Luciano, A.; Cótica, L. F.; Santos, I. A.; Paesano Jr, A.; da Cunha, J. B. M. Structural and magnetic characterization of the ball-milled α-Fe_2O_3–Mn_2O_3 and α-Fe–Mn_2O_3 systems. *Journal of Magnetism and Magnetic Materials* **2004,** *281*, 227-233.

(132) Landolt, H.; Börnstein, R., *Landoldt-Börnstein Numerical Data and Functional Relationships in Science and Technology New Series, Group III, vol , Part b1, edited by K.-H. Hellwege and A. M. Hellwege*. Springer-Verlag: New York, 1975.

(133) Geller, S. Structure of α-Mn_2O_3, $(Mn_{0.983}Fe_{0.017})_2O_3$ and $(Mn_{0.37}Fe_{0.63})_2O_3$ and relation to magnetic ordering. *Acta Crystallographica Section B* **1971,** *27*, 821-828.

(134) Seifu, D.; Kebede, A.; Oliver, F. W.; Hoffman, E.; Hammond, E.; Wynter, C.; Aning, A.; Takacs, L.; Siu, I. L.; Walker, J. C.; Tessema, G.; Seehra, M. S. Evidence of ferrimagnetic ordering in $FeMnO_3$ produced by mechanical alloying. *Journal of Magnetism and Magnetic Materials* **2000,** *212*, 178-182.

(135) Christian Enger, B.; Lødeng, R.; Holmen, A. A review of catalytic partial oxidation of methane to synthesis gas with emphasis on reaction mechanisms over transition metal catalysts. *Applied Catalysis A: General* **2008,** *346*, 1-27.

(136) Noorman, S.; Annaland, M. V.; Kuipers, H. Packed bed reactor technology for chemical-looping combustion. *Industrial & Engineering Chemistry Research* **2007,** *46*, 4212-4220.

(137) Neumann, D.; Veser, G. Catalytic partial oxidation of methane in a high-temperature reverse-flow reactor. *Aiche J.* **2005,** *51*, 210-223.

(138) Veser, G. Multiscale process intensification for catalytic partial oxidation of methane From nanostructured catalysts to integrated reactor concepts. *Catal. Today* **2010,** *157*, 24-32.

(139) Eigenberger, G.; Nieken, U. Catalytic combustion with periodic flow reversal. *Chemical Engineering Science* **1988,** *43*, 2109-2115.

(140) Neumann, D.; Gepert, V.; Veser, G. Some Considerations on the Design and Operation of High-Temperature Catalytic Reverse-Flow Reactors. *Industrial & Engineering Chemistry Research* **2004,** *43*, 4657-4667.

(141) Go, K. S.; Son, S. R.; Kim, S. D. Reaction kinetics of reduction and oxidation of metal oxides for hydrogen production. *Int. J. Hydrog. Energy* **2008,** *33*, 5986-5995.

(142) Loutzenhiser, P. G.; Galvez, M. E.; Hischier, I.; Stamatiou, A.; Frei, A.; Steinfeld, A. CO_2 Splitting via Two-Step Solar Thermochemical Cycles with Zn/ZnO and FeO/Fe_3O_4 Redox Reactions II: Kinetic Analysis. *Energy Fuels* **2009,** *23*, 2832-2839.

(143) Bhavsar, S.; Najera, M.; Solunke, R.; Veser, G. Chemical looping: To combustion and beyond. *Catal. Today*, in press.

(144) Cao, A.; Lu, R.; Veser, G. Stabilizing metal nanoparticles for heterogeneous catalysis. *Phys. Chem. Chem. Phys.* **2010,** *12*, 13499-13510.

(145) Kirchhoff, M.; Specht, U.; Veser, G. Engineering high-temperature stable nanocomposite materials. *Nanotechnology* **2005,** *16*, S401-S408.

(146) Sanders, T.; Papas, P.; Veser, G. Supported nanocomposite catalysts for high-temperature partial oxidation of methane. *Chem. Eng. J.* **2008,** *142*, 122-132.

(147) Arai, H.; Machida, M. Thermal stabilization of catalyst supports and their application to high-temperature catalytic combustion. *Appl. Catal., A* **1996,** *138*, 161-176.

(148) Machida, M.; Eguchi, K.; Arai, H. Effect of additives on the surface area of oxide supports for catalytic combustion. *J. Catal.* **1987,** *103*, 385-393.

(149) Joo, S. H.; Park, J. Y.; Tsung, C. K.; Yamada, Y.; Yang, P. D.; Somorjai, G. A. Thermally stable Pt/mesoporous silica core-shell nanocatalysts for high-temperature reactions. *Nat. Mater.* **2009,** *8*, 126-131.

(150) Takenaka, S.; Umebayashi, H.; Tanabe, E.; Matsune, H.; Kishida, M. Specific performance of silica-coated Ni catalysts for the partial oxidation of methane to synthesis gas. *J. Catal.* **2007,** *245*, 392-400.

(151) Fotou, G. P.; Lin, Y. S.; Pratsinis, S. E. Hydrothermal stability of pure and modified microporous silica membranes. *J. Mater. Sci.* **1995,** *30*, 2803-2808.

(152) Ramkumar, S.; Fan, L. S. Calcium Looping Process (CLP) for Enhanced Noncatalytic Hydrogen Production with integrated Carbon Dioxide Capture. *Energy Fuels* **2010,** *24*, 4408-4418.

(153) Solunke, R. D.; Veser, G. Nanocomposite Oxygen Carriers for Chemical-Looping Combustion of Sulfur-Contaminated Synthesis Gas. *Energy Fuels* **2009,** *23*, 4787-4796.

(154) Solunke, R. D.; Veser, G. Integrating desulfurization with CO_2-capture in chemical-looping combustion. *Fuel* **2011,** *90*, 608-617.

(155) Perkins, C.; Weimer, A. W. Likely near-term solar-thermal water splitting technologies. *Int. J. Hydrog. Energy* **2004,** *29*, 1587-1599.

(156) Steinfeld, A. Solar hydrogen production via a two-step water-splitting thermochemical cycle based on Zn/ZnO redox reactions. *Int. J. Hydrog. Energy* **2002,** *27*, 611-619.

(157) Howarth, R. W. Should Fracking Stop? *Nat. Mater.* **2011,** *477*, 271-275.

(158) Steinfeld, A. Solar thermochemical production of hydrogen—a review. *Solar Energy* **2005,** *78*, 603-615.

(159) Greeley, J.; Nørskov, J. K.; Mavrikakis, M. Electronic strucure and catalysis on metal surfaces. *Annual Review of Physical Chemistry* **2002,** *53*, 319-348.

(160) Mowbray, D. J.; Martínez, J. I.; Calle-Vallejo, F.; Rossmeisl, J.; Thygesen, K. S.; Jacobsen, K. W.; Nørskov, J. K. Trends in Metal Oxide Stability for Nanorods, Nanotubes, and Surfaces. *The Journal of Physical Chemistry C* **2010,** *115*, 2244-2252.

(161) Nørskov, J. K.; Bligaard, T.; Rossmeisl, J.; Christensen, C. H. Towards the computational design of solid catalysts. *Nature Chemistry* **2009,** *1*, 37-46.

(162) Ruban, A.; Hammer, B.; Stoltze, P.; Skriver, H. L.; Nørskov, J. K. Surface electronic structure and reactivity of transition and noble metals. *Journal of Molecular Catalysis A: Chemical* **1997,** *115*, 421-429.

(163) Schaub, R.; Thostrup, P.; Lopez, N.; Lægsgaard, E.; Stensgaard, I.; Nørskov, J. K.; Besenbacher, F. Oxygen Vacancies as Active Sites for Water Dissociation on Rutile TiO_2 (110). *Physical Review Letters* **2001,** *87*, 266104.

(164) Liang, S.; Veser, G. Mixed Lanthana/Ceria Nanorod-Supported Gold Catalysts for Water–Gas-Shift. *Catal. Lett.* **2012,** *142*, 936-945.